MICROSTRUCTURE AND GROWTH OF Al_2O_3 ON Ni-Al ALLOYS

By

HAROUN MOHAMED HINDAM, B.Sc.

A Thesis

Submitted to the School of Graduate Studies

in Partial Fulfilment of the Requirements

for the Degree

Doctor of Philosophy

McMaster University

May 1979

MICROSTRUCTURE AND GROWTH OF Al_2O_3 ON Ni-Al ALLOYS

DOCTOR OF PHILOSOPHY (1979)
(Metallurgy and Materials Science)

McMASTER UNIVERSITY
Hamilton, Ontario

TITLE : Microstructure and Growth of Al_2O_3 on Ni-Al Alloys

AUTHOR : Haroun Mohamed Hindam, B.Sc. (Cairo University)

SUPERVISOR : Dr. W.W. Smeltzer

NUMBER OF PAGES : xii, 168

ABSTRACT

The oxidation properties of Ni-2, Ni-6 and Ni-32wt.%Al alloys were investigated in one atm oxygen at the temperature range 1273 to 1573 K. The reaction kinetics were determined thermogravimetrically and by layer thickness measurements. The reacted specimens were analyzed using light microscopy, X-ray diffraction, X-ray topography and electron metallographic techniques (TEM, SEM, EPMA and AES). Particular interest was given to the growth of Al_2O_3 on these alloys.

Ni-2wt.%Al alloy oxidizes parabolically, at a rate one order of magnitude larger than pure Ni, giving rise to a scale consisting of an outer Al-doped NiO layer, an inner $NiO-NiAl_2O_4$ layer and an Al_2O_3-alloy internal precipitation zone. The growth of the Al_2O_3 rodlike precipitates, which is interpreted by a $NiO/Al_{(alloy)}$ solid state displacement reaction, is controlled by oxygen diffusion through the Al-depleted alloy in the precipitation zone. The increase in the reaction rate is attributed to the doping effect of dissolved Al on NiO and the high affinity of Al for oxygen resulting in internal precipitation.

The oxidation kinetics of Ni-6wt.%Al alloy are irreproducible due to the formation of an imperfect Al_2O_3 scale containing NiO nodules, localized at alloy grain boundaries, beneath which Al_2O_3 is precipitated internally. The transition from internal precipitation to continuous Al_2O_3 formation is

interpreted by a model involving the impingement of favorably oriented rodlike precipitates and lateral diffusion of Al from the impingement sites to neighboring regions of the precipitation front. The steady oxidation stage is controlled by thickening of the Al_2O_3 film.

The initial sub-microcrystalline film, which is formed on Ni-32wt.%Al alloy, "recrytallizes" subsequently to α-Al_2O_3 giving rise to a well oriented film containing regions of disarrayed polycrystalline oxide. Inert marker measurements indicated that the initial film grows by inward oxygen diffusion. The metallographic observations on the growth of the recrystallized α-Al_2O_3 scale are consistent with counter-current Al and oxygen boundary diffusion in the disarrayed oxide and outward Al lattice diffusion in the oriented film. Accordingly, the growth of this scale was interpreted by a short-circuit diffusion model involving simultaneous reactants lattice and boundary diffusion.

ACKNOWLEDGEMENTS

The author wishes to express his sincere appreciation to Dr. W. Smeltzer for his guidance and encouragement throughout the stages of this program. The interest shown by Dr. J. Kirkaldy and Dr. P. Dawson, who both served on the supervisory committee, is gratefully acknowledged.

He is indebted to Dr. T. Homma for his general interest in this work, in particular for suggesting and carrying out the X-ray topography measurements. Valuable discussion and helpful advice, concerning Auger electron spectroscopy measurements, offered by Dr. J. Robinson, are gratefully appreciated.

Thanks are also due to the staff and graduate students of the McMaster Metallurgy Department for their help and friendship. In particular, I wish to thank Mr. T. Bryner for preparing the alloys, Messrs. D. Hodgson and F. Gibbs for technical assistance, drafting and photographic work, Messrs. F. Smith and F. Pearson for assistance with the electron metallographic techniques.

The author gratefully acknowledges the financial support of the Department of Metallurgy and Materials Science in the form of scholarship and teaching assistantship.

TABLE OF CONTENTS

LIST OF FIGURES

LIST OF TABLES

CHAPTER 1

INTRODUCTION

Nickel superalloys find wide applications as construction materials for gas turbine engines either for aircraft or industrial applications, coal combustion furnaces and high temperature reactors for electric power generation. In this environment, the alloys are subjected to severe corrosive conditions resulting from hot oxidizing gas. Alloys operating in such environment must fulfill two major requirements : high mechanical and corrosion resistances.

Mechanical resistance is achieved by precipitation hardening with $\{Ni_3(Al,Ti)\}$ phase, called gamma prime, which precipitates coherently in the matrix[1]. Refractory metals are added to act as solid solution strengtheners[1]. The presence of carbides of Ti, Cr and refractory metals inhibits grain boundary sliding and improves creep resistance[1]. Dispersion hardening with oxide particles or fibres also contributes to the strength of the alloys[2,3].

Oxidation resistance is achieved by incorporating metallic elements which can be selectively oxidized to form a continuous, adherent and slow-growing oxide film. Cr, which forms a protective Cr_2O_3 scale, is the most frequently used metal for this purpose. However, at high temperatures and in oxygen atmospheres, the formation of volatile oxides of Cr[4] deteriorates

the oxidation resistance of the alloys. This phenomenon is enhanced during service due to thermal fluctuations and high flow rates of oxidizing gases. Al is a potential competitor to Cr in this respect, since volatilization of Al_2O_3 in oxidizing atmosphere is minimal[5] and diffusion in this oxide is much slower than in Cr_2O_3 under the same experimental conditions[6,7].

Considerable effort has been made to achieve each of these two properties independently. As a result, it is necessary to apply a coating on high strength alloys to form a composite system which combines corrosion resistance with mechanical strength. Nickel aluminide coatings based on the intermetallic phases Ni_3Al (γ') and NiAl (β) have been successfully used in this field[8-15]. In oxidizing environments, a protective Al_2O_3 film is formed.

The objective of this research is to study the mechanism of growth of Al_2O_3 on Ni-Al alloys at high temperatures in oxygen atmospheres. Depending on the experimental conditions, Al_2O_3 may form as internal precipitates or as a continuous protective film[16]. Particular interest is given to the latter case since the growth of a protective Al_2O_3 on alloys containing Al has been the subject of several controversial interpretations[16-29]. A major problem encountered in the task of elucidating oxide film growth is the identification of the mobile species responsible for its thickening. In the present study, a new method, which is based on inert markers and a surface sensitive electron spectroscopy technique (AES),

has been developed to yield this necessary data. The mechanisms of growth of the rodlike Al_2O_3 precipitates beneath a NiO film and the transition from internal oxidation to the development of a multi-layered $NiO/NiAl_2O_4/Al_2O_3$ scale have been defined. It was also demonstrated that the growth of the protective Al_2O_3 scale can be adequately interpreted with a model which is based on simultaneous diffusion of the reactants along lattice sites and grain boundaries in the scale.

Several techniques have been used to obtain and collate the necessary data : alloy preparation and homogenization, chemical analysis, sample metallographic preparation, inert marker technique, thermogravimetric analysis, optical microscopy, X-ray diffraction and topography, electron metallography (TEM, RHEED, SEM, EPMA and AES) and ion sputtering techniques.

In the next chapter, a brief description of the oxidation theory of metals is presented in order to emphasize the fundamental concepts necessary for this study. This is followed by a literature review of the relevant systems (Chapter 3). The experimental techniques and procedures are described in Chapter 4. The results are presented in Chapter 5 under three sub-headings : internal oxidation, transition from internal oxidation to continuous scale formation and growth of protective Al_2O_3 scale. Finally, scale growth models are proposed to rationalize the experimental observations (Chapter 6).

CHAPTER 2

PRINCIPLES OF METAL OXIDATION

2.1 INTRODUCTION

The different aspects of oxidation have been documented in several monographs [7,30-37] and have been the subject of recent reviews [38,39].

When a bare metal is exposed to oxygen, the reaction is initiated by the chemisorption of oxygen molecules impinging on the surface. Oxygen dissociation by place exchange with the underlying metal leads to the formation of oxide nuclei at random sites on the substrate. Subsequent lateral growth results in complete coverage of the surface with a micro-crystalline oxide film. Amorphous oxide films have also been observed at low temperatures.

In order that the oxide film continue to thicken, the reactants (metal and oxygen ions) must diffuse in the oxide. In crystalline substances, diffusion occurs via migration of point defects, whereas amorphous substances contain open extended channels in their network through which cations and/or anions can move.

At low temperatures and in the thin film range (thickness < 10^3 nm), the chemical potential gradient is insufficient to drive the reaction. However, a large electrostatic field, set up across the film due to the ionization of oxygen and the

metal at the oxide/gas and metal/oxide interfaces, respectively, acts as the driving force. In this regime, the kinetics follow one of several rate equations, namely :

- Logarithmic : $(\Delta W/A) = k_l \log (at + t_o)$ (2.1)

- Inverse Logaritmic : $(\Delta W/A)^{-1} = b - k_{il} \log t$ (2.2)

- Cubic : $(\Delta W/A)^3 = k_c\, t$ (2.3)

- Parabolic : $(\Delta W/A)^2 = k_p\, t + c$ (2.4)

where $\Delta W/A$ is the weight gain per unit area,

k is the reaction rate constant,

t is time,

a, b, c are constants.

Several models[40,41] have been proposed to explain the observed kinetics based on reactions involving transport across the film (cations, anions or electrons) or surface reactions as controlling steps. However, there is no clear distinction between one model and the other and different postulated mechanisms often lead to the same kinetic equation.

The growth of thick scales on metals usually follows a parabolic law. Wagner[42] postulated that scaling occurs by " ambipolar diffusion " of non-interacting point defects and electrons under the influence of their electrochemical potential gradients.

Linear kinetics are observed when the scale cracks allowing direct access of oxygen to the substrate. Surface reac-

tion controlling steps (e.g. dissociation of gaseous reactants, volatilization of oxidation products, etc.) also give rise to linear kinetics and are strongly dependent on the gas pressure.

At intermediate temperatures ($T < 0.75$ to $0.8\ T_m$), the rate of oxidation of most metals is too high to be explained by lattice diffusion solely. Since the activation energy for grain boundary diffusion is much less than for lattice diffusion, it is imperative to consider the effect of structural imperfections on oxidation. Models, which are based on simultaneous diffusion in oxide lattice and easy diffusion paths, have been advanced by Smeltzer et al.[43-51] to account for the observed oxidation kinetics of several metals. The low resistance paths are structural imperfections present in the oxide scale (e.g. grain boundaries, dislocations,etc.).

2.2 DEFECT STRUCTURES OF OXIDES

In oxides, bulk diffusion occurs via the migration of point defects and electrons. Accordingly, they are classified by their defect structures into :[7,34]

- Metal-deficient oxides: (p-type) having positive holes and cation vacancies (e.g. FeO, NiO, CoO, Cu_2O,etc.) or oxygen interstitials.
- Metal-excess oxides : (n-type) having electrons and cation interstitials (e.g. CdO, ZnO, etc.) or oxygen vacancies (e.g. ZrO_2, Nb_2O_5, HfO_2, etc.).

The effect of oxygen pressure on the defect equilibria in oxides can be best visualized with the aid of Kröger-Vink

diagrams[7,34]. A hypothetical diagram may be derived by writing the possible defect reactions and applying the law of mass action to each reaction coupled with the electroneutrality condition assuming that the activity coefficients are unity and that each species occurs in a single ionization state.

The electrical conductivity of an oxide, K, is related to the concentrations of the electrical charge carriers, their mobilities and charges. In limiting cases, it may be expressed as :

$$K = a\, p_{O_2}^{1/n} \qquad (2.5)$$

where the sign and magnitude of the exponential term depend on the nature and the ionization state of the defects, respectively. The deviation from a simple power relationship may be due to the existence of defects in different ionization states, their association and interaction to form vacancy clusters or shear structures[38,39].

2.3 WAGNER PARABOLIC OXIDATION THEORY[42]

Consider a reaction system composed of the reactants (metal and oxygen) separated by a layer of the reaction product (oxide)• Assuming diffusion control, the interfaces may be considered at local equilibrium, i.e. the concentrations of the reactants are time independent.For a two-component system and at fixed temperature and pressure, Gibbs phase rule assigns zero degree of freedom for a two-phase system which is presented here by the interface. Consequently, the concentrations correspond to those obtained from the phase diagram of

the relevant system at the appropriate temperature.

Based on the local equilibrium concept and assuming that scaling occurs by ambipolar diffusion of non-interacting point defects and electrons under the influence of their respective electrochemical potential gradients, the rational parabolic constant for scale growth can be ascertained as :

$$k \text{ (g eq/cm sec)} = \bar{C}_{eq} \int_{a_O^i}^{a_O^0} \left(\frac{|Z_M|}{|Z_O|} D_M + D_O\right) d\ln a_O \qquad (2.6)$$

where $\bar{C}_{eq}$ is the average concentration in g eq/cm^3,

D_M and D_O are the self diffusion coefficients of the metal and oxygen, respectively,

Z_M and Z_O are their valences,

a_O^0 and a_O^i are the oxygen activities at the oxide/gas and metal/oxide interfaces, respectively.

The model fits the observations for most oxides having a narrow homogeneity range at high temperatures. At temperatures below about 0.75 to 0.8 T_m, the role of structural imperfections in the oxide must be considered since the activation energy for diffusion along these defects is much smaller than for lattice diffusion. In oxides having a large concentration of point defects, (e.g. FeO), association and interaction of vacancies occur, as discussed earlier. Whence, a one to one correspondence is not expected between the concentration of vacancies and diffusion; transport being occuring by a cooperative role between neighboring vacancies rather than by individual jumps[39].

2.4 SHORT-CIRCUIT DIFFUSION IN OXIDE SCALES

Although direct experimental evidence for enhanced diffusion along grain boundaries in metals was obtained several years ago[52], it is only recently that the role of such imperfections on diffusion in oxides has been recognized. The following observations emphasize the role of structural imperfections in diffusion and scale growth :

- Examination of NiO films, using TEM, has revealed that they are composed of small crystallites having a high density of boundaries which are relatively easier diffusion paths than the lattice[43-45].

- Ni single crystals oxidize anisotropically; oxidation being dependent on crystal orientation[46-49,53,54]. The anisotropy was found to be related to the density of structural imperfections present in the oxide film formed on each face. The latter is determined by nucleation and growth processes which are orientation dependent.

- ZrO_2 scales are composed of coarse columnar grains extending from the metal/scale to the scale/gas interfaces. The presence of these preferred sites for oxygen diffusion explains the high oxidation rates of Zr and several other refractory metals[38].

- A porous scale is formed when certain refractory metals (e.g. Mo and W) are oxidized. The porosity, which is due to transformation to sub-oxides, accelerates oxygen diffusion in the scale[38].

- Diffusion coefficients for polycrystalline oxides are several orders of magnitude greater than for single crystals and are

sensitive to grain size[55,56].

- Oxide whiskers have been observed during the oxidation of metals[57-61]. It has been confirmed that these filaments contain linear defects which may be responsible for their relatively fast growth[59-61].

- Scale aging, by annealing the pre-oxidized metal in vacuum, decreases its " permeability " and alters its texture. These changes are reflected by a pronounced decrease in the oxidation rate upon subsequent exposure to the oxidizing atmosphere[62].

Following the argument advanced by Hart[63] for random diffusion of atoms in the lattice and grain boundaries, Smeltzer et al.[43-51] have evoked short-circuit diffusion models to account for the observed oxidation kinetics of several metals. They are discussed briefly in the following. According to Hart, the effective diffusion coefficient for the movement of atoms in a solid matrix containing a random array of line defects may be expressed as :

$$D_{eff} = (1-f)\ D_L + f\ D_B \qquad (2.7)$$

where D_L and D_B are the lattice and boundary diffusion coefficients, respectively,

f is the fraction of easy diffusion sites.

Assuming a linear concentration gradient across the scale, the flux may be expressed using Fick's first law :

$$J = - D_{eff} \frac{\Delta c}{x} \qquad (2.8)$$

The rate of oxide thickening is given by :

$$\frac{dx}{dt} = D_{eff} \frac{\Delta c}{x} \tilde{V} \qquad (2.9)$$

where $\tilde{V}$ is the oxide specific volume.

Several cases have been investigated :

(I) The density of easy diffusion paths remains unaltered during oxidation :

Integration of Eq.(2.9) defines an effective parabolic rate constant

$$k_{eff} = 2 D_{eff} \hat{V} \Delta c \qquad (2.10)$$

which is greater than that predicted by Wagner theory. The oxidation of Zr was found to conform to this behavior[50].

(II) The density of easy diffusion paths decays with time :

(a) The decay is essentially due to grain growth as revealed by TEM in the case of NiO[43-49]. A general expression for grain growth is :

$$D_t^2 - D_o^2 = k' t \qquad (2.11)$$

where D_o and D_t are the mean initial diameter and after time t, respectively. For an array of square blocks, the fraction of easy diffusion sites per unit area is given by :

$$f(t) = \frac{2d}{D_t} \qquad (2.12)$$

where d is the boundary width. Substituting D_t from Eq.(2.11) in the last expression, the fraction of easy diffusion paths becomes

$$f = \frac{2d}{(D_o^2 + k' t)^{1/2}} \qquad (2.13)$$

(b) The decay is associated with the ordering of disarrayed oxide at grain boundaries driven by growth stresses. This mechanism has been postulated for Ti, Hf and Zr at intermediate temperatures[51]. A first order expression was used to describe the decay :

$$-\frac{df}{dt} = k' f \quad \text{or} \quad f = f^o e^{-k't} \qquad (2.14)$$

After evaluating the effective diffusion coefficient by substituting Eq.(2.13) or (2.14) in Eq.(2.7),integration of Eq.(2.9) yields expressions which describe the growth of oxide films when both lattice and grain boundary diffusion determine the reaction rate.

2.5 BINARY ALLOY OXIDATION

2.5.1 The Diffusion Path Concept

Referring to Onsager's phenomological multicomponent diffusion theory, as applied by Kirkaldy to oxides and sulfides (Ref.(35), p.101), the following expressions, which are similar to Fick's second law, can be derived to relate the concentrations of the two independent components in a ternary system

$$\frac{\partial C_1}{\partial t} = \frac{\partial}{\partial x} D_{11} \frac{\partial C_1}{\partial x} + \frac{\partial}{\partial x} D_{12} \frac{\partial C_2}{\partial x} \tag{2.15}$$

and

$$\frac{\partial C_2}{\partial t} = \frac{\partial}{\partial x} D_{21} \frac{\partial C_1}{\partial x} + \frac{\partial}{\partial x} D_{22} \frac{\partial C_2}{\partial x} \tag{2.16}$$

Assuming parabolic growth, a parametric substitution

$$x = \lambda t^{1/2} \tag{2.17}$$

may be used to transform the last two expressions to O.D.E. The solutions are given by Equations in the form

$$C_A = C_A(\lambda) \tag{2.18}$$

and

$$C_O = C_O(\lambda) \tag{2.19}$$

where the solute metal (A) and oxygen (O) are chosen arbitrarily as the two independent components. λ can be eliminated from the last two equations to obtain the distribution

$$C_A = C_A(C_O) \tag{2.20}$$

which can be plotted on the pertinent A-B-O phase diagram. The locus obtained is termed the " diffusion path ". For a given alloy composition, the diffusion path is unique for a given set of experimental conditions.

Kirkaldy and Brown[64] have developed seventeen useful theorems pertaining to the construction of the diffusion paths in ternary multi-phase systems. The most important rules are : (1) the diffusion path must shift away from the component which is preferentially oxidized and (2) it must cross at least once or coincide with the straight line joining the oxygen corner of the phase diagram to the alloy bulk composition. The second rule is applicable to semi-infinite solid-state couples only.

Fig. 2-1 is an isothermal section of a hypothetical phase diagram (A-B-O) on which two possible diffusion paths are shown and the corresponding concentration profiles across the scales. Path P_1-Q_1-T_1-S_1-O_1 enters a two-phase region coinciding with a tie line. Consequently, only single-phase layers exist separated by planar interfaces. Path P_2-R_2-Q_2-T_2-S_2-O_2 crosses tie lines in a two-phase region which implies the existence of " supersaturation " in the alloy diffusion zone. The supersaturation is relieved by morphological breakdown of the interface and/or internal oxidation. A path, which is calculated based on the assumptions of the existence of planar interfaces and single-phase regions only and is found to enter a two-phase region, is termed " virtual diffusion path ". Following the method developed by Kirkaldy[65], the actual path

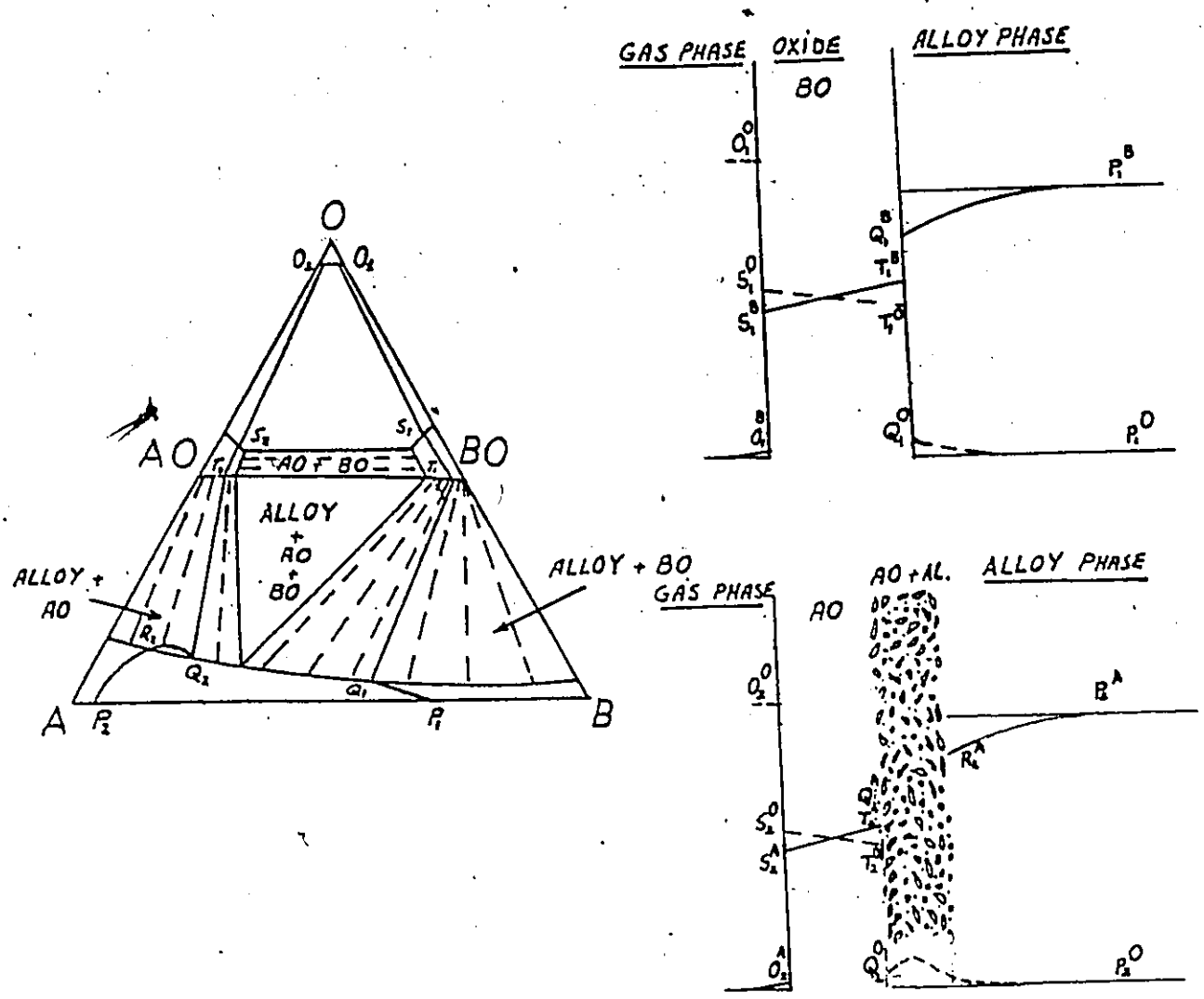

Fig.2-1. Hypothetical diffusion paths and corresponding concentration profiles across the scales. Path $P_1Q_1T_1S_1O_1$ involves planar interfaces only; $P_2R_2Q_2T_2S_2O_2$ is a "virtual" diffusion path involving an internal precipitation zone.

may be calculated by reformulating the problem taking into account the presence of a precipitation zone, assuming that the compositions of the precipitates and the matrix and their relative amounts are known. The diffusion path concept has been used by Dalvi and Coates to interpret the oxidation behavior of Ni-Fe and Ni-Cr alloys [66].

2.5.2 Internal Oxidation

When there is a large difference in the free energy of formation of the oxides of alloy components, the one having a lower free energy is selectively oxidized providing that the oxygen partial pressure in the ambient atmosphere is greater than its dissociation pressure but smaller than the other. The oxide may be precipitated internally. The criteria necessary for the occurence of internal oxidation are summarized in the following :

- Oxygen should be soluble in the alloy to the extent that its inward diffusion to the bulk of the alloy is much faster tnan the outward diffusion of the less noble metal to the surface. This implies that

$$D_O N_O >> D_A N_A \qquad (2.21)$$

- Since internal oxidation is a nucleation and growth process, the concentration of oxygen and the less noble metal should exceed the oxide solubility product.
- According to Wagner [67], the alloy bulk concentration of the less noble metal must not exceed a critical value, N_A^*, which causes the transition from internal to external oxidation. More recently, Smeltzer and Whittle [68] expanded this analysis by

treating the binary alloy plus oxygen as a true ternary system to include the effect of both metal and oxygen gradients in the alloy on the oxygen flux. The limiting bulk concentration of the selectively oxidized solute can then be ascertained in terms of metal and oxygen diffusivities in the alloy, the Wagner interaction coefficient between oxygen and solute and the parabolic rate constant of recession of the alloy/oxide front.

- A strong interaction between oxygen and solute favors internal oxidation since it results in a maximum in the oxygen distribution. This factor reflects the interdependence between the thermodynamic properties of the system and its diffusion behavior.

Rapp[69] has reviewed the models advanced to describe internal oxidation and extended them to describe simultaneous internal oxidation and external scale formation[70].

CHAPTER 3

LITERATURE REVIEW

3.1 PROPERTIES AND APPLICATIONS OF NICKEL SUPERALLOYS

Nickel superalloys are used as construction materials for gas turbine engines either for aircraft or industrial applications, coal combustion furnaces and high temperature reactors for electric power generation. They consist essentially of a Ni-rich matrix, called gamma, which has a disordered f.c.c. lattice. Several elements and compounds are added to impart desired properties to the alloys :

- Al forms a precipitation-hardenable Ni_3Al phase termed gamma prime[1]. The effective role of the precipitates in increasing alloy strengh is by acting as obstacles to dislocation motion which depends on the coherency between the matrix/precipitates and particle spacing. Ti is added to control the lattice mismatch between the precipitates (γ') and the matrix (γ) since it dissolves in the (γ') phase substituting Al atoms to form $\{Ni_3(Al,Ti)\}$. Upon aging, the growth of fine precipitates within the (γ') particles is accompanied with a loss in coherency[71-73]. It was concluded that the fine precipitates are (γ) phase which forms during cooling due to the decrease of Ni solubility in the (γ') phase.
- Refractory metals (Mo, W, Ta, Nb, etc.) are added to act as solid solution hardeners.[1].

- Carbides of refractory metals and Cr act as dispersion strengtheners and inhibibitors to grain boundary sliding[1].
- Matrix reinforcement with Al_2O_3 or ThO_2 particles and Al_2O_3 filaments has been successfully used to improve the mechanical strength of the alloys[2,3].
- Cr is added to improve the oxidation resistance. Fig. 3-1 is an isothermal section in the Ni-Cr-O phase diagram at 1273 K[74]. It indicates that alloys with compositions greater than few ppm Cr form Cr_2O_3 at equilibrium. However, Cr_2O_3 is precipitated internally in this case . Concentrations greater than 15 at.% Cr are used to insure the formation of a continuous protective scale.At high temperatures, the formation of several volatile oxide species of Cr with a general formula Cr_xO_y results in the loss of the protective element and the deterioration of the oxidation properties of the alloys[4]. Conversely, excess Cr has deleterious effects on the mechanical properties since it promotes the formation of embrittling phases having a plate-like morphology which enhances crack nucleation and propagation[1]. The aforementioned drawbacks pose serious problems on the use of Ni alloys designed to form a Cr_2O_3 scale.

Al is apotential competitor to Cr with respect to corrosion protection since volatilization of Al_2O_3 in oxidizing atmospheres is minimal[5] and diffusion of either Al or O in Al_2O_3 is much slower than Cr in Cr_2O_3[6,7]. A concentration exceeding 28 at.% Al is required to form a continuous Al_2O_3 scale on Ni-Al alloys at 1273 K in oxygen atmosphere[75]. Alloys

with high Al content are brittle and pose serious problems in their fabrication and use. However, the addition of Cr reduces substantially the amount of Al required to form a continuous Al_2O_3 scale[75,76]. See Fig.3-2 where the oxides in equilibrium with Ni-Cr-Al alloys are mapped on the ternary phase diagram.

Because of the protective properties of Al_2O_3 scales, coatings based on nickel aluminides are frequently used to improve the environmental resistance of high strength alloys. This topic has received considerable attention in the literature[8-15]. Coating procedure consists of depositing a layer of Al on the alloy substrate, followed by a diffusion treatment which results in the formation of an aluminide layer composed of Ni-Al intermetallic phases. Different methods are used to produce a diffusion coating on Ni superalloys. The most important are : Pack cementation, metal or slurry spraying, hot dipping, electrodeposition, electrophoresis and hot pressing. Depending on the Al activity in the reaction mixture, one of two distinct microstructures is obtained after the diffusion treatment[9-11]. They are shown in Fig.3-3.

In oxidizing environment, nickel aluminide coatings form a protective Al_2O_3 scale. Coating degradation occurs when oxides other than Al_2O_3 become stable due to Al depletion. Several researchers[13,14] have argued that the depletion is due to the inward diffusion of Al in the alloy substrate during service, as evidenced by electron microprobe studies[9,14]. Accordingly, " diffusion barriers " formed in a separate pro-

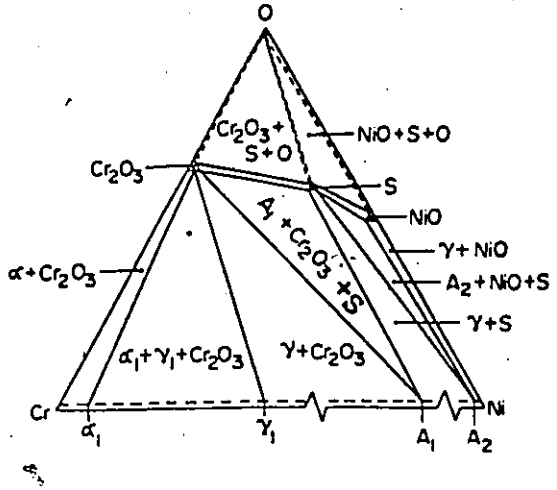

Fig.3-1. Isothermal section in Ni-Cr-O phase diagram at 1273 K[74]; A_1=few ppm Cr.

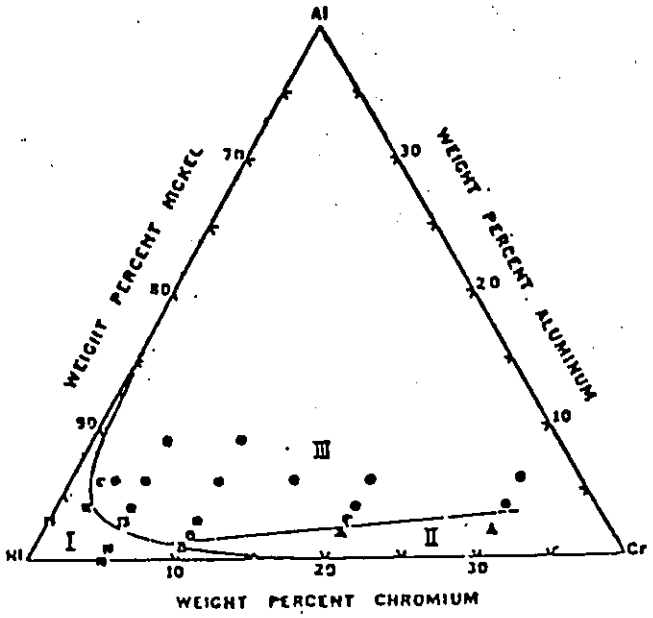

Fig.3-2. Oxide "mapping" for Ni-Cr-Al system at 1273 K[75].
I = Al_2O_3 internal precipitates,
II = Cr_2O_3 layer,
III = Al_2O_3 layer.

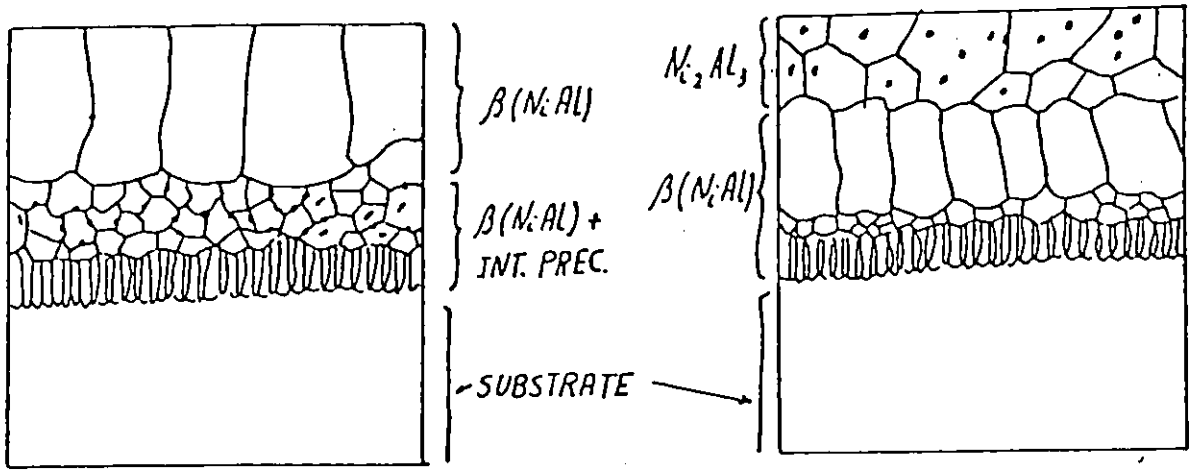

Type (I): Low Al activity

Type (II): High Al activity

Fig.3-3. Microstructures of nickel aluminide coatings[9-11].

cess by coating with metals, which inhibit Al diffusion such as Pt, Cr and Ta, were suggested to increase coating life[13]. Al depletion is more likely due to repeated formation and spallation of the Al_2O_3 scale[8-11,14]. Spalling may be due to stresses arising from cyclic operation or phase transformation as discussed in the next section.

3.2 PROPERTIES OF Ni-Al ALLOYS

3.2.1 Crystal and Defect Structures

The phase diagram of the Ni-Al is well known[77]; see Fig.3-4. Ni and Al are f.c.c. metals. The atomic radius of Al is 14.9% larger than that of Ni[78]. At 1473 K, up to 17 at.% Al can be dissolved in Ni to give a disordered f.c.c. solid solution (γ). Also of interest are the intermetallic phases Ni_3Al (γ'), NiAl (β) and Ni_2Al_3 (δ) because of their wide use as protective coatings as discussed earlier. These phases are characterized by wide homogeneity ranges. Ni_3Al (γ') has a f.c.c. superlattice analogous to Cu_3Au with Al atoms occupying the cube corners and Ni atoms the centers of the faces in the ordered lattice[79]. The stoichiometric composition of the NiAl phase (β) has a CsCl structure with one type of atoms occupying the cube centers and the other the corners[80]. Ni_2Al_3 (δ) has a tetragonal structure[81].

Hughes et al.[80], using X-ray diffraction techniques, measured the compositional dependence of the lattice parameter of the (β) phase. Their results indicate a maximum value at the stoichiometric composition and a linear drop on both sides. They concluded that on the Ni-rich side, Al atoms are substituted by

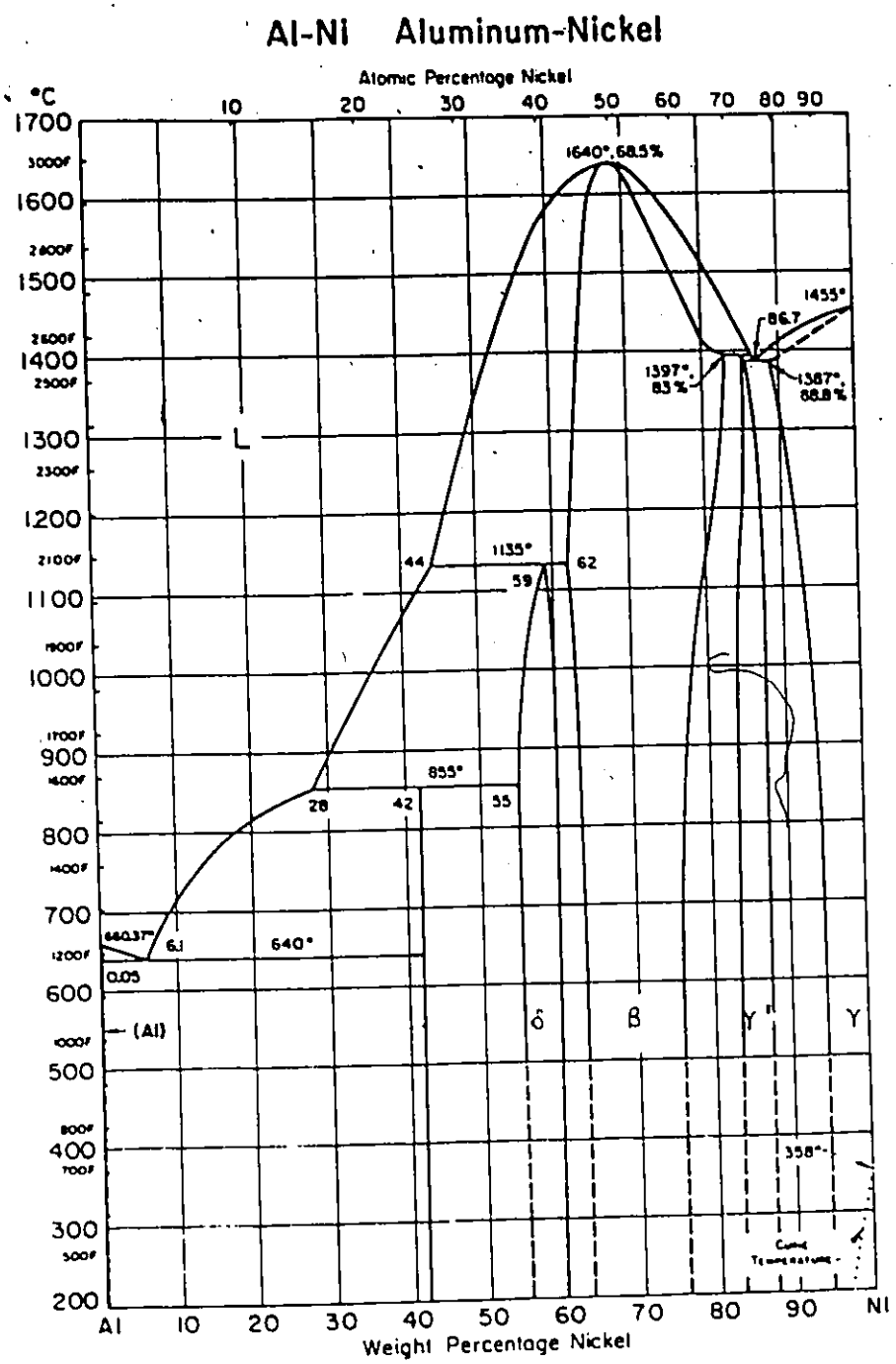

Fig.3-4, Ni-Al phase diagram[77].

the smaller Ni atoms, while on the Al-rich side, Ni vacancies are formed. These results have been confirmed by Taylor et al.[81].

Voids and vacancy dislocation loops have been observed in as grown or as cast (β) NiAl single or polycrystals[82-84]. Furthermore, it was found that both types of defects grow during annealing[84,85]. The presence of these defects implies the existence of a large vacancy supersaturation. Fraser et al.[84] have suggested the surface oxidation during annealing as a cause of vacancy supersaturation. The dissociation pressure of Al_2O_3 at the annealing temperature (1100 K), is 10^{-43} atm[86]. Usually annealing is carried out in vacuum not better than 10^{-10} atm ; thence an Al_2O_3 film may form on the alloy surface by selective oxidation. In the absence of sinks, vacancies, formed by the outward diffusion of Al to the surface, condense into voids when their concentration exceeds the saturation limit[84].

3.2.2 Martensitic Transformation

Rosen and Goebel[87] have observed a martensitic phase when Ni-Al alloys with compositions greater than 63 at.% Ni are quenched from high temperature. This topic has also been studied by Smialek and Hehemann[88] using resistivity measurements and metallographic techniques. They concluded that no martensite forms in the case of the stoichiometric composition of the (β) NiAl phase because of the high resistance to shearing and the strong ordering forces between Ni and Al atoms. Smialek[89] pointed out that stresses associated with a martensitic trans-

formation may contribute to the spalling of the protective Al_2O_3 scale formed on Ni aluminide coatings and thus lead to their degradation.

3.2.3 Thermodynamic Properties

Steiner and Komarek[90] have determined the aluminum activities in Ni-Al alloys using solid/gas equilibration techniques. Nickel activities were calculated by integrating Gibbs-Duhem equations[91]. These results, which are shown in Fig.3-5, indicate a negative deviation from ideality. Furthermore, there is a tremendous change in aluminum and nickel activities within the (β) phase. Using a molten electrolyte galvanic cell ($AlCl_3$ in NaCl,KCl), Schaefer[92] determined the activities in the same system. From the experimental data, excess and partial molal free energies were calculated. The activity results agree with those determined by Steiner and Komarek. The heats of formation of Ni-Al alloys have been determined calorimetrically by Kubaschewski[93]. The thermodynamic properties of Ni and Al have been tabulated in recent references[94,95].

3.2.4 Diffusion Properties

The Ni-Al system has been the subject of several diffusion studies[96-100]. A list of the available diffusion data is given in Table 3-1.

Janssen and Reick[96] have measured the interdiffusion coefficients of the Ni-rich and intermediate phases using diffusion couples. They were calculated using the Boltzman-Matano

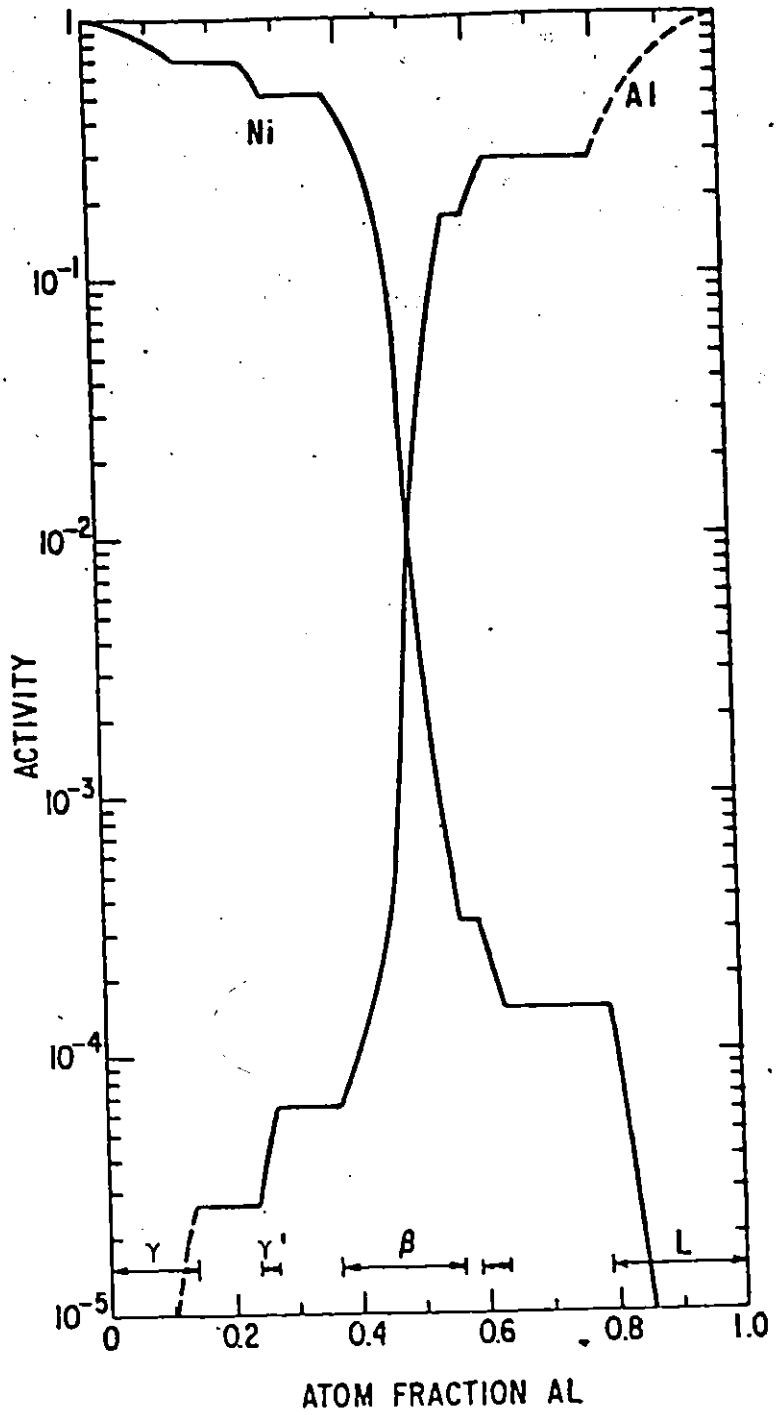

Fig.3-5. Ni and Al activities in Ni-Al system at 1273 K (90,91).

method from the concentration profiles of the diffusing species measured with an electronprobe microanalyzer. These data have been re-evaluated by Janssen[97] in a recent publication. From the location of inert markers (W wires 0.01 mm thick) in the diffusion zone, they concluded that in alloys richer in Ni than the stoichiometric composition of the (β) phase, Ni diffuses much faster than Al; while Al is much faster in compositions richer in Al. Enhanced diffusion along grain boundaries in Ni_3Al (γ') has been observed. Below 1273 K, the activation energy for diffusion was calculated as 50 kJ/g mol compared with 267 kJ/g mol at higher temperatures.

Table 3-1
Diffusion Data for Ni-Al Alloys

at.% Ni	T (K)	Phase	D_o (cm^2/sec)	E (kJ/g mol	D (cm^2/sec) (1473 K)	Ref.
100	1273-1673	Ni	10	253	$D^*=1.0\times10^{-8}$	(6)
92-98	1533	(γ)			$D^*=1.3\times10^{-9}$	(98)
86	1273-1573	(γ)		272	$\tilde{D}=1.4\times10^{-9}$	(97)
75	1273-1573	(γ')		267	$\tilde{D}=1.5\times10^{-11}$	(97)
73-76	1173-1573	(γ')	2.84	303	$D^*=5.0\times10^{-8}$	(99)
62	1273-1573	(β)		230	$\tilde{D}=1.1\times10^{-8}$	(97)
0	723 - 923	Al	1.7	142	-	(6)

(D^* and $\tilde{D}$ are tracer and chemical diffusion coefficient, respec.)

Using a radioactive tracer (Ni^{63}), Wittenberger[98] did not find a compositional dependence of the diffusion coefficient in the Ni-rich phase (γ) within experimental accuracy. Also no dependence was observed in the Ni_3Al phase (γ')[99]. The self diffusion coefficient of Ni in this phase was found to be one order of magnitude smaller than in pure Ni. The author[99] concluded that it may be due to the large energy for vacancy

migration in the highly ordered phase. The recent study of Delavignette et al.[100] has shown that vacancies in the NiAl phase (β) form triangular arrays on the (111) planes after heat treatment. This ordering may explain the unexpected non correspondence between vacancy concentration and diffusion.

3.3 PROPERTIES OF Ni-O SYSTEM

Considerable information exists in the literature on the Ni-O system. In this review, only studies pertinent to the oxidation of Ni are included in the bibliography. For a complete list of references, the reader is referred to recent reviews[7, 43,46,62,101]

3.3.1 Crystal and Defect Structures

When Ni, which is a f.c.c. metal, is exposed to oxygen, a compact, non volatile oxide film is formed which consists solely of NiO having f.c.c.(NaCl) structure. The solubility of oxygen in Ni is low and the coefficients of thermal expansion of the metal and oxide are almost identical[43]. Electrical conductivity[102] and gravimetric[103] measurements indicate that NiO is a p-type semiconductor exhibiting a small range of non-stoichiometry, $\sim 10^{-4}$ on the metal-deficit side of stoichiometry at 1273 K[104]. Diffusion measurements based on isotope tracer technique[105-108] using Ni^{63} and O^{18} have shown that the diffusion coefficient of oxygen in NiO is two orders of magnitude less than that of Ni. Accordingly, it was concluded that the predominant defects in NiO are nickel vacancies (V_{Ni}) and positive holes (h). There is no agreement on the ionization state of nickel vacancies[103,109,110] and the defect reactions

for NiO are written in terms of singly or doubly ionized vacancies as shown by the following defect equilibria :

$$1/2\ O_2 = O_O^{\times} + V'_{Ni} + h^{\cdot} \qquad (3.1)$$

$$1/2\ O_2 = O_O^{\times} + V''_{Ni} + 2\ h^{\cdot} \qquad (3.2)$$

where $O_O^{\times}$ is a normal oxygen lattice site. The application of the law of mass action to the above reactions leads to the following oxygen pressure-defect concentration relationships :

$$\{V'_{Ni}\} = \{h^{\cdot}\} \alpha (p_{O_2})^{1/4} \qquad (3.3)$$

$$\{V''_{Ni}\} = \{\frac{h^{\cdot}}{2}\} \alpha (p_{O_2})^{1/6} \qquad (3.4)$$

3.3.2 Epitaxial Growth

Many physical properties of the oxide films are found to be related to the metal substrates. In particular, specific relations do exist between their crystallographic orientations. The following epitaxial relationships have been determined for Ni/NiO[46,49,111] :

$(100)_{NiO}$, $(111)_{NiO}$ // $(100)_{Ni}$,

$(100)_{NiO}$ // $(110)_{Ni}$,

and $(111)_{NiO}$ // $(111)_{Ni}$.

During the early stage of oxidation, several other orientations were observed which eventually convert to those shown above.

Several theories have been advanced to explain the observed epitaxial relationships[46]. The most accepted one is based on the least misfit between the two lattices (metal and oxide) in contact at the interface which results in minimizing the interfacial energy. It has been also observed that the oxide orientation is always such that the coincidence of the c.p. directions is maximized.

3.3.3 Oxidation Mechanism

Kinetics

The oxidation kinetics of Ni have been extensively studied over a wide range of temperature and pressure. At high temperatures (T > 1173 K), they have consistently exhibited parabolic behavior[112,113]; whereas at low temperatures (T < 773 K), several rate laws have been observed (logaritmic, cubic,etc.) and have been interpreted by different mechanisms[114-117]. At intermediate temperatures (773<T<1173 K), Ni exhibits a stage of more rapid oxidation before the onset of parabolic kinetics[43-49,118,119].

The initial stage of oxidation of Ni (oxide film thickness range 50-300 nm)has been studied at 773 and 873 K by Perrow et al.[43-45]. The oxide films were found to be composed of small crystallites which grow in size with time. A short-circuit diffusion model based on recrystallization and grain growth of oxide crystallites has been employed to interpret the initial fast non-parabolic oxidation.

Nickel single crystals oxidize at different rates depending on crystallographic orientations[46-49,53,54]. It has been found that the major crystallographic planes in the order of decreasing oxidation rates were (100), (111), (110) and (311). Cathcart et al.[53] found a direct correlation between the oxidation anisotropy and the density of short-circuit paths present in the oxide films formed on the different faces of Ni. The density of easy diffusion paths is determined by the nucleation and growth of the oxide which are orientation dependent. Films

on the (100) plane, which oxidizes the fastest were found to contain a high density of high angle boundaries; while only low angle boundaries existed in the oxide films formed on the (311) plane which oxidizes the slowest. The short-circuit diffusion model has also been employed to interpret the growth kinetics of NiO on monocrystalline and polycrystalline Ni[43-49,118,119].

The structure of NiO films and oxidation kinetics were found to be sensitive to surface preparation techniques[47,120,121], e.g. mechanical, chemical and electropolishing, annealing, cold work, etc. Cold worked Ni oxidizes faster than if it were annealed, forming a fine-grain oxide which coarsens rapidly with time[121].

At high temperatures, the oxidation kinetics follow closely parabolic relationships. According to Wagner's parabolic theory, Sec.2.3, the rational parabolic constant for Ni oxidation is defined by Eq.(2.6). Upon omitting D_O and expressing the self diffusion coefficient of Ni in terms of vacancy concentration ($D_{Ni} = V_{Ni} D_{V_{Ni}}$) and substituting for V_{Ni} from Eq.(3.3) or (3.4), this equation becomes at 1 atm pressure :

$$k_r = 3 \bar{C}_{eq} D^{o}_{Ni} \qquad (3.5)$$

where D^{o}_{Ni} is the diffusivity at 1 atm pressure. The calculated and experimental rate constants are shown in Fig.3-6. The knee in the Arrhenius plot observed at T ≈ 1173 K has been interpreted by the transition from lattice diffusion to grain boundary or surface diffusion as the temperature is lowered.

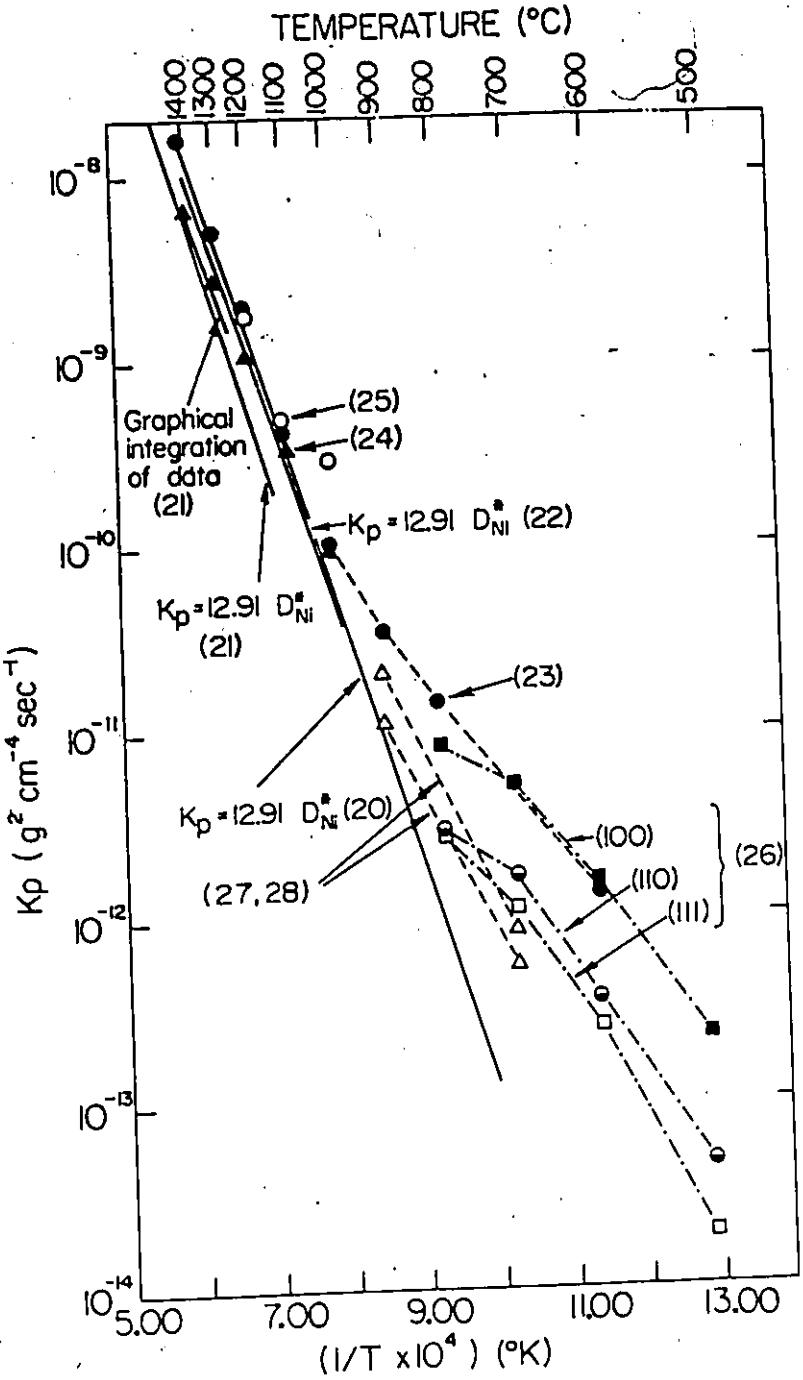

Fig. 3-6. Arrhenius plot of the parabolic rate constants for Ni oxidation. Numbers refer to the bibliography in the review paper by Smeltzer and Young[39] from which this figure was taken.

Scale Morphology

Depending on temperature, metal purity and surface preparation, a duplex or single-layered NiO scale results from the oxidation of Ni[46,62,122-129]. The duplex scale consists of a light-green equiaxed fine-grained inner layer adjacent to the metal and a dark-gray coarse columnar outer layer. Several mechanisms have been advanced to interpret the structure of the NiO scale :

1) Dissociative Mechanism : Startell and Li[122], based on an inert marker experiment, proposed that the outer layer is Ni-deficient and grows by outward migration of Ni ions; while the inner layer is anion deficient and grows by inward diffusion of oxygen ions. The dissociation of NiO at the interface between the two layers assists the diffusion process by providing Ni and O ions. Birks and Richert[123] postulated that the formation of a duplex scale is due to insufficient plastic flow leading to progressive loss of contact between the metal and oxide. In the regions where the scale becomes detached from the substrate, NiO dissociates to give Ni ions and electrons which migrate outwardly and O molecules which react with the metal. The presence of pores in the inner layer, assumed to be due to the dissociation process, provides open channels for O diffusion. Grain boundaries existing in the columnar layer may also contribute to O transport. Evans et al.[124] have explained the transition from a duplex structure to a single columnar layer at high temperatures by the increase in oxide

plasticity which favors the anhilation of cavities formed at the metal/oxide interface and maintaining good contact between the scale and substrate.

2) Recrystallization Mechanism : Rhines and Wolf[125] have evoked a model based on the recrystallization of NiO film driven by growth stresses. Since NiO is a cation conductor, Pilling-Bedworth argument for the cause of stress in scales is not applicable. The stresses, if any, can be relieved at the oxide/gas interface. However, the authors suggested that enormous stresses can be generated as O, which diffuses inwards along grain boundaries in the columnar layer, reacts with the flux of Ni ions at these boundaries. The accumulation of oxide in the vicinity of the boundaries establishes a stress gradient across the scale and causes oxide recrystallization at the metal/oxide interface.

3) Recrystallization and Grain Growth : Manolescu and Smeltzer[62] have interpreted the oxidation kinetics and scale microstructure based on a model which involves recrystallization and grain growth of oxide film.

3.4 PROPERTIES OF Al-O SYSTEM

3.4.1 Thermodynamic Properties

Al_2O_3 is the only thermodynamically stable solid oxide in the Al-O system[126] and exists in several polymorphic modifications[127,128]. At low oxygen pressure ($<10^{-8}$ atm) or in reducing atmosphere and at high temperatures (>1973 K), the existence of Al suboxides (Al_2O and AlO) in the vapor phase is well established[5,126,129].

An amorphous Al_2O_3 film is formed when Al is oxidized below 673 K[130]. At higher temperatures, γ-Al_2O_3 nucleates and grows beneath the amorphous film[130]. The γ-phase, which has a spinel structure with the tetra and octahedral interstices partially filled with Al ions[131], is also obtained by calcining amorphous or crystalline hydrated Al_2O_3 at temperatures lower than 1223 K[127,128]. The other modifications (χ,κ,δ and θ-Al_2O_3), which are formed during the successive irreversible transformations leading to α-Al_2O_3, are believed to have structures closely related to γ-Al_2O_3[132]. α-Al_2O_3 (corundum), which has a hexagonal close-packing of O ions with Al ions occupying 2/3 of the octahedral interstices is thermodynamically stable at temperatures higher than 1223 K up to its melting point (2323 K)[32,133]. The transformation γ-Al_2O_3 → α-Al_2O_3 is accompanied by a reduction of 14.3 % in volume[133].

α-Al_2O_3 is a very stable oxide phase having extremely low dissociation pressures[86,95] and vapor pressures[5] over a wide range of temperatures. The vapor pressure is < 10^{-10} atm at 2273 K. However, volatilization of Al_2O_3 as Al and Al_2O becomes appreciable at 2273 K in H_2/H_2O atmospheres[5]. The standard free energy of formation of α-Al_2O_3 at high temperatures has been determined by Gosh and Kay[134] using a solid electrolyte. The thermodynamic data for the Al-O system has been compiled in recent monographs[95,135].

3.4.2 Oxidation Properties of Al

The structure and morphology of Al_2O_3 films formed on

Al have been extensively studied by Doherty and Davis[130] using TEM. They have demonstrated that Al forms an amorphous Al_2O_3 film if oxidized below 673 K; whereas at higher temperatures, γ-Al_2O_3 crystallites nucleate and grow beneath the amorphous film. It has been argued that the amorphous film grows by outward diffusion of interstitial Al ions and electrons[131,136]. The formation of γ-Al_2O_3 crystallites beneath the amorphous film, inferred from strong epitaxial growth, has been considered as an evidence for oxygen migration through both films; though it is believed that oxygen migration in the amorphous film involves structural imperfections only[137,138].

At room temperature, the growth of the amorphous film follows an inverse logarithmic relation; whereas at elevated temperatures ($T < 573$ K), a parabolic relation is observed[136, 139]. Assuming Al ion diffusion through the oxide film as rate controlling step, Smeltzer[136] has shown that film growth can be adequately interpreted by Mott and Cabrera theory[40,41]. Based on the same assumption and using arbitrary parameters, Dignam et al.[137] have derived the following expression which fits the experimental data over the whole range of film thicknesses :

$$\frac{dx}{dt} = 2\,A\,\sinh(B/x) \qquad (3.6)$$

where A and B are experimetally determined parameters.

At $T > 673$ K, no single kinetic expression satisfies the experimental results over the entire range of film thicknesses. Three stages were observed : a fast, but declining, initial rate

followed by a second linear stage that subsequently decreased to a very slow third stage[130,136-138]. It has been suggested[130] that the first stage corresponds to the formation of a continuous amorphous film, the second involves the nucleation and lateral growth of γ-Al_2O_3 beneath it and the third involves the thickening of the crystalline film. Based on Doherty and Davis[130] metallographic observations, Dignam et al.[137] have advanced a model to interpret the oxidation kinetics of Al under these experimental conditions. They have assumed that oxygen migration through the amorphous film, which leads to the nucleation and growth of γ-Al_2O_3 crystallites, occurs through " faulted boundaries " in the film close to the periphery of the crystallites. These imperfections may arise as a consequence of the difference between the specific volumes of the two phases. An essentially similar model has been advanced by Beck et al.[138] to interpret the oxidation kinetics of Al and dilute Al-Cu alloys.

3.4.3 Defect Structure and Transport Properties of α-Al_2O_3*

The defect structure of Al_2O_3 is a matter of conjecture in the literature. However, available electrical conductivity and diffusion data[55,56,140-142] indicate that it exhibits an extremely small nonstoichiometric range.

Large discrepancies exist in the reported electrical conductivity data for Al_2O_3. The results are presented in Fig. 3-7. Possible reasons for these differences would be the presence of alliovalent impurities which can critically affect the defect-

* All subsequent entries of Al_2O_3 are implied to mean α-Al_2O_3.

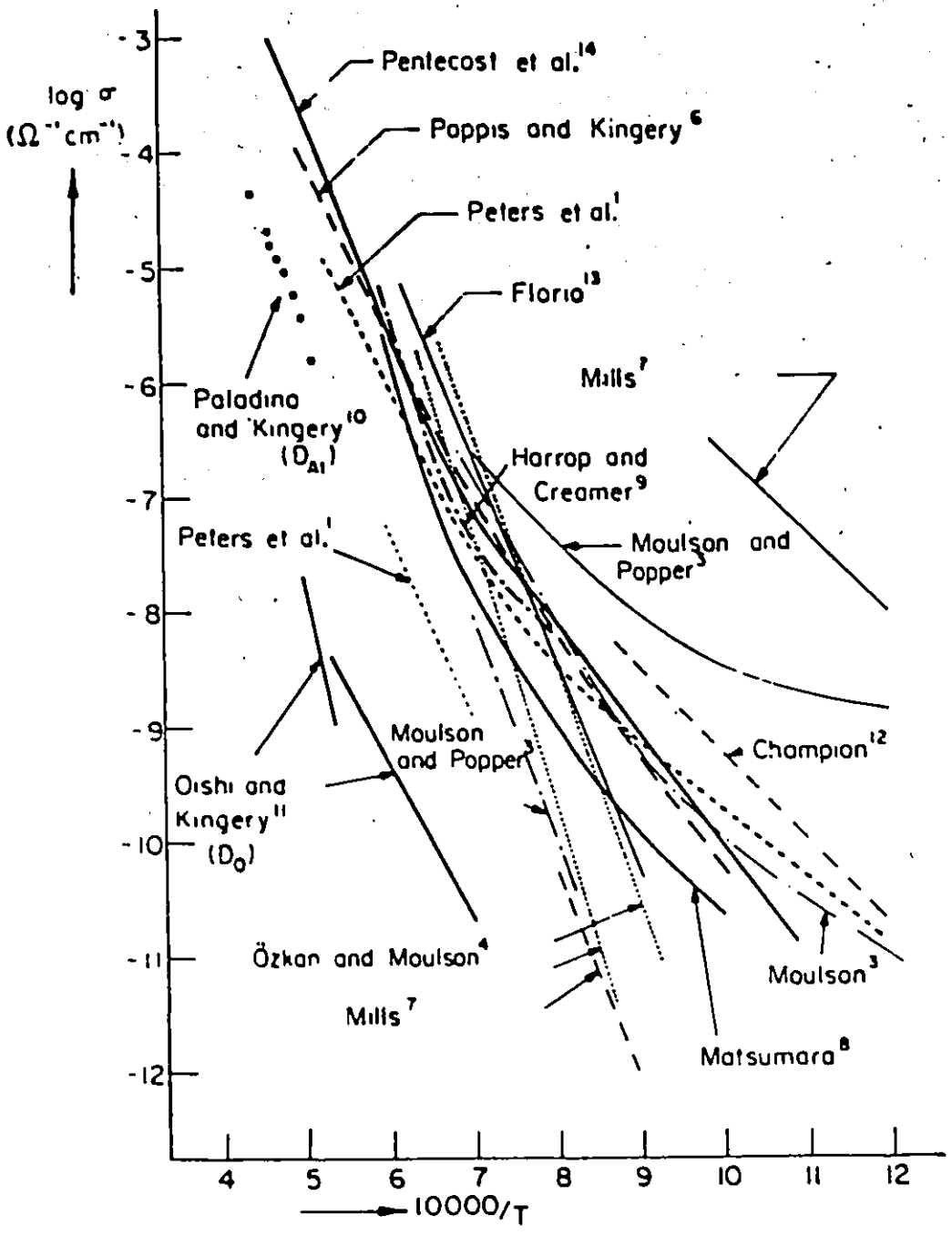

Fig.3-7. Specific conductivity of Al_2O_3 reported in the literature. Numbers refer to the bibliography in Brook et al's paper[142] paper from which this figure was taken.

dependent properties, gas leakage and surface or grain boundary conduction[141,142]. Schmalzried[143] concluded from solid-state e.m.f. cell studies that Al_2O_3 is an electronic conductor above 1573 K; while it is a mixed conductor at lower temperatures. Using volume guards against surface and gas conduction, Kröger et al.[142] concluded that Al_2O_3 single crystals are ionic conductors with $Al^{3\cdot}$ as the principle charge carrier at high oxygen activities and high temperatures (T > 1723 K). These findings are not in agreement with Pappis and Kingery[140] measurements which inferred that Al_2O_3 is n-type at low oxygen potential (10^{-10} atm < p_{O_2} < 10^{-6} atm) with $Al^{3\cdot}$ or $V_O^{\cdot\cdot}$ as possible point defects and p-type at high oxygen potential (10^{-4} atm < p_{O_2} < 1 atm) with $V_{Al}^{'''}$ as possible defect. At intermediate oxygen potentials, the conductivity is ionic and the ionic range becomes narrower as the temperature is raised. No volume guards were used in that study.

Kingery et al.[55,56] have determined the tracer diffusion coefficients of Al and O in Al_2O_3 using Al^{26} and O^{18} isotopes. Their results are shown in Fig. 3-8. Three conclusions can be made :

1) Both Al and O are mobile in Al_2O_3 . However, the diffusion coefficient of Al is approximately one order of magnitude greater than that of O at the same temperature and the activation energy for Al bulk diffusion is about 2/3 of that for O diffusion.

2) Diffusion of O is structurally sensitive. The activation energy for O diffusion in polycrystalline samples (average

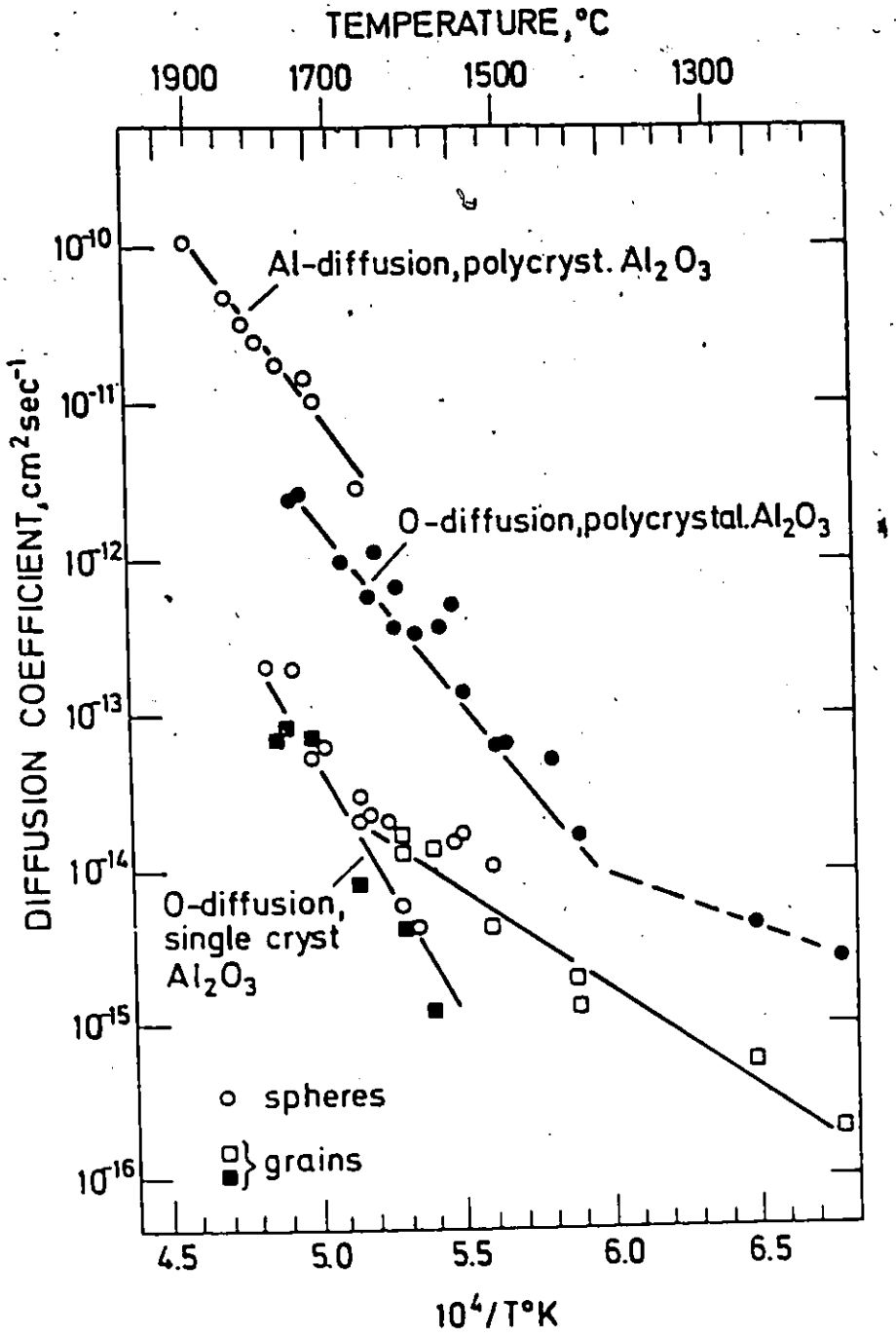

Fig.3-8. Aluminum and oxygen tracer diffusion coefficients in Al_2O_3 (55,56).

grain size 30 μm) is one half of that for single crystals. Al diffusion in single crystals has not been determined.

3) The diffusivities are impurity-sensitive.

The properties of Al_2O_3 have been compiled in a recent monograph[144].

3.5 OXIDATION PROPERTIES OF Ni-Al AND Al_2O_3-FORMING ALLOYS

Ni-Al alloys without additions have been the subject of few oxidation studies[16-22]. In this section, alloys containing Al other than Ni-Al are also reviewed since it is believed that the study of these systems might provide useful data for the elucidation of the growth mechanism of protective Al_2O_3 scales. Nevertheless, measurements or observations related to these systems must be interpreted with care since the presence of additional components complicates the analysis due to the formation of additional phases and the doping of Al_2O_3 with allio-valent elements can critically affect its defect-dependent properties.

The review is classified for convenience in three sections according to the morphology of Al_2O_3 formed on the alloys, namely : internal precipitation, imperfect discontinuous scale and protective continuous scale. A summary of the experimental results on the oxidation of Ni-Al alloys and Al_2O_3-forming alloys other than Ni-Al is presented in Tables 3-2 and 3-3, respectively.

3.5.1 Internal Precipitation

The oxidation rates of Ni-Al alloys with Al concentration

less than 4 wt.% are greater than those of pure Ni. The reaction kinetics can be presented by parabolic relationships[16-18]. There is a small dependence of the oxidation rate on oxygen pressure[17] and alloy composition[18] with the exception of very low Al concentration (< 0.5 wt.%). The oxidation products formed on these alloys consist of an external NiO scale and an internal Al_2O_3 precipitation zone[16,18]. The outer region of the external scale, which is virtually pure NiO, has a coarse columnar structure. The inner region, which is doped with Al, is porous and has a finer grain size. $NiAl_2O_4$ is believed to form at the scale/subscale interface[16] and within the inner part of the external scale especially in the case of alloys with high Al content[18].

The increase in the oxidation rate accompanying the addition of Al has been attributed to the doping effect of Al on NiO which results in an increase in the concentration of Ni vacancies[16,18]. It has been postulated that the presence of $NiAl_2O_4$ precipitates and pores in the inner layer may interfere with the outward diffusion of Ni[18] and that gaseous transport of oxygen may occur through the pores[16,18]. It has been suggested that the dissociation of NiO at the scale/subscale interface, which presumably results in the porosity of the inner layer[16], supplies the oxygen necessary for the growth of the Al_2O_3 precipitates[16,18].

3.5.2 Imperfect Discontinuous Scale

With the exception of one study[19], this topic has

received little attention to the present. Alloys with Al composition in the range of 5 to 7 wt.% form an Al_2O_3 film with NiO nodules scattered in it[16,19,20]. The nodules have the same morphology as the external scale formed on alloys with lower Al content[18,19]. Either internal precipitates or a thin discontinous film of Al_2O_3 are observed beneath the nodules[16,19]. It was suggested that the transition from internal precipitation to growth of a continuous film occurs by preferential precipitation of Al_2O_3 particles at alloy grain boundaries[18,19].

This type of scaling is accompanied with irreproducible kinetics and is sensitive to sample preparation techniques[16,19]. The kinetics show the characteristics of " breakaway oxidation ", namely : initial parabolic stage with a very low oxidation rate, followed by a linear stage with a much faster rate and a final rate declining stage[16,19]. Breakaway kinetics were not observed in one study[20]; however, deviation from parabolic behavior was reported in this case.

A mechanism, which is based on mechanical breakdown of an initial protective Al_2O_3 scale, has been advanced to account for the above observations[16,19]. The breakdown was ascribed to the formation of oxide phases other than Al_2O_3 (i.e. NiO and $NiAl_2O_4$ - which have different equivalent volumes) due to Al depletion by selective oxidation[16] or to stresses developed in the Al_2O_3 film overlaying an Al-depleted alloy surface and which are not completely relieved by plastic deformation[19].

3.5.3 Protective Continuous Scale

Alloys forming Al_2O_3 [23-29] have been reported to oxidize parabolically after a transient stage during which Al_2O_3 as well as other oxides are formed. However, parabolic behavior was usually observed for relatively short period followed by gradual deviation [24,26,28].

Only recently, researchers have identified the volatilization of Pt used as suspension wire as a source of error in thermogravimetric analysis [26,27]. In order to overcome this problem and whenever several oxides were formed, the kinetics were determined by scale thickness measurements [26] or quantitative X-ray diffraction [21,24]. Uneven scale thickening at oxide grain boundaries and over coexisting alloy phases posed some difficulties [26]. These measurements also indicate that Al_2O_3 scalesthicken parabolically for short periods [21,24] and deviate considerably from parabolic behavior after long time [26]. The activation energy for Al_2O_3 growth varies from 209 to 356 kJ/g mol [21,22,24-26].

Though several alloy systems were studied, there are some common metallographic observations relevant to Al_2O_3 scale growth :

- The initially formed oxide film is free from structural features [22]. Thicker films are textured having fine dimples [23-26] and a lacey or cellular structure [22,29].
- Formation of faceted small voids or large smooth areas with step-like striations at the alloy/scale interface [21-28]. The latter were observed to coincide with wrinkles in the scale [23, 25,27,28]. It was also found that the wrinkles are associated

with polishing marks on the surface[27] and that electropolishing tends to reduce their density[25].

- Variation of oxide grain size across the scale in the region of convolutions; the grains are finer at the scale/gas surface than at the inner interface[28].

- Growth of oxide filaments (whiskers) at the scale/gas interface[21,23,28].

- The Al_2O_3 scale inevitably spalls during cooling[21,23-28]. In this respect, it was found that the addition of small amounts of reactive metals, e.g. Y, Hf, Sc, Th, etc., improves scale adherence[23-25,27,28].

Finally, the properties of the oxides in the Ni-Al-O system are summarized in Table 3-4.

Table 3-2

Summary of Experimental Results of Previous Investigations on the Oxidation of Ni-Al Alloys.

Conc. Al wt.%	T (K)	P_{O_2} (atm)	$(\Delta W/A)^n = k\,t$ n	k $(g.cm^{-2})^n sec^{-1}$	Remarks	Ref.
Pure Ni	1273	1	2.0	1.0×10^{-10}	-Parabolic kinetics, T>1273 K.	(38)
	1373	"	"	4.5×10^{-10}		
	1473	"	"	2.0×10^{-9}		
γ-Phase 1.8	1273	1	1.6	2.8×10^{-9}	-Approximate parabolic kinetics.	(17)
	"	10^{-2}	"	1.1×10^{-9}	-Slight dependence of k on P_{O_2}.	
	"	10^{-4}	"	1.7×10^{-9}		
3.25	1173	10^{-2}	2.0	1.0×10^{-10}	-Parabolic kinetics	(16)
	1323	"	"	1.0×10^{-9}		
	1473	"	"	7.0×10^{-9}		
0.5	1273	1	2.0	3.3×10^{-10}	-Approximate parabolic kinetics.	(18)
1.0	"	"	1.9	3.7×10^{-10}	-Dependence of k on alloy composition.	
2.5	"	"	2.0	5.0×10^{-10}	-Individual oxide layers thicken parabolically.	
4.0	"	"	1.8	5.8×10^{-10}		
0.5	1473	"	1.8	4.0×10^{-9}		
1.0	"	"	1.8	5.5×10^{-9}		
2.5	"	"	1.9	7.0×10^{-9}		
4.0	"	"	1.9	6.0×10^{-9}		
					-External duplex scale : outer layer pure NiO, inner layer Al-doped NiO or $NiO+NiAl_2O_4$; Al_2O_3 precipitated in alloy.	(16), (18)
5.0	1173	0.13		3.0×10^{-12}	-Parabolic kinetics preceded by a non-parabolic stage.	(20)
	1273	"		6.0×10^{-12}		
	1373	"		7.5×10^{-12}		
	1473	"		1.0×10^{-11}		
6.0	1273, 1573	0.1		-	-Breakaway kinetics.	(16)
7.0	1273, 1473	1		-	-Breakaway kinetics; dependence on surface preparation.	(19)
					-Scale consists of Al_2O_3 film with NiO nodules scattered through it.	(16), (19), (20).

(Continued)

Table 3-2 (Continued)

γ'-Phase (Ni$_3$Al)						
12.5	1273, 1473	1		-	-Kinetics sensitive to surface preparation. -Continuous Al_2O_3 scale containing 0.2-0.3 and 0.5-0.6 wt.% Ni at 1273 and 1473 K, resp. -Striated smooth areas at alloy/scale interface. -Small depletion in Al at alloy/oxide interface.	(19)
12.9-13.2	1173	0.21		1.1×10^{-13}	-Parabolic kinetics preceded by non-parabolic stage, t=50 h, E=195 kJ/gmole. -Al_2O_3 only is formed at 1473 K; at lower T, NiO and $NiAl_2O_4$ are also formed. -Al_2O_3 thickens parabolically, t=4 h, E=250 kJ/gmole. -Voids at alloy/oxide interface and whiskers at scale/gas interface.	(21)
	1273	"		5.3×10^{-13}		
	1373	"		2.0×10^{-12}		
	1473	"		7.1×10^{-12}		
β-Phase (NiAl)						
25	1273	0.1	2.0	8.0×10^{-14}	-Parabolic kinetics, t=20 h, E=265 kJ/gmole. -Al_2O_3 is the only oxide formed.	(16)
	1373	"	"	4.0×10^{-12}		
	1473	"	"	5.0×10^{-12}		
	1573	"	"	1.0×10^{-11}		
25 ➡	1373	0.21		-	-Approximate parabolic kinetics, t=100 h, for both isothermal and cyclic tests. -Initial thin tranparent oxide film which subsequently transforms to a textured film having a "lacey" structure. -Polyhedral voids at alloy/oxide interface; total cavity volume continuously increasing with time. -Observations on oxide grain growth.	(22)

Table 3-3

Summary of Experimental Results of Previous Investigations on Al_2O_3-Forming Alloys.

System and Alloy Comp. (wt.%)	Alloy Phases	T (K)	P_{O_2} (atm)	Oxide Phases	k ($g^2.cm^{-4}/sec$)	Remarks	Ref.
Fe-25Cr-4Al	sol.sol.	1473	0.1	Cr-doped Al_2O_3	0.8×10^{-11}	-Parabolic kinetics, t=24 h.	(23)
" + 0.1 Y	" +yttrides	"	"	Al_2O_3 + $YAlO_3$	0.4×10^{-11}	-Cr_2O_3 present in transient stage.	
" + 0.2 Sc	" +scandides	"	"	Al_2O_3 + Sc_2O_3	1.8×10^{-11}	-Voids at alloy/oxide interface; nodules fine dimples, and whiskers at scale/gas interface.	
						-Few observations on oxide grain growth.	
						-Pt wire markers reside at scale/alloy (FeCrAlY) interface.	
Ni-10Cr-5Al	γ+γ'	1373	0.21	Al_2O_3+$NiAl_2O_4$	1.7×10^{-12}	-Approximate parabolic kinetics after extended oxidation, t=50 h.	(24)
		1423	"	"	3.0×10^{-12}	-Continuous decrease in the slope of parabolic plots for Y and Th alloys.	
" + 0.5 or 1 Th	"	1473	"	Al_2O_3+$NiAl_2O_4$ +HfO+ThO_2	5.4×10^{-12} –	-Al_2O_3 thickens parabolically, t 10 h, E = 209 kJ/gmole.	
" + 0.5 Y	" + YNi_9	1373-1473	"	Al_2O_3+$NiAl_2O_4$ +HfO+Y_2O_3+ +$YAlO_3$ +$Y_3Al_5O_{12}$	–	-Voids at alloy oxide interface.	
Ni-16Cr-6Al	γ+γ'	1273	0.1	Al_2O_3	3.9×10^{-13}	-Parabolic kinetics up to 100 h, E = 293 kJ/gmole, deviation after longer time.	(25)
		1373	"	"	2.4×10^{-12}		
		1473	"	"	3.0×10^{-12}		
" + 0.1 Y	" +Yttrides	1473	"	Al_2O_3+Y_2O_3 +$YAlO_3$	2.9×10^{-12}	-NiO, Cr_2O_3 and $NiCr_2O_4$ present during transient stage.	
Co-25Cr-6Al	α+β	1273	"	Al_2O_3	1.4×10^{-13}	-Metallographic observations similar to FeCrAl alloy[23]; wrinkling of scale and formation of large oxide crystals at these sites.	
		1373	"	"	9.9×10^{-13}		
		1473	"	"	5.4×10^{-12}		
" + 0.1 Y	α+β +Yttrides	1473	"	Al_2O_3+Y_2O_3 +$YAlO_3$	3.3×10^{-12}	-Y-rich particles extending through scale.	

(Continued)

Table 3-3 (Continued)

Pt-0.5Al Pt-2Al Pt-6Al	sol.sol. " + Pt_2Al Pt_2Al+Pt_5Al	1273 " 1373 1473 1573	0.21 " " " "	Al_2O_3 int.prec. + Pt mounds discont.Al_2O_3 scale cont.Al_2O_3 scale "	- - 2.0×10^{-13} 4.0×10^{-13} 1.5×10^{-11}	-Parabolic kinetics, t=100 h; E = 356 kJ/gmole; deviation after longer time. -Uneven thickening of Al_2O_3 on Pt_2Al and Pt_5Al phases. -Preferential thickening of scale at grain boundaries. -Few observations on oxide grain growth. -Pt volatilization as PtO_2.	(26)
Fe-27Cr-4Al " + 0.8 Y	sol.sol. " + YFe_3	1473 "	1 "	Al_2O_3 doped with Fe and Cr. Al_2O_3+Y-rich oxide	- -	-Convoluted scale; convolutions aligned in the direction of SiC abrasion markings. -Scale wrinkles associated with smooth areas at alloy/oxide interface. -Y-rich particles extending through scale. -Pt volatilization.	(27)
Co-10Cr-11Al " + Y up to 1% " + Hf up to 1.5%	α+β " +Co_3Y α+β	1373 " "	0.21 " "	Al_2O_3 " "	- - -	-Parabolic kinetics, t=100 h; deviation in case of Y and Hf alloys. -CoO and Cr_2O_3 present during transient stage. -Smooth areas with step-like striations at alloy/oxide interface associated with with wrinkles in scale. -Whiskers at scale/gas interface. -Variation of oxide grain size across scale; rapid grain growth. -Al_2O_3 protrusions penetrating in alloy and encapsulating Y-rich internal oxide particles. -Neither Hf nor Y is detected in Al_2O_3 scale except in the region of protrusions	(28)
Pt-22Al	-	1373	0.21	Al_2O_3	2.0×10^{-12}	-Parabolic kinetics after a period of rapid oxidation, t = 40 h. -Uneven thickening of scale and formation of ridges. -Persistent appearance of polishing scratches at scale free surface.	(29)

Table 3-4

Properties of the Oxides in the Ni-Al-O System.

Property	NiO	Al_2O_3	$NiAl_2O_4$
Crystal St.	f.c.c. (NaCl)	amorphous[130] ↓ 673 K γ (spinel) ↓ 1223 K α (hexagonal)[133]	inverse spinel[145] $\{(Al^{3\cdot})_8\}_A\{(Al^{3\cdot})_8(Ni^{2\cdot})_8\}_B\{(O^{2-})_{32}\}$ A, B = tetra, octahedral sites, respectively.
Defect St.	$Ni_{(1-x)}O$, $x \approx 10^{-4}$ T = 1273 K[104]. V_{Ni} + h.	controversial[55,56, 140-143]	Defects on Al and Ni sites, inert marker[146].
Spec.Grav.	6.67[147]	γ 3.60[133] α 3.96[133]	4.50[133]
Th.Exp. Coef. (K^{-1})	1.68×10^{-6} [32]	α 8×10^{-6} [32]	-
M.P. (K)	2263[147]	2323[133]	2293[133]
Vaporization	negligible (T < 1673 K)	nil, oxidizing atm. as Al, AlO, Al_2O T>2000 K in H_2/H_2O[5]	-
$-\Delta F_f$ (1500K) (kJ/gmole O)	108[95]	797[95]	658[145]
Sol.of Al or Ni (wt.%)	0.7, T=1673 K[148]	< 1, T=1473 K[19]	Ni insoluble, Al soluble[149].

(Continued)

Table 3-4 (Continued)

D (1473 K) (cm^2/sec) E (kJ/gmole)	$D_{Ni}(s,p)=10^{-11}$ (105,108) E=185(105), 240 (108) $D_O(s)=10^{-13}$ (107) $E=240$(107)	$D_{Al}(p,130-200\mu m)=2\times10^{-16}$ E=475 (56). $D_O(s)=10^{-19}$ E=635 $D_O(s,d)=2\times10^{-16}$ E=240 $D_O(p,20-30\mu m)=2\times10^{-15}$ E=460 (55).	$D_{Ni}=7\times10^{-13}$ (34) $D_{Ni}>D_{Al}$ (146) E=225 (150).

F_f = free energy of formation, E = activation energy for diffusion, s = single crystal p = polycrystalline, d = doped.

CHAPTER 4

EXPERIMENTAL PROCEDURES AND TECHNIQUES

4.1 INTRODUCTION

A variety of experimental techniques was used for preparation and analysis of materials, oxidizing the specimens and characterization of oxidation products. These techniques include electrical arc melting, annealing and homogenization, chemical analysis, thermogravimetric analysis, inert marker measurements, optical microscopy, X-ray diffraction and topography, electron metallography (TEM, SEM, EPMA and AES) and ion sputtering techniques.

4.2 SAMPLE PREPARATION AND ANALYSIS

4.2.1 Sample preparation for Oxidation Experiments

Ni (99.99% purity) and Al (99.95% purity) used in this investigation were supplied by Falconbridge and Alcan Companies, respectively. Chunks of each metal were mechanically cleaned and accurately weighted to yield alloys with nominal compositions of 2, 6 and 32 wt. % Al . The total weight of each batch was approximately 40 gm. The alloys were prepared by melting in an electrical arc furnace with non-consumable W electrodes in an oxygen-gettered Ar atmosphere. They were cast into a horizontal mold machined in the water-cooled copper hearth. They were remelted four times and inverted during each melting operation to prevent segregation. The buttons produced were approximately

circular in cross section of 10 mm diameter and 70 mm long. The buttons were given a homogenization treatment at 1473 K for approximately 24 h in ultrapure Ar flowing in a mullite tube furnace. They were then mounted on feldspar blocks using cold setting epoxy resin and hardener and were cut into slices 1 mm thick with a diamond blade mounted on a Micro-Matic Precision Wafering Machine or with a low speed Isomet Diamond Saw (Buehler Ltd.). A Servomet Spark Cutting Machine was used to cut the alloys with high Al content since they were too brittle. The slices were trimmed on a SiC abrasive belt to give a rectangular form. A hole of 0.6 mm diameter for suspension in the furnace was drilled in each sample. To avoid mechanical damage, no mounting was used and a masking tape was used to hold the specimens during polishing through 220, 320, 400, and 600 mesh SiC abrasive papers using water as lubricant. They were then sealed in quartz tubes evacuated to 10^{-8} atm and annealed at 1173 K for 24 h to relieve stresses which may have been introduced during cutting and polishing. Following this step, a micrometer was used to measure the size of each specimen to 0.01 mm for computing its surface area. The specimen size was approximately 10 mm × 10 mm and 1 mm thick. The final polishing was done on napless cloths impregnated with 6 μm and then 1 μm diamond paste using kerosene as lubricant. After thoroughly washing with petroleum ether and ethanol, the specimens were ultrasonically agitated in distilled water using a Branson Automatic Cleaner. Then, they were washed in ethanol, dried in a stream of clean compressed air and stored in a dessicator kept under vacuum.

4.2.2 Determination of Alloy Composition and Homogeneity

Representative specimens were mounted in cold setting epoxy resin and metallographically polished to examine their microstructures. The average grain size of any composition was usually large; it varied approximately from 0.1 mm for Ni-2, 6 and 13 wt.% Al to 1 mm for Ni-32 wt.% Al alloys.

Alloy homogeneity was insured using EPMA. The actual Ni content was determined by wet chemical analysis involving double precipitation with dimethylglyoxime using tartaric acid to complex Al . A Perkin-Elmer Atomic Absorption Spectrophotometer was used to determine the Al content. The actual alloy compositions are given in Table 4-1. They were single-homogeneous phases within the EPMA sensitivity.

Table 4-1

Actual Alloy Compositions

Nominal Composition	Actual Composition wt.%Al	at.%Al
Ni- 2wt %Al	2.1	4.4
Ni- 6wt.%Al	5.9	12.0
Ni-32wt.%Al	32.2	50.8

In order to study the effect of surface preparation on the oxidation behavior, some samples were electropolished. The experimental conditions and solutions used in electropolishing and etching the alloys and oxide phases are given in Table 4-2.

Table 4-2

Procedure and Solutions used in Polishing or Ething Alloy and Oxide Phases

Phase	Purpose	Procedure	Ref.
Ni	Polishing	H_2SO_4 (60%), I = 0.6 A/cm², T = 273 K, vigorous agitation.	(46)
Ni-Al alloys	"	H_2SO_4 (ρ=1.84):CH_3OH = 1:7, E = 12.5 V, t = 2-4 min.	(151)
"	"	H_3PO_4 (85%):C_2H_5OH:H_2O = 40:38:22, I = 0.35 A/cm².	(152)
Ni-Al (γ)	Etching	Lactic Acid:HCl(ρ=1.2):HNO_3 (ρ=1.4) = 30:20:10.	(151)
Ni-Al (γ')	"	HCl(ρ=1.2):C_2H_5OH:$CuCl_2$. $2H_2O$ = 40cm³:80cm³:26g.	(151)
Ni-Al (β)	"	HCl(ρ=1.2):CrO_3 = 150cm³: 1.5 g.	(151)
NiO	"	HF:CH_3COOH:H_2O = 1:1:4, E = 3-5 V, t = 2-5min.	(46)
Al_2O_3	"	H_3PO_4(85%), T = 700 K, t = 2-3min.	(153)

4.2.3 Examination of Alloy Substructure

The substructure of β-NiAl phase was studied using Berg/Barrett X-ray topography technique which is described elsewhere[154]. These measurements have been carried out in collaboration with another research laboratory[155]. Cu-K_{α_1} radiation was used and the samples were oriented for Bragg diffraction from (111) or (100) planes. The contrast obtained in the X-ray images

can be caused by variations either in the orientation or spacing of the diffracting planes[154].

4.2.4 Specimen Preparation for Inert Marker Experiments

The method used consists of vapor depositing an extremely thin inert metallic marker,and determining its location within the reaction zone subsequent to oxidation using AES and Ion Sputtering techniques. The detectability limit of AES (10-1000 ppm) and its surface sensitivity (≈1.5 nm) allow the use of a very limited amount of the marker so that its interferance with the reaction is minimized.

Subsequent to the sample preparation procedure described in Sec.4.2.1, the specimens were further electopolished prior to vacuum vapor depositing Pd which was purchased in the form of wire from Ernest F. Fullam Inc. Three 300-mesh Cu sheet screens superimposed at 120° to each other were used as a mask to give deposits of 50 to 200 μm^2 at a fractional coverage of 0.15. The estimated thickness of the deposited marker is 3 - 5 nm. Pd was used as an inert marker because it meets the following criteria : chemical stability at oxidizing temperature, high melting point (1825 K)[156], ease of evaporation in vacuum, low vapor pressure at oxidizing temperature and high Auger electron yield[157].

Following oxidation, a Scanning Auger Spectrometer equipped with an Ar ion gun, was used to determine the concentration of film constituents and the location of the Pd marker. This procedure and experimental conditions are outlined in Sec.4.4.1.

4.3 OXIDATION APPARATUS AND PROCEDURE

Oxidation runs were carried out in flowing oxygen at 1 atm pressure in the temperature range 1273 to 1473K . The extra dry pure oxygen, which was supplied by Matheson, was purified further by passing through Ascarite, silica gel and Drierite to remove any traces of CO_2 and H_2O. The complete assembly, which consisted of an oxygen supply and purification system, a vertical mullite tube furnace with its ends sealed to pyrex tubes, a vacuum system and a balance, is shown in Fig.4-1. An Ainsworth, type RV, semi-automatic balance equipped with a Bristol, type AU-1, recording unit was used. The weight change measurement effectuated by this balance is based on the piezoelectric effect. The mechanical strains, which are exerted on a transducer due to the weight change, are converted to electrical signals which are amplified and used to operate the recorder pen. Under the experimental conditions of this investigation, the balance sensitivity was 0.1 mg. The sample was suspended to a Pt wire fixed at one end to an iron core which could be moved freely using a magnet in a vertical quartz tube connected to the balance pan with a nylon fiber. The furnace was heated with a single cylindrical Crusilite SiC heating element surrounding the reaction tube. The temperature was controlled within ± 2 K by a proportional controller (Thermo-electric, type 400) through a Pt/Pt-10 Rh thermocouple placed between the heating element and the mullite tube. The actual temperature profile in the hot zone was previously determined

ahead of 52

Figure 4.1 Schematic of reaction assembly containing RV Ainsworth continuously recording semi-automatic balance: 1-oxygen purifier containing Ascarite, silica gel and Drierite, 2-reflection mirror, 3-observation window, 4-Pirani vacuum gauge, 5-supporting ring for heating element, 6-silicone carbide heating element, 7-furnace, 8-mullite tube, 9-thermocouples, 10-Pirani gauge, 11-loading inlet, 12-soft iron core, 13-magnet, 14-outer tube, 15-suspension tube, 16-specimen, 17-suspension wire, 18-expansion bellow, 19-automatically switched weights, 20-glass bell, 21-transducer, 22-cold trap, 23-oxygen bubbler, 24-mechanical pump.

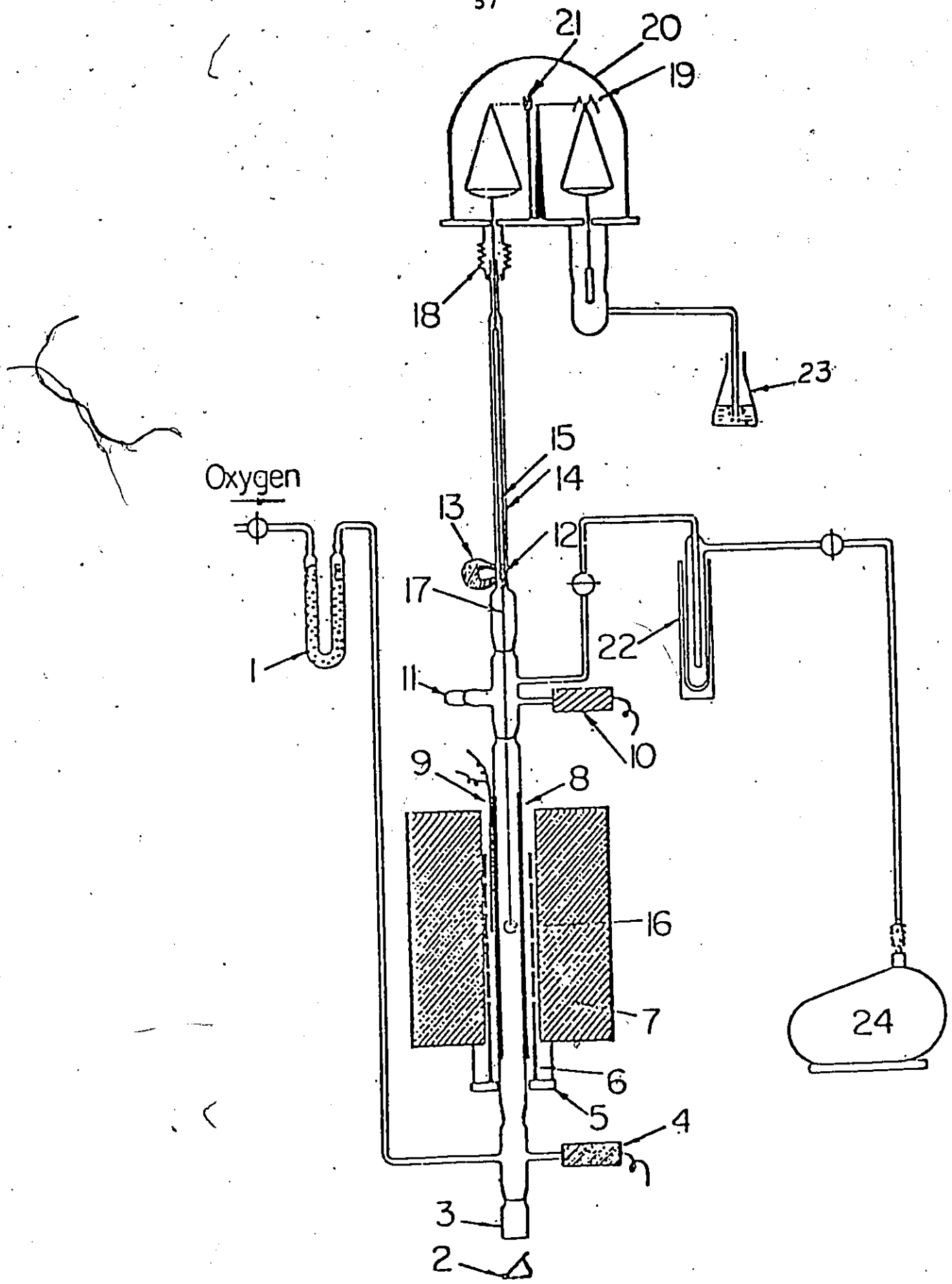
21
20
19
18
23
15
14
Oxygen
13
12
17
22
1
11
10
9
8
16
7
24
6
5
4
3
2

by calibration against a standard Pt/Pt-10 Rh thermocouple suspended in the reaction tube, using a potentiometer (Type K-3, Leeds and Northrup).

Prior to an oxidation run, the sample weight was determined using a Mettler microbalance. It was then attached to a Pt hook and suspended to the end of the Pt wire after being raised from the reaction chamber by manipulating the iron core with a magnet. The furnace was then heated to the desired temperature and evacuated to 10^{-5} atm (measured by means of a Pirani vacuum gauge) using a mechanical pump and then flushed with Ar. This procedure was repeated twice. After isolating the mechanical pump, the system was filled with oxygen at 1 atm (measured with a mercury manometer) through a metering needle valve and the gas was allowed to buble at constant flow rate in a distilled water flask connected to the other side of the balance. When the sample was oxidized to the desired extent, it was raised from the reaction zone. The weight change determined separately by weighting the sample before and after oxidation on the Mettler balance was compared with that recorded on the chart in order to determine the oxygen pick-up (usually less than 0.3 mg) during lowering the sample in the reaction chamber and during the balance time lag. The zero point and balance sensitivity were adjusted before each run.

Since the scales formed on Ni-13 and Ni-32 wt.% Al alloys spalled readily during raising the sample from the reaction zone,

a Pt basket made from a 80 mesh woven wire gauze was used to surround the samples and they were slowly cooled. However, small crystallites, with an average size of 5 to 10 μm, were found laying on the surface of the oxidized samples (Fig.4-2). Only Pt could be detected using the SEM X-ray energy dispersive analyzer. It was concluded that in the experimental conditions used, a volatile oxide of Pt(PtO_2), which is stable at high temperatures in oxygen atmosphere[156], condensed on cooling. Substitution of all Pt materials used with Pt-13 Rh alloy was found not to be effective in minimizing Pt volatilization. Moreover, since these alloys oxidized at a very slow rate, another system was used. It consisted of a Kanthal (A-1) heated mullite tube furnace closed at one end. The oxygen supply and vacuum systems were similar to those described above. Oxidation runs were carried out in static oxygen at 1 atm. The sample was suspended by a small Pt-13 Rh hook over a recrystallized Al_2O_3 boat made by cutting a cylindrical crucible parallel to its axis. Al_2O_3 thermocouple sheaths resting on groves made in the crucible walls were used to support the Pt/Rh hooks. After the evacuated furnace was brought to the desired temperature and pressure, the boat was moved from the cold part of the furnace to the hot zone by means of a quartz rod which could be manipulated back and forth in the furnace through a stainless steel swage-lock fixed at the end of the pyrex closing cover of the other end of the tube. The O-ring seal at the area of contact in the joint was effective in keeping the reaction chamber vacuum tight. The assembly is

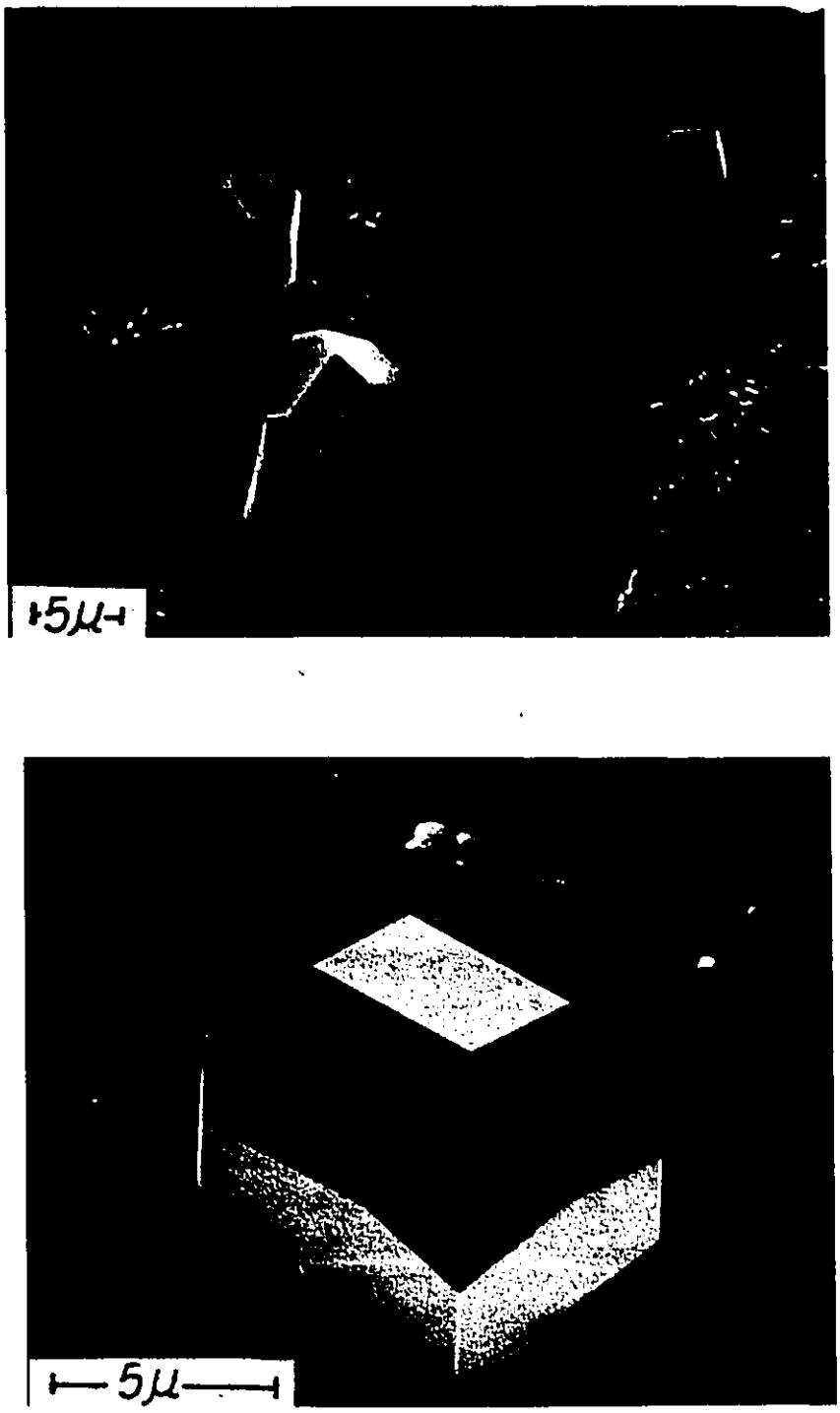

Fig.4-2. SEM images of platinum oxide crystals formed by oxidative vaporization at 1473 K in oxygen.

shown schematically in Fig.4-3. In this case, the reaction kinetics were determined by measuring oxide scale thickness using SEM.

4.4 ANALYSIS OF OXIDATION PRODUCTS

4.4.1 Films

Thin oxide films were stripped from the alloy substrate and examined with a Siemens Elmiskop I model TEM operated in the range of 80 to 100 kV. Polycrystalline oxide phases were identified using the relation

$$R \times d = \lambda \times L \qquad (4.1)$$

where R is the distance between the central spot and diffraction ring,

λ is the electron wave length,

L is the camera constant,

d is the interplanar spacing.

The diffraction patterns were indexed by comparison with a standard gold diffraction pattern obtained under the same operating conditions of the microscope.

Two methods were used to strip the oxide films. In the first method, the oxidized sample was immersed in a 10 % bromine-methanol solution which selectively dissolved the alloy. The remaining oxide film was transferred to cleaning solutions, washed, dried and sandwiched between two Cu grids. In the second, an extraction replica, prepared by spreading parlodion (cellulose acetate dissolved in iso-amyl acetate) on the surface of the oxidized sample, was used. After the plastic film has solidified, a sharp knife was used to cut

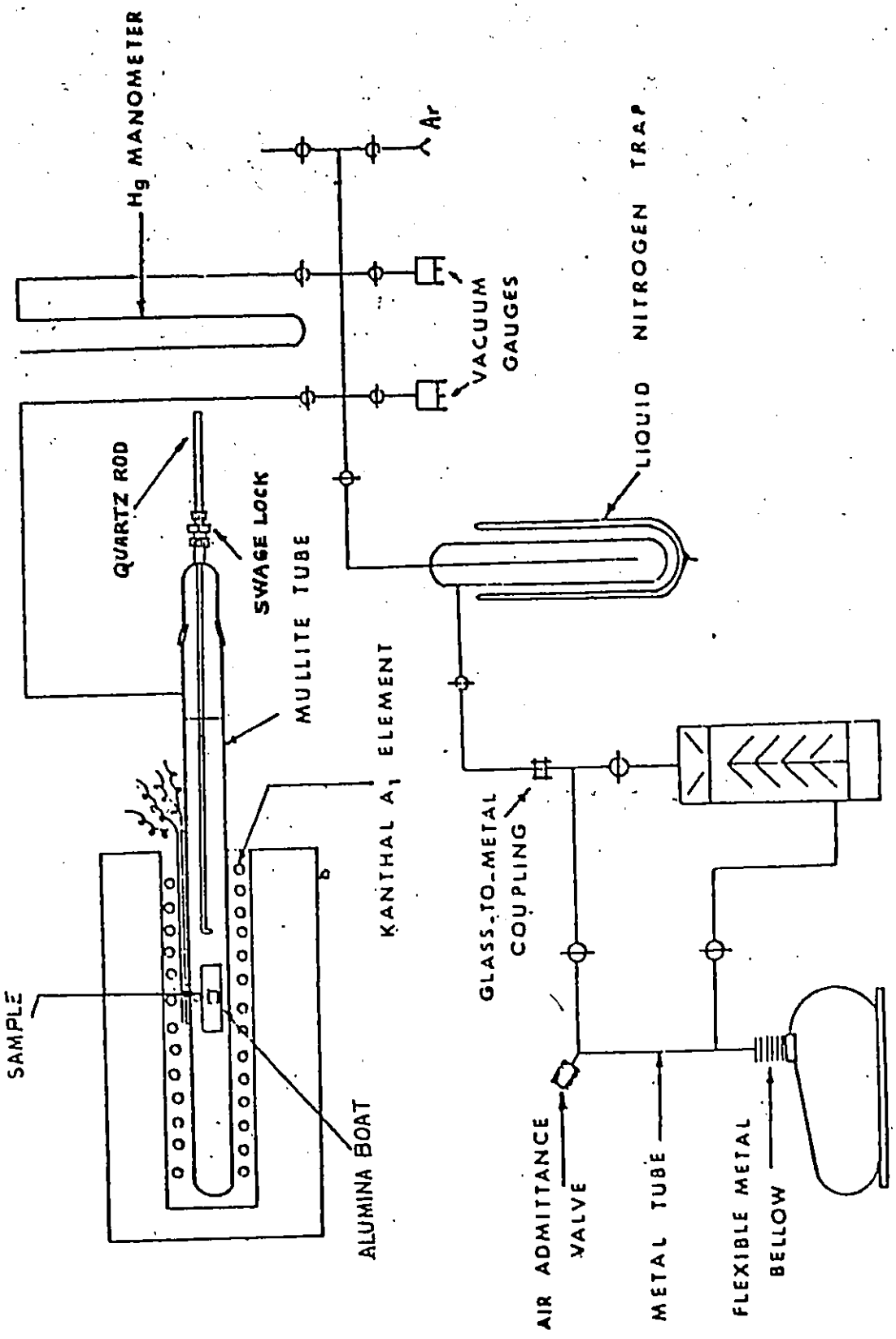

Fig.4-3: Schematic of the reaction assembly used for oxidizing alloys with high aluminum content.

it in square pieces which were transferred to Cu grids laid on a filter paper to dissolve the plastic with iso-amyl acetate. The second method was not successful in stripping tenaciously adherent oxide films.

The compositions of oxide films were determined using a Scanning Auger Spectrometer equipped with an Ar ion gun (Physical Electronics Industries Inc.,Model 544). The measurements were performed while simultaneously sputtering the oxide films. The experimental conditions for these measurements are given in Table 4-3. Corrected Auger peak intensities were used to represent the concentrations of the film constituents. The atomic fraction of each element is given by[157]:

$$N_i = \frac{I_i/c_i}{\Sigma\, I_i/c_i} \qquad (4.2)$$

where I_i are the Auger peak-to-peak intensities,

c_i are experimental relative sensitivity correction factors.

No corrections were applied to account for preferential sputtering.

Table 4-3
Experimental Conditions Used in AES Measurements.

	Electron Beam	Ar Ion Beam
Acceleration Voltage (kV)	4	5
Current	2 μA	20 mA
Diameter (μm)	3	-
Scanned or Rasted Area	60μm×100μm	4mm×4mm
Residual Pressure (atm)	10^{-13}(no sp.); 10^{-7}(while sp.)	

4.4.2 Scales

Oxide phases were identified by X-ray Debye and Scherrer Powder Diffraction technique using Ni-filtered Cu-K_α radiation and by RHEED in the case of thick films.

A Zeiss optical microscope and a Cambridge SEM were used to study the morphology of the reaction products. Vacuum impregnation with epoxy resin was necessary to improve sample edge retention during polishing. Cold mounting epoxy and hardener were used to mount the samples and the standard polishing and etching procedures were followed. Since it was necessary to use hot H_3PO_4 (673 K) to etch Al_2O_3 scales which would attack the mounting material, another sample preparation procedure[158] was used in this case. The spalled Al_2O_3 flakes were mounted using molten Parowax. After the wax solidified, the samples were carefully polished using 600 mesh SiC papers and kerosene as lubricant. The wax was then dissolved in chloroform and the flakes were transferred to cleaning and etching solutions and finally cleaned in methanol. Whenever etching was difficult, fracture cross sections were obtained and examined with the SEM. An X-ray energy dispersive analyzer attached to the SEM permitted the identification of the oxide phases.

A Cameca MS-64 EPMA, which was operated at 15 kV and 50 nA filament current, was used to determine the compositions of the reaction products. Line scan and point count methods were used. In the latter case, alloy compositions were determined by calibration using standards and oxide compositions from the measured X-ray intensities after applying the neces-

sary corrections for atomic number, absorption and fluorescence using a computer program developed in this laboratory[159] based on a McMaster publication[160]. It was necessary to coat the samples with C by vapor deposition to avoid electrical charge build-up while examining the samples in the SEM and EPMA.

CHAPTER 5

EXPERIMENTAL RESULTS

5.1 INTRODUCTION

The results can be conveniently divided into three sections according to the microstructure of Al_2O_3* formed on the alloys. Al_2O_3 is precipitated internally in alloys which contain < 4 wt.%Al. The oxidation results of the Ni-2 wt.% Al alloy, which exhibit this behavior, are included in Sec.5.2. An imperfect Al_2O_3 scale is formed on alloys with intermediate Al compositions (5 ∿ 7 wt.%). Alloys in this class undergo a long transient period before reaching a final oxidation stage wherein the scale exhibits a steady state morphology. The oxidation results of Ni-6 wt.% Al alloy, which fall in this latter classification, are presented in Sec.5.3. Only Al_2O_3 is formed on alloys with compositions > 19 wt.% Al and it grows as a continuous film from the onset of the reaction. The growth of the protective Al_2O_3 scale on Ni-32 wt.% Al alloy is investigated in Sec.5.4.

5.2 INTERNAL PRECIPITATION OF Al_2O_3 AND DUPLEX SCALE FORMATION

5.2.1 Oxidation Kinetics

Ni-2 wt.% Al alloys were oxidized in flowing oxygen at one atmosphere pressure in the temperature range 1273-1473 K. The reaction rates were determined thermo-gravimetrically

---

* Except where specifically indicated, Al_2O_3 will be used in the text to designate α-Al_2O_3.

using a continuous recording semi-automatic Ainsworth balance. They follow a parabolic relation in the temperature range and over the time period investigated (up to 50 h). The values of the parabolic rate constants are given in Table 5-1. The rate constants for oxidation of pure Ni are also included for comparison. The rate constants for Ni-2 wt.% Al alloys are approximately one order of magnitude greater than those for pure Ni at the same temperatures. An Arrhenius plot of these results is shown in Fig.5-1. The activation energy for the oxidation of Ni-2 wt.% Al alloy is 146 kJ/g mole ; while its value for the oxidation of Ni is 193 kJ/g mole.

Table 5-1

Parabolic Rate Constants for Oxidation of Ni and Ni-2 wt.% Al Alloys.

T (K)	k ($g^2.cm^{-4}.sec^{-1}$) Ni	Ni-2 wt.% Al
1273	1.0×10^{-10}	1.4×10^{-9}
1373	3.6×10^{-10}	3.9×10^{-9}
1473	1.2×10^{-9}	9.2×10^{-9}

5.2.2 Scale Morphology

Oxidation of Ni-2 wt.% Al alloys results in the formation of a duplex external scale and an internal precipitation zone in the alloy. The outer oxide layer is dark gray and the inner is light green. It was possible to fracture the scale

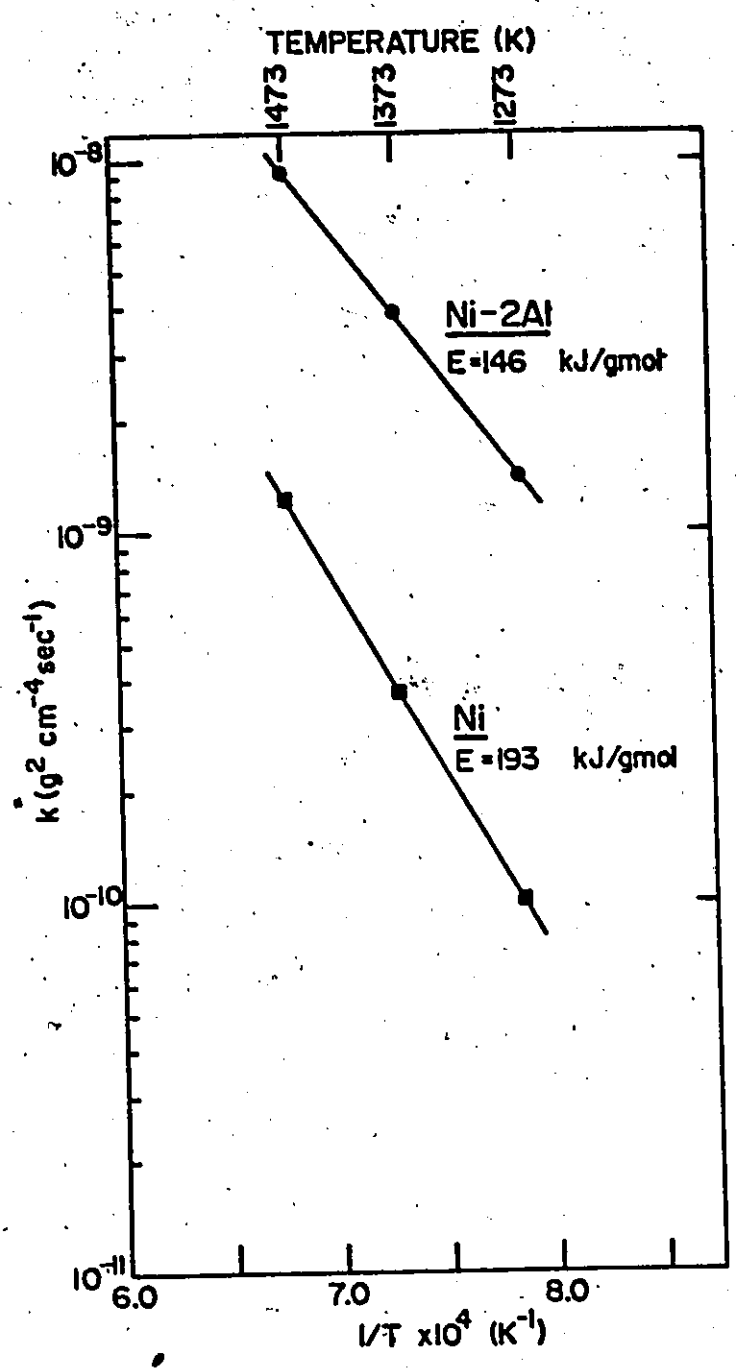

Fig.5-1. Arrhenius plot of the parabolic rate constants for Ni and Ni-2 wt.% Al oxidation.

along the interface between the two layers and make a separate X-ray powder diffraction analysis of each layer. The internal precipitates, which were extracted by dissolving the alloy in 10 % bromine- methanol solution, were also subjected to X-ray diffraction analysis. These analyses are given in Table 5-2. The standard X-ray diffraction data for oxides which can form on Ni-Al alloys are included in Table 5-3 for reference. According to these measurements, the outer layer is NiO, the inner layer is mainly NiO containing $NiAl_2O_4$ as a second phase and the internal precipitates are Al_2O_3.

The different regions of the scale are shown in Fig.5-2 {(a)-(g)}. Fig.(a) is an over-all cross section showing the duplex scale and part of the internal precipitation zone. Fig.(b) is a fracture cross section of the outer layer which has a coarse grained columnar structure. Well defined pores exist in the vicinity of its interface with the inner layer. The pore size is in the range of 1 $\sim$ 5 μm. The outer surface of the scale adjacent to the gas phase has a terraced structure and an average grain size of 30 μm, Fig.(c). The structure of the inner oxide layer was revealed by mechanical polishing, Fig.(d). It consists of rod-shaped precipitates, presumably $NiAl_2O_4$, which are embedded in a NiO matrix partially pulled out by polishing. The precipitates lay parallel to the scale growth direction and extend between the inner/outer layers interface and the inner layer/ alloy precipitation zone interface. This latter interface is shown in Fig.(e). The

Table 5-2
Results of X-ray Analysis
(Interplanar Spacings nm×10)

Ni-2 wt.% Al (6 h at 1473K) outer layer		Ni-2 wt.% Al (6 h at 1473K) inner layer		Ni-2 wt.% Al (6 h at 1473K) internal prec.		Ni-32 wt.% Al (7 d at 1473K)	
2.4 *	N	4.63	S	3.48*	A	3.48 *	A
2.08 *	N	2.84	S	2.55*	A	2.55 *	A
1.473*	N	2.4 *	N	2.38	A	2.37	A
1.258	N	2.08 *	N	2.08*	A	2.08 *	A
1.205	N	2.01	S	1.74	A	1.74	A
1.043	N	1.55	S	1.6 *	A	1.6 *	A
0.958	N	1.476*	N			1.407	A
0.932	N	1.423	S			1.375	A
0.853	N	1.26	N			1.24	A
0.804	N	1.207	N			1.043	A
		1.043	N				
		0.958	N				
		0.933	N				
		0.856	N				

Table 5-3
X-ray Diffraction Data for Possible Oxides Formed on Ni-Al alloys

γ-Al_2O_3 d nm×10	(hkl)	α-Al_2O_3 d nm×10	(hkl)	NiO d nm×10	(hkl)	$NiAl_2O_4$ d nm×10	(hkl)
4.56 *	(111)	3.47	(102)	2.410*	(111)	4.65 *	(111)
2.80	(220)	2.55	(104)	2.088*	(200)	2.846	(220)
2.39 *	(311)	2.375	(110)	1.476*	(220)	2.427*	(311)
2.28	(222)	2.160	(006)	1.259	(311)	2.013*	(400)
1.977*	(400)	2.083*	(113)	1.206	(222)	1.6415	(422)
1.520	(511)	1.96	(202)	1.0441	(400)	1.5485	(511)
1.395*	(440)	1.736	(204)	0.9582	(331)	1.4232*	(440)
1.140	(444)	1.598*	(116)	0.9338	(420)	1.3601	(531)
1.027	(731)	1.545	(121)	0.8527	(422)	1.2739	(620)
0.989	(800)	1.508	(108)	0.8040	(511)	1.2274	(533)
0.884	(840)	1.401	(214)			1.2134	(622)
0.806	(844)	1.371*	(300)			1.1613	(444)
		1.237	(101)			1.0753	(642)
		1.041	(226)			1.0476	(731)

* = main lines, N = NiO, S = $NiAl_2O_4$ spinel, A = α-Al_2O_3.

precipitates in the two zones extend along it. The morphology of the Al_2O_3 precipitates was not completely revealed by mechanical polishing, Fig.(e), or chemical etching, Fig.(f). However, a better relief was obtained by " deep etching ", Fig.(g). The Al_2O_3 precipitates, which have a rod-like structure, extend across the precipitation zone parallel to the growth direction . Fig.5.3{(a)-(d)} are SEM images further illustrating the structural properties of the internal precipitates. Their population and size are uniform through the precipitation zone, Fig.(a), except at alloy grain boundaries where they are usually denser without forming a continuous layer, Fig.(b). However, it was observed that these parameters depend on temperature, alloy composition and would probably depend on the oxygen partial pressure. The precipitates, which are formed at 1473, Fig.(c), are coarser and have a wider spacing than at 1273 K, Fig.(a). At 1473 K, the average precipitate size and spacing are 3 and 10 μm, respectively, which correspond to a fractional coverage of 0.07. The cylindrical rod shape of the precipitates was further ascertained by examining a transverse deep-etched section, Fig.(c). It was not possible to establish if a boundary exists at the precipitation front, Fig.(d).

Ni and Al X-ray scans across the scale and the internal precipitation zone are shown in Fig.5-4. The alloy in the vicinity of the precipitation front is depleted of Al. It was not possible to precisely determine the amount of Ni dissolved

ahead of 72

Fig.5-2

Ni-2 wt.% Al alloy scale structure (SEM images; 1473 K except (g), 1273 K)

(a) Global cross section
(b) Outer NiO layer
(c) Outer scale surface
(d) Inner NiO-$NiAl_2O_4$ Layer
(e) Interface between inner layer and internal precipitation zone
(f) Internal precipitation zone (alloy + Al_2O_3)
(g) Internal precipitation zone, deeply etched.

Fig.5-3

Details of the Al_2O_3 precipitation zone (SEM images; (a) and (b) 1273 K, (c) and (d) 1473 K).

(a) Deep-etched longitudinal section
(b) Precipitation at grain boundaries
(c) Deep-etched transverse section
(d) Alloy precipitation front (Etched)

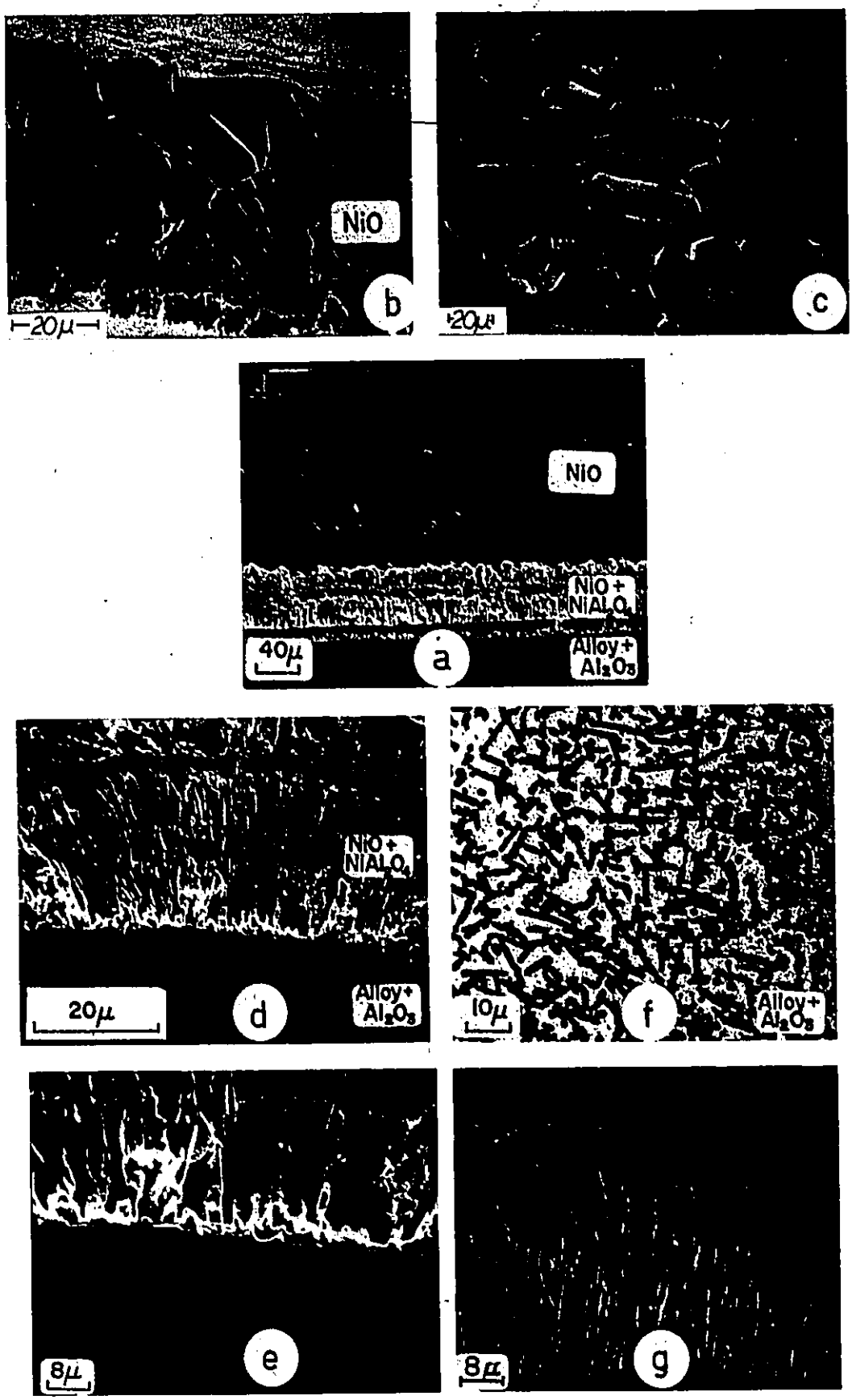
NiO
b
20μ
20μ
c
NiO
NiO + NiAl2O4
40μ
a
Alloy + Al2O3
NiO + NiAl2O4
20μ
d
Alloy + Al2O3
10μ
f
Alloy + Al2O3
8μ
e
8μ
g

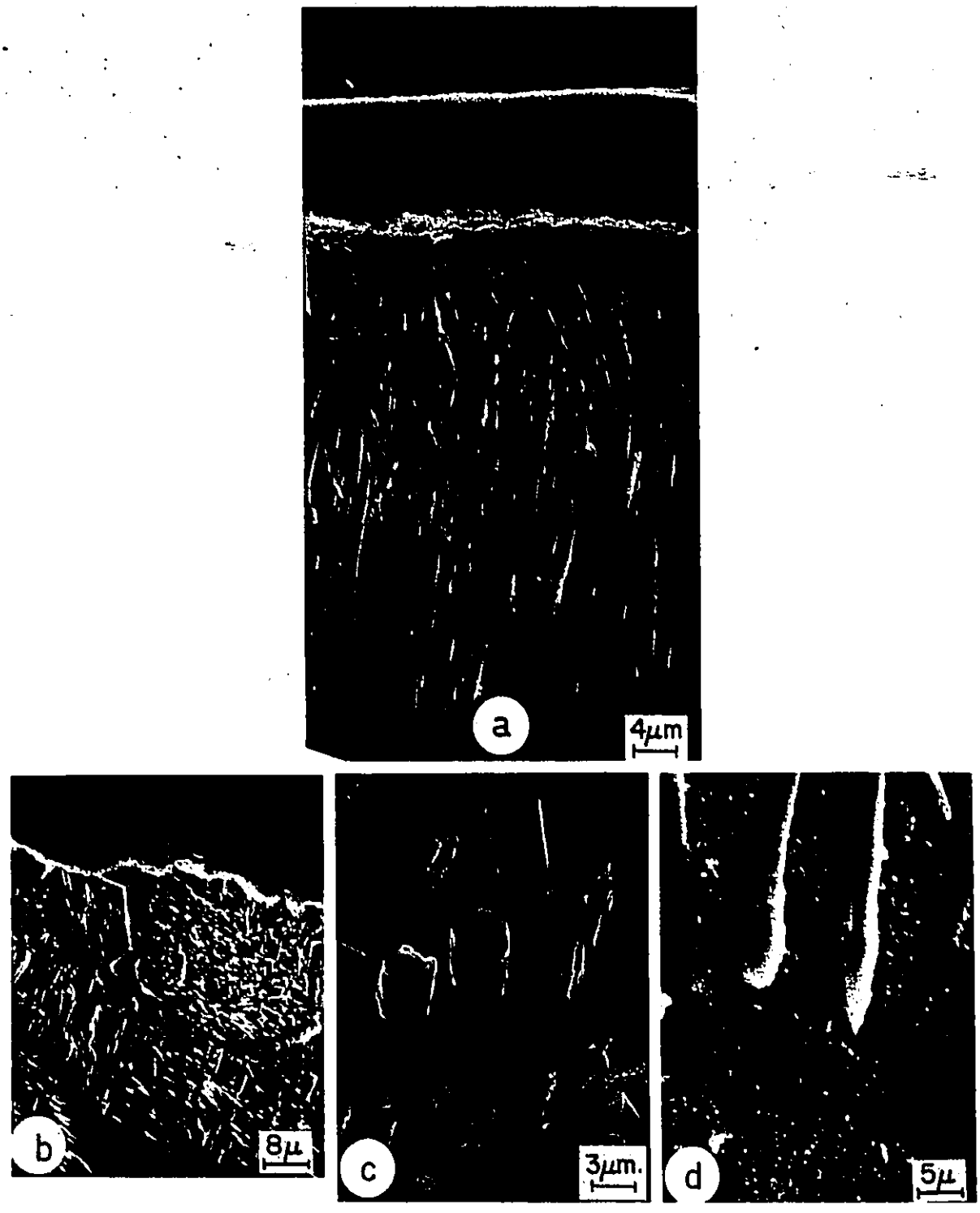
a
4μm
b
8μ
c
3μm.
d
5μ

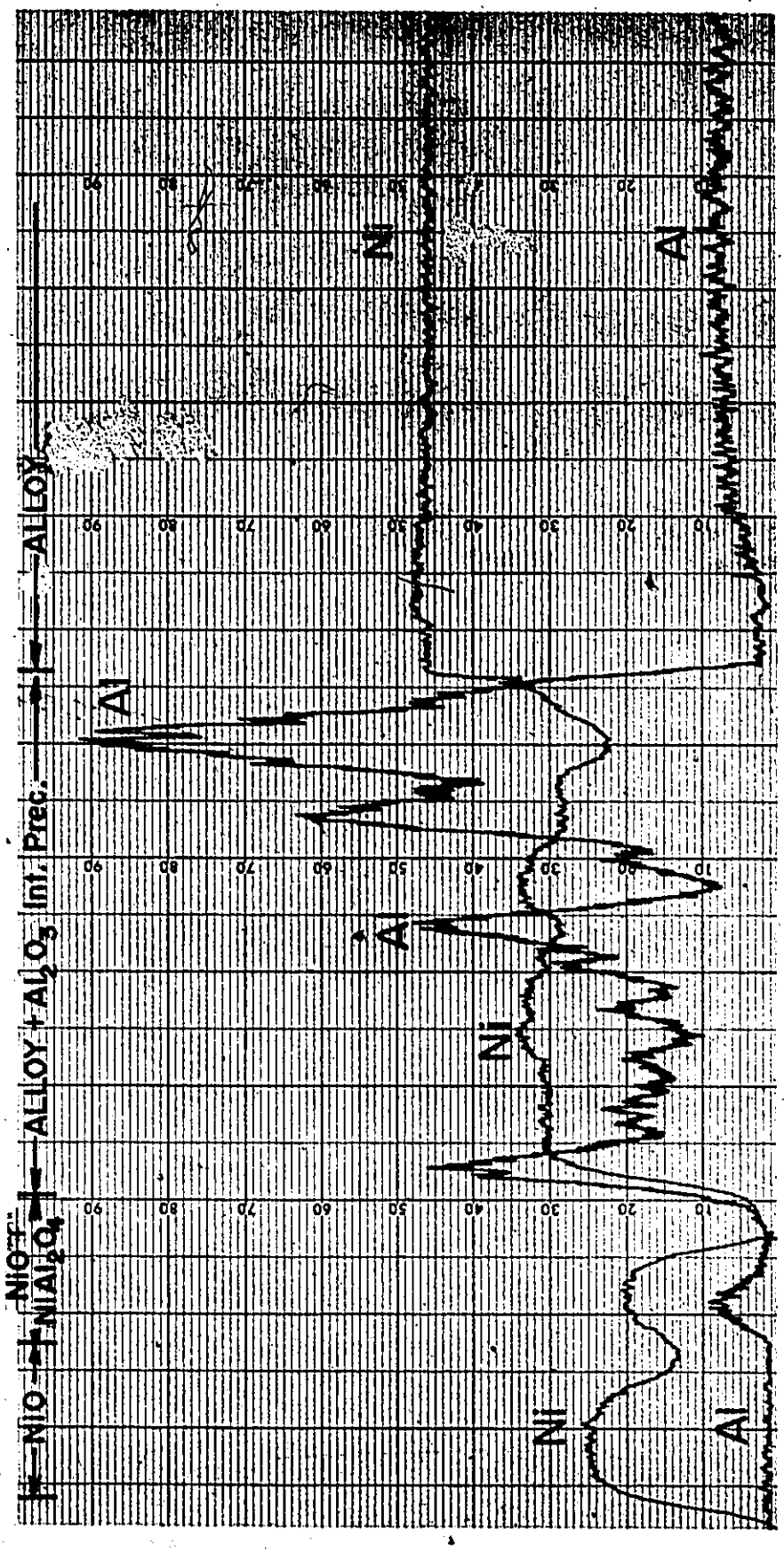

Fig.5.4. Al and Ni electron microprobe scans across a scale formed on Ni-2 wt.% Al alloy.

in the Al_2O_3 precipitates or the composition of the $NiAl_2O_4$ particles because their size is smaller than the electron microprobe diameter. The outer NiO layer is doped with Al. However, the Al X-ray counts were only sligthtly above the background level and a quantitative determination of the amount of Al dissolved in NiO was not possible.

5.2.3 Layer Thickness Measurements

Since the scale grew uniformly on the Ni-2 wt.% Al alloy, it was possible to determine the thickening rate of both oxide layers and the penetration depth of the internal precipitation zone. The latter was measured by examining etched cross sections in a light microscope while SEM was used in the other cases. The boundary between the two oxide layers could be accurately located by following Al X-ray counts using an energy dispersive analyzer attached to the SEM. All layers thickened according to a parabolic relation. The internal precipitation zone grew most rapidly and the inner two-phase layer (NiO + $NiAl_2O_4$) thickened most slowly. The values of the growth rate constants are given in Table 5-4 and the parabolic plots are shown in Fig.5-5.

Table 5-4
Parabolic Rate Constants for Layer Growth on Ni-2wt.%Al Alloy.

T (K)	k ($\mu m/h^{\frac{1}{2}}$)		
	Outer Layer	Inner Layer	Precipitation Zone
1273	3.8	1.4	19.8
1373	10.8	4.1	37.8
1473	22.2	11.4	49.8

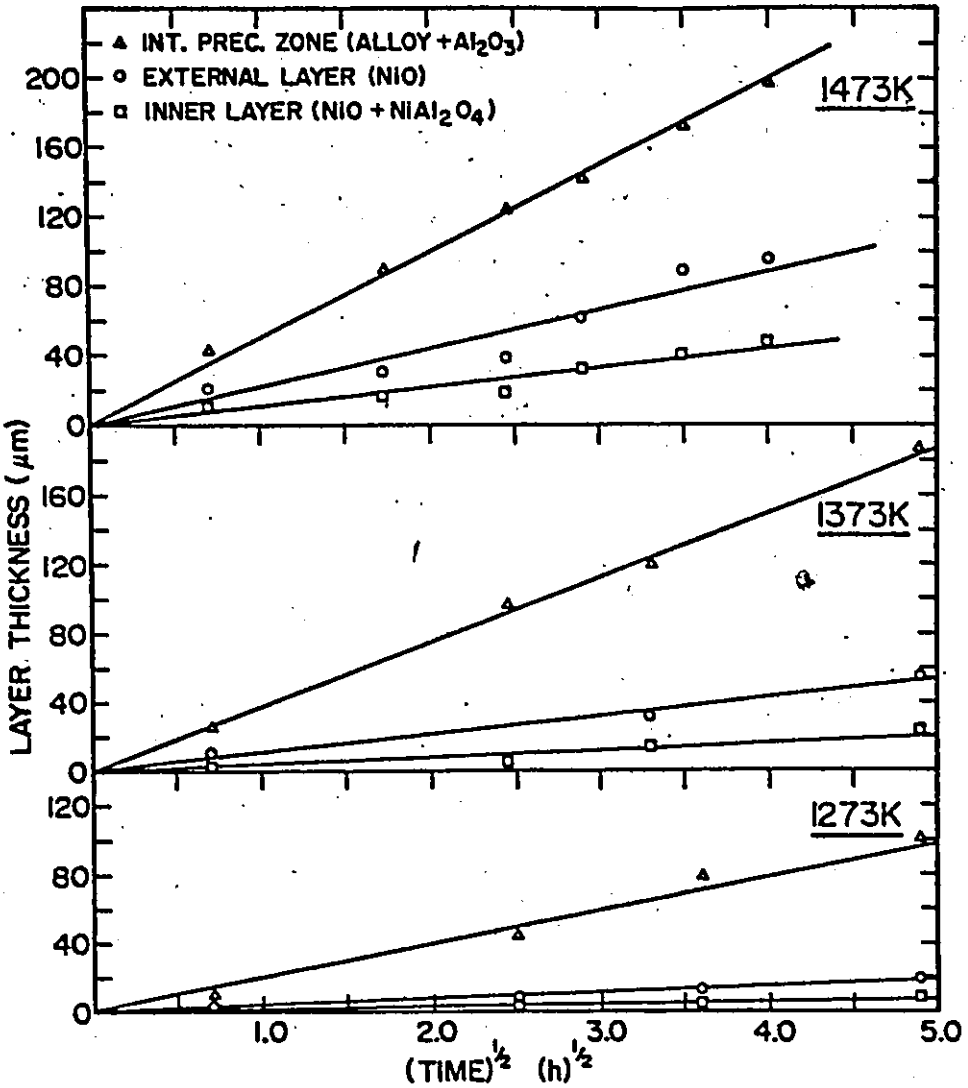

Fig. 5-5. Parabolic plots of layer growth on Ni-2 wt.% Al alloy.

5.3 TRANSITION FROM INTERNAL PRECIPITATION TO CONTINUOUS SCALE FORMATION

5.3.1 Scale Morphological Development

The scale formed on the Ni-6 wt.% Al alloy consists of a thin Al_2O_3 film through which scattered nodules protrude outward to the surface, Fig.5-6 {(a)-(e)}. The nodules tend to form preferentially at alloy grain boundaries, Fig.(a) and (b) and at alloy surface imperfections induced by mechanical polishing. Their density depends on alloy surface preparation techniques. In the region of a nodule, the scale has the same morphology observed on the Ni-2 wt.% Al alloy; namely, an outer coarse grained NiO layer having a terraced surface structure, an inner layer consisting of NiO + $NiAl_2O_4$ and an internal Al_2O_3 precipitation zone, Fig.(a)-(d). However, a continuous Al_2O_3 film is formed at the internal precipitation front at a latter growth stage, Fig.(b) and (d). Lateral growth of the nodules results in their overlap, Fig.(e), and the formation of large patches of NiO.

This alloy undergoes a long transient stage during which the initially formed internal precipitates transform to a continuous $NiAl_2O_4$ layer overlaying an Al_2O_3 film. Fig.5-7 {(a)-(d)} are light micrographs to illustrate the oxidation behavior during this transient stage. SEM images taken from large areas of the samples are shown in Fig.5-8 {(a)-(c)}. Initially, the scale has a similar structure to that observed on Ni-2 wt.% Al alloy. However, discontinuous Al_2O_3 films are

77(a)

Fig.5-6

Nodular growth on Ni-6 wt.% Al alloy
(SEM images, 1373 K)

(a) NiO nodules protruding from an imperfect Al_2O_3 film at alloy grain boundaries
(b) Nodule outer surface
(c) Scale cross section in the vicinity of a nodule
(d) Structure of the ragion beneath a nodule (deep-etched cross section)
(e) Nodules coalescence.

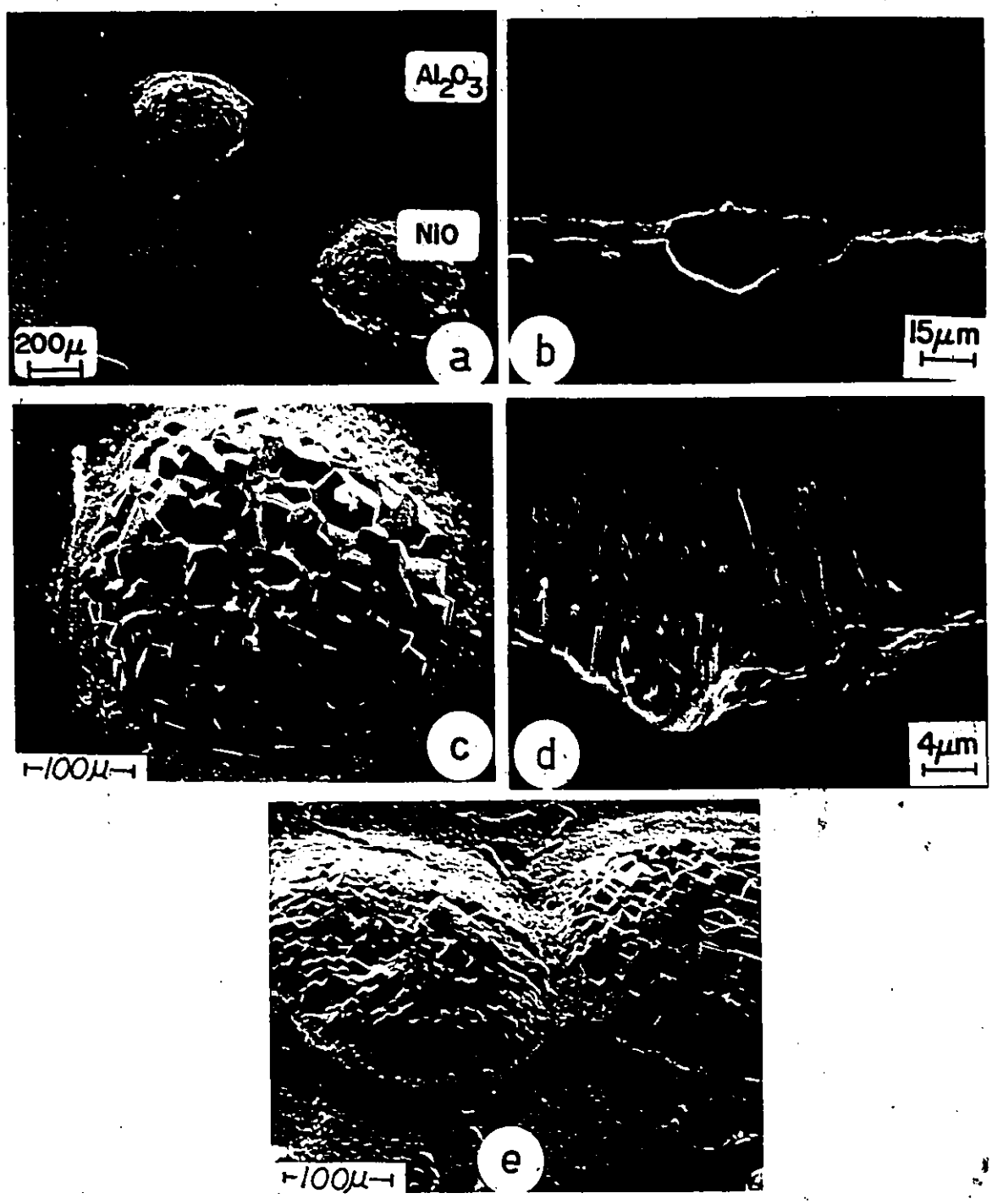
Al_2O_3
NiO
200μ
a
b
15μm
c
100μ
d
4μm
e
100μ

formed at some regions of the internal precipitation front and effectively block its advance there, Fig.5-7 (a) and 5-8 (a). Eventually, lateral growth of the discontinuous Al_2O_3 films results in the formation of a highly irregular alloy/scale interface and undercutting of the internal precipitation zone from the alloy substrate, Fig.5-7 (b) and 5-8 (b). Subsequent oxidation of the Al-depleted alloy matrix in the precipitation zone results in its conversion to NiO + $NiAl_2O_4$, Fig.5-7 (c) and (d). After a long period, a continuous $NiAl_2O_4$ layer is developed while the Al_2O_3 film beneath it continues to thicken, Fig.5-8 (c). The final steady state morphology of the scale is shown in Fig.5-9 {(a)-(c)}. Al and Ni X-ray maps indicate that it consists of an external $NiAl_2O_4$ layer overlaying an Al_2O_3 film.

5.3.2 Oxidation Kinetics

The oxidation kinetics of the Ni-6 wt. % Al alloy were also determined thermo-gravimetrically using the Ainsworth balance. The results are shown in Fig.5-10 (a) as linear plots. The kinetics are irreproducible due to the phenomenon of nodular growth. Furthermore, the amount of oxygen uptake during the initial reaction period is dependent on alloy surface preparation techniques. Specimens, which were polished down to 1 μm diamond paste, exhibit lower oxygen uptake and form fewer nodules than samples abraded on coarse SiC papers. In this latter case, NiO is formed as an almost continous external scale rather than scattered nodules.

Fig.5-7

Ni-6 wt.% Al alloy transient oxidation stages (Light microscope images, 1473 K)

(a) Al_2O_3 internal precipitation and development of a discontinuous film
(b) Al_2O_3 continuous film formation
(c) and (d) Conversion of the alloy precipitation zone to NiO + $NiAl_2O_4$

Fig.5-8

Ni-6 wt.% Al alloy transient oxidation stages (SEM images of deep-etched cross sections, 1373 K)

(a) as 5-7(a)
(b) as 5-7(b)
(c) Triplex layer morphology

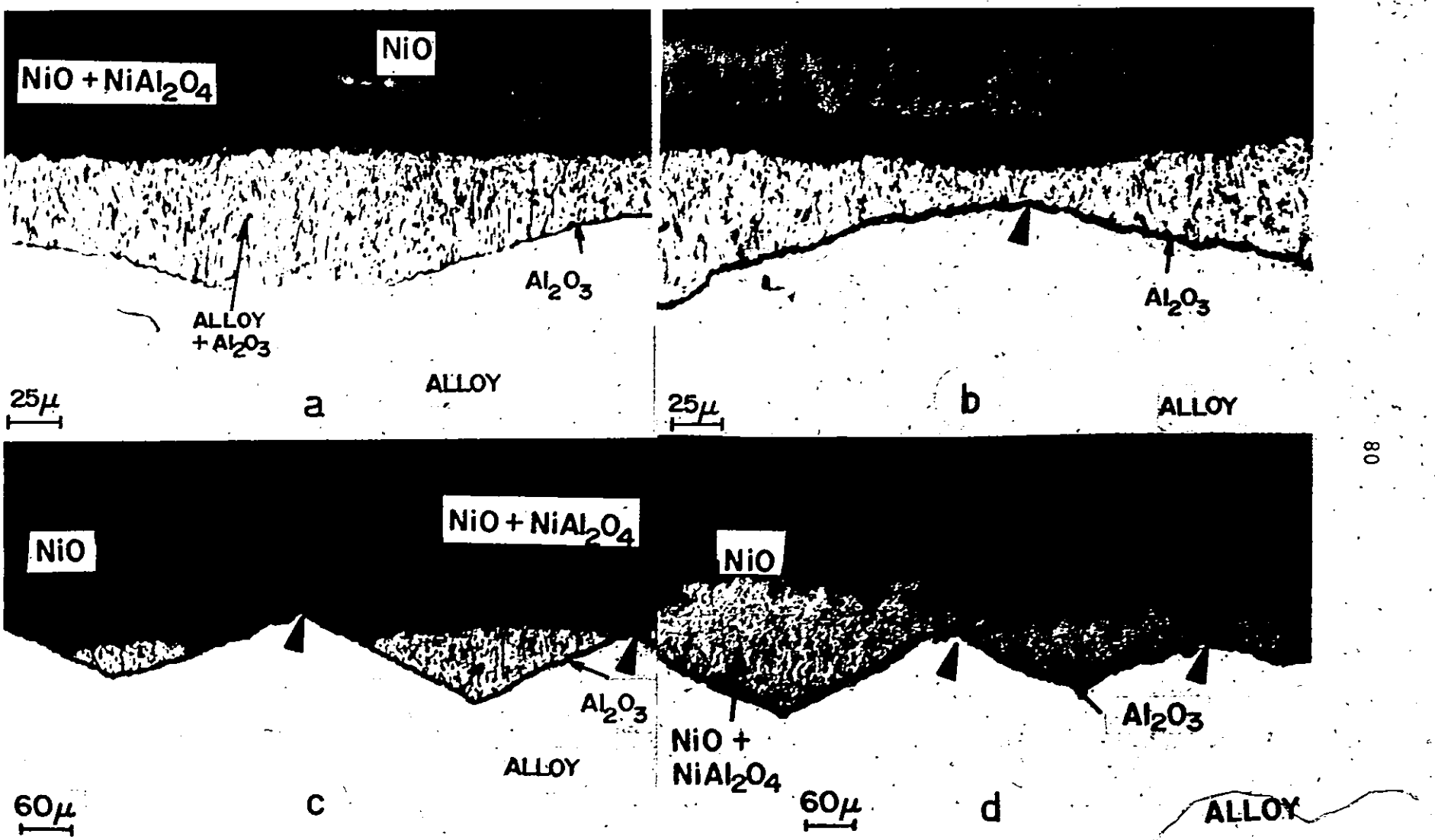
NiO + NiAl2O4
NiO
Al2O3
ALLOY + Al2O3
ALLOY
25μ
a
b
NiO
NiO + NiAl2O4
NiO + NiAl2O4
60μ
c
d

Fig.5-7

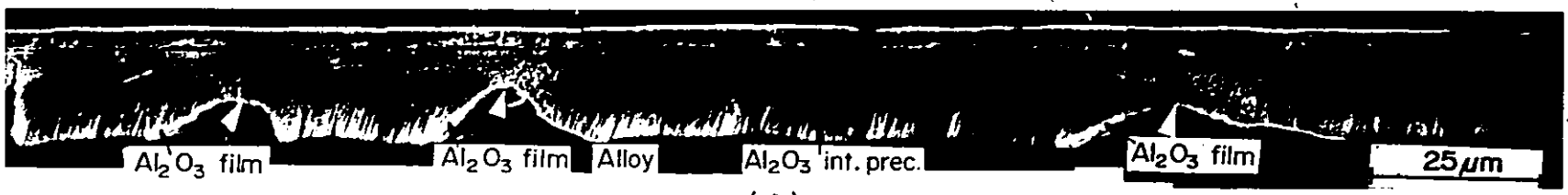
Al_2O_3 film
Al_2O_3 film
Alloy
Al_2O_3 int. prec.
Al_2O_3 film
25μm

(A)

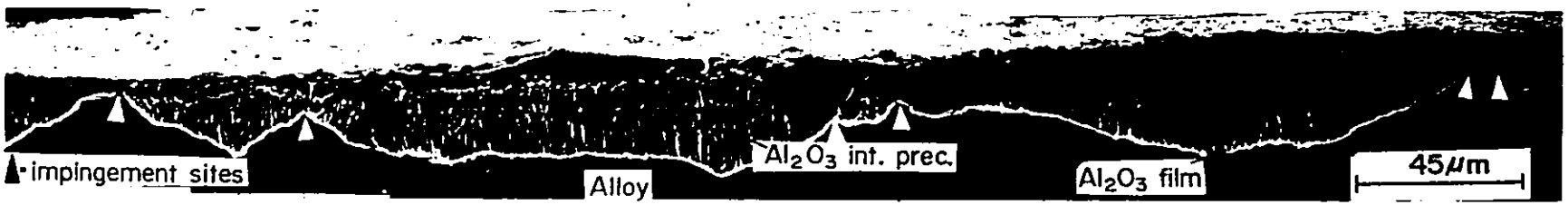
impingement sites
Alloy
Al_2O_3 int. prec.
Al_2O_3 film
45μm

(B)

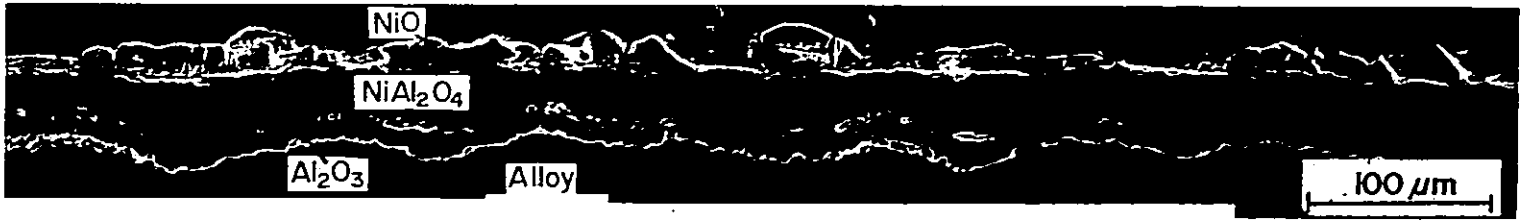
NiO
$NiAl_2O_4$
Al_2O_3
Alloy
100 μm

(C)

Fig.5-8

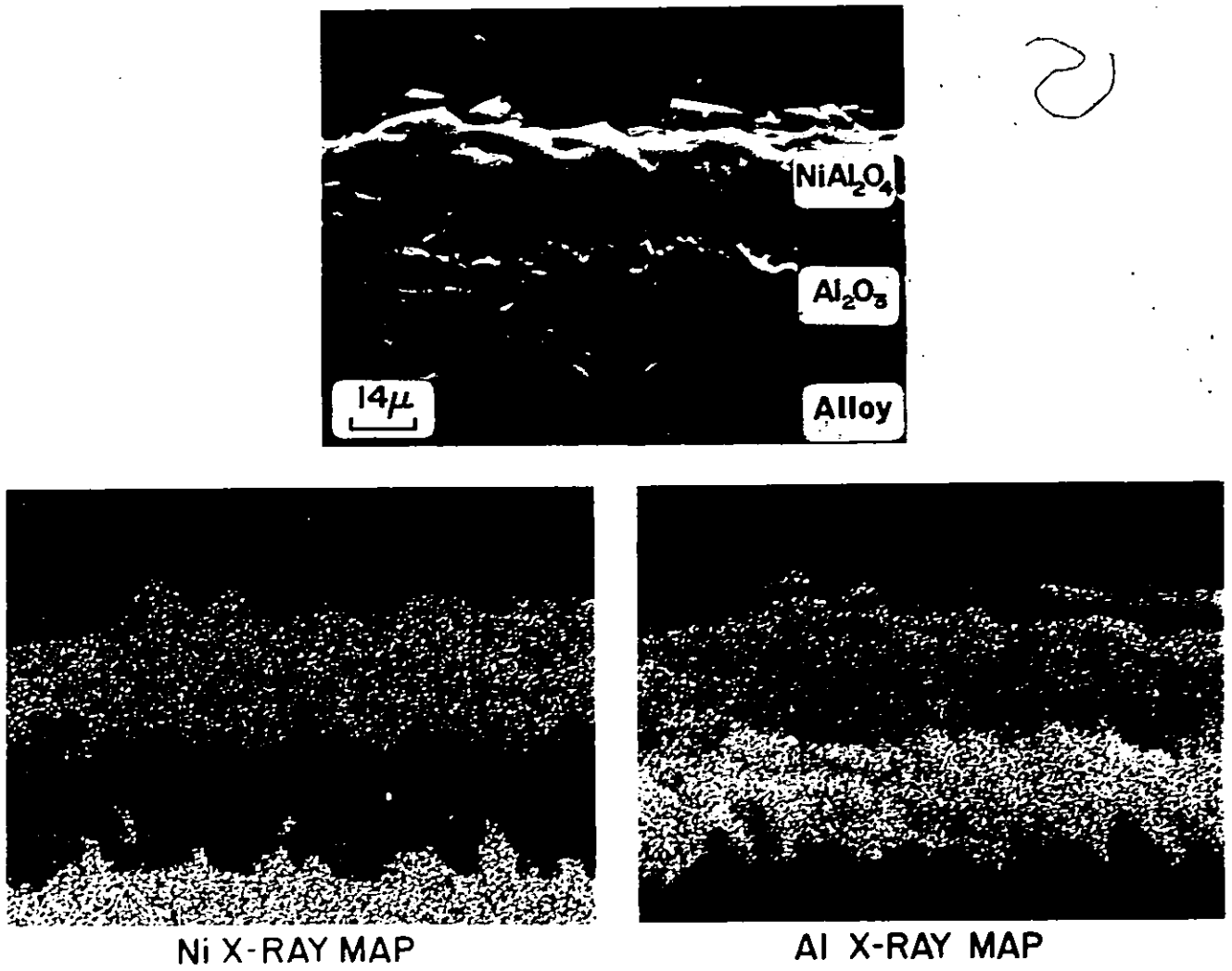

Fig.5.9. Ni-6 wt.% Al steady state scale morphology (1573K); Ni and Al X-ray maps.

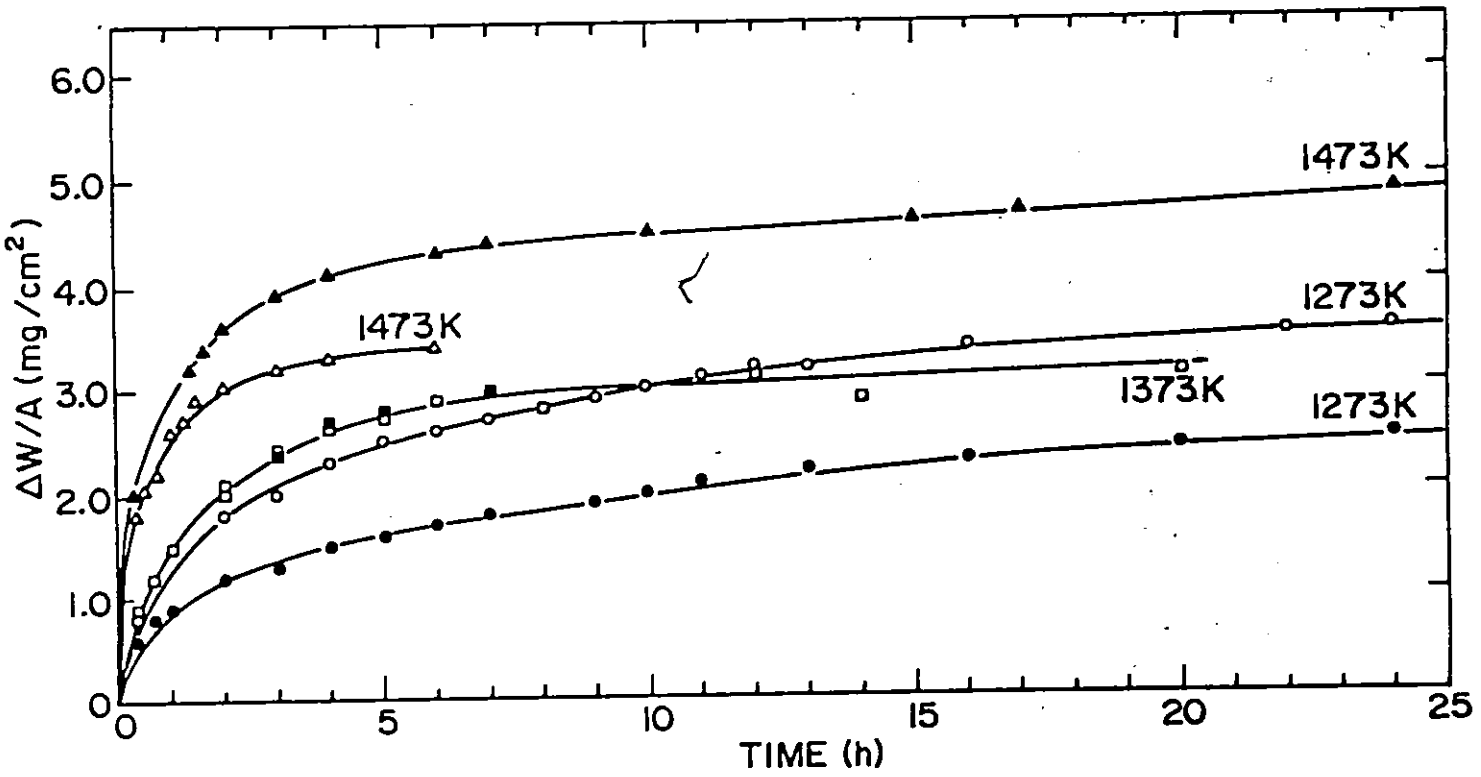

Fig.5-10(a). Ni-6 wt.% Al oxidation kinetics : linear plot.

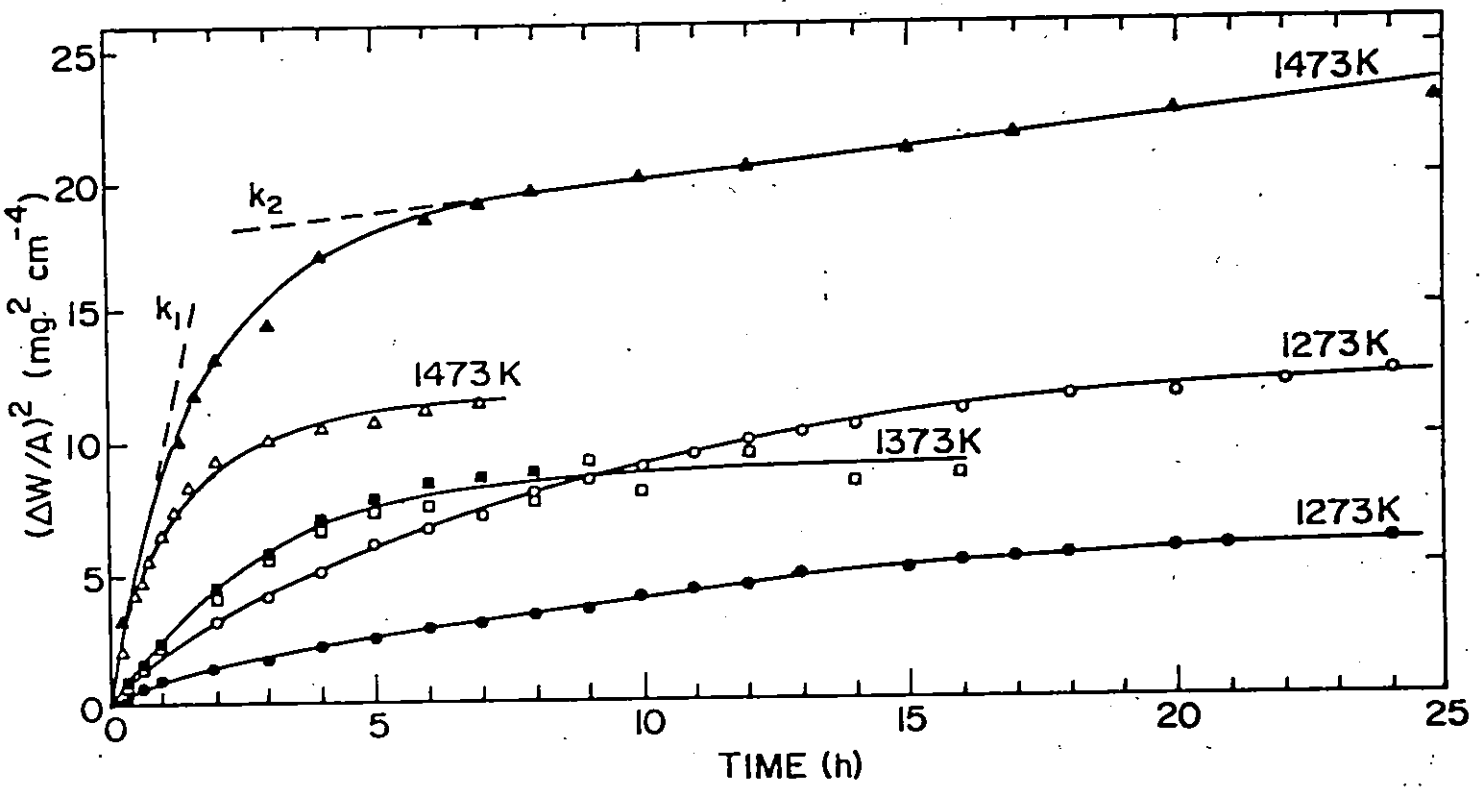

Fig.5-10(b). Ni-6 wt.% Al oxidation kinetics : parabolic plot.

Though the kinetics are irreproducible, they exhibit the same trend if presented as parabolic plots, Fig.5-10 (b), namely : an initial fast parabolic stage, subsequent to which the kinetics decline and deviate from parabolic behavior and finally, parabolic kinetics are resumed but at much slower rates. The balance sensitivity (0.1 mg) did not allow accurate measurements beyond this stage since the specimens oxidized at extremely slow rates. At T = 1473 K, the average value of the rate constant during the first parabolic stage, k_1 = 2.5×10^{-9} $g^2.cm^{-4}.sec^{-1}$, has the same order of magnitude as in the case of Ni-2 wt.% Al alloy (Table 5-1). Its value during the second parabolic stage, k_2 = 0.8×10^{-10} $g^2.cm^{-4}.sec^{-1}$, is one order of magnitude less than k_1.

5.4 GROWTH OF THE CONTINUOUS Al_2O_3 SCALE

5.4.1 Scale Morphological Development

Ni-32 wt.% Al alloys were oxidized in static oxygen at one atmosphere in the temperature range 1273-1573 K. Fig.5-11 (a) is a transmission electron image and corresponding diffraction pattern of an oxide film formed on this alloy composition at 1273 in 5 min. The estimated film thickness is 120 nm. The image exhibits poor contrast due to the lack of morphological features in the film and the pattern consists of halos which can arise either from amorphous oxide or submicrocrystallites < 10 nm in size. Heating the stripped film " in situ " to 1073 K leads to the formation of crystallites having a wide size range,50 to 250 nm, as shown in Fig.5-11 (b). This structure gives rise to a definite electron diffraction

Fig.5-11

TEM images and selected area diffraction patterns of oxide films on Ni-32 wt.% Al alloy.

(a) Initial sub-microcrystalline film (5 min at 1273 K)
(b) Film shown in (a) after heating "in situ" to 1073 K.

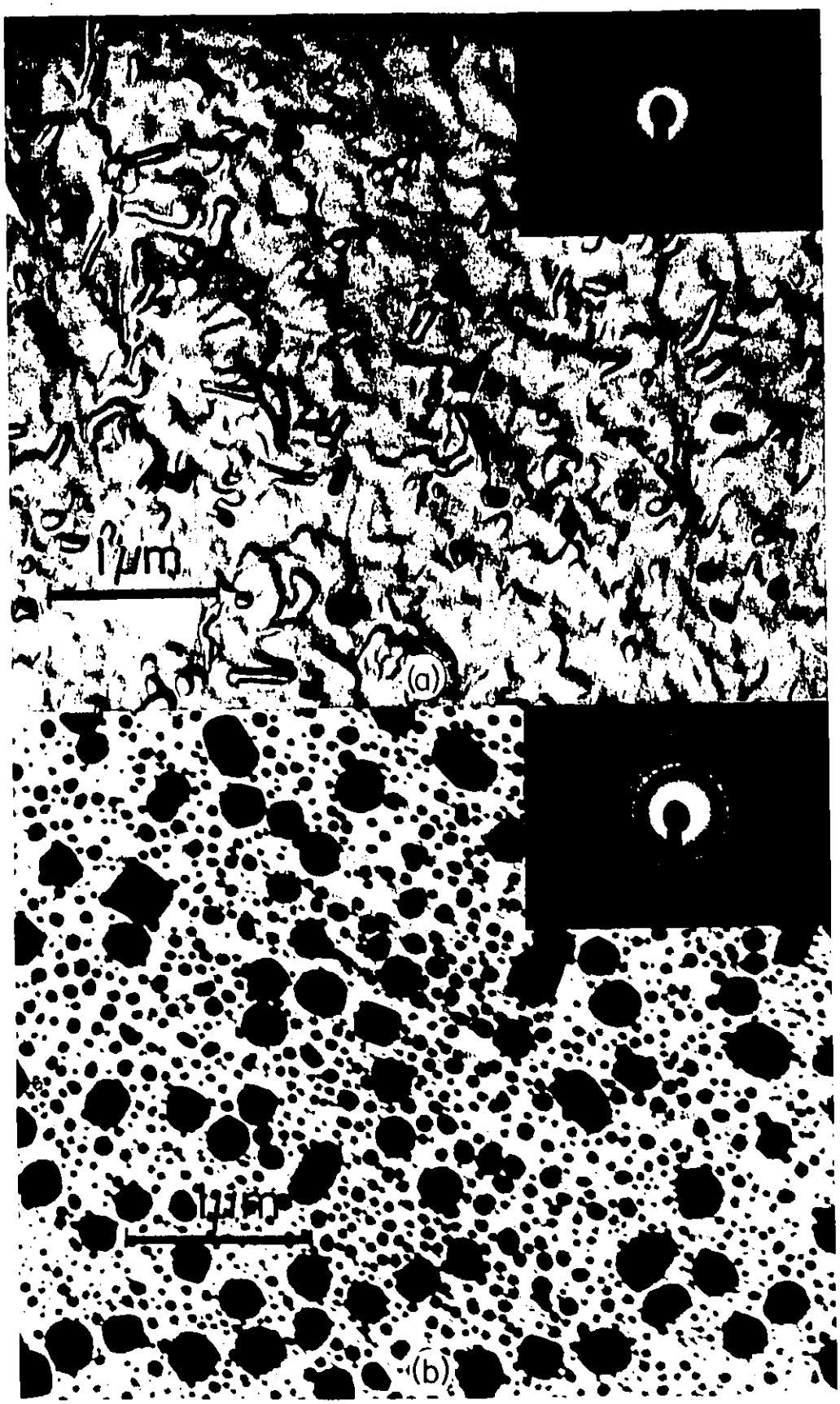
1 μm
(a)
100 nm
(b)

ring pattern, which could be indexed as γ-Al_2O_3. Oxide films formed at 1473 K in few min have the same structure as Fig.(a). In Sec.5.4.4, experimental evidence is advanced to confirm that the sub-microcrystalline film consists of Al_2O_3 solely.

The structure of a thicker film ($\sim$1 μm) formed in 30 min at 1473 and the corresponding reflection electron diffraction pattern are shown in Fig.5-12 {(a)-(d)}. The pattern exhibits sharp diffraction rings and could be analyzed as α-Al_2O_3. The film is non uniform and contains ridges extending outward and inward, Fig.(a) and (c). Faceted cavities were consistently observed at the alloy/film interface. These cavities tend to coalesce forming extended troughs between the film and alloy substrate. The film structure varies from an alloy grain to the other. The oxide film in the vicinity of an alloy grain boundary is shown in Fig.(d) where the delineation between two distinct morphologies is evident.

Inevitably, thicker scales spalled partially upon cooling. However, this occurence allowed close examination of its structure. Fig.5-13 {(a)-(e)} are SEM images of different regions of an Al_2O_3 scale formed in 15 d at 1473 K. It is apparent that the scale fractured intergranularly, Fig.(a). Electron probe microanalysis indicates that $\sim$ 0.5 wt.% Ni is dissolved in this scale. The ridges persist after this long oxidation period as evidenced by micrographs of the scale outer surface Fig.(b), and scale underside, Fig.(c). The total length of the ridges present at both interfaces account for < 10 % of the scale thickness. Few whiskers are formed at the scale

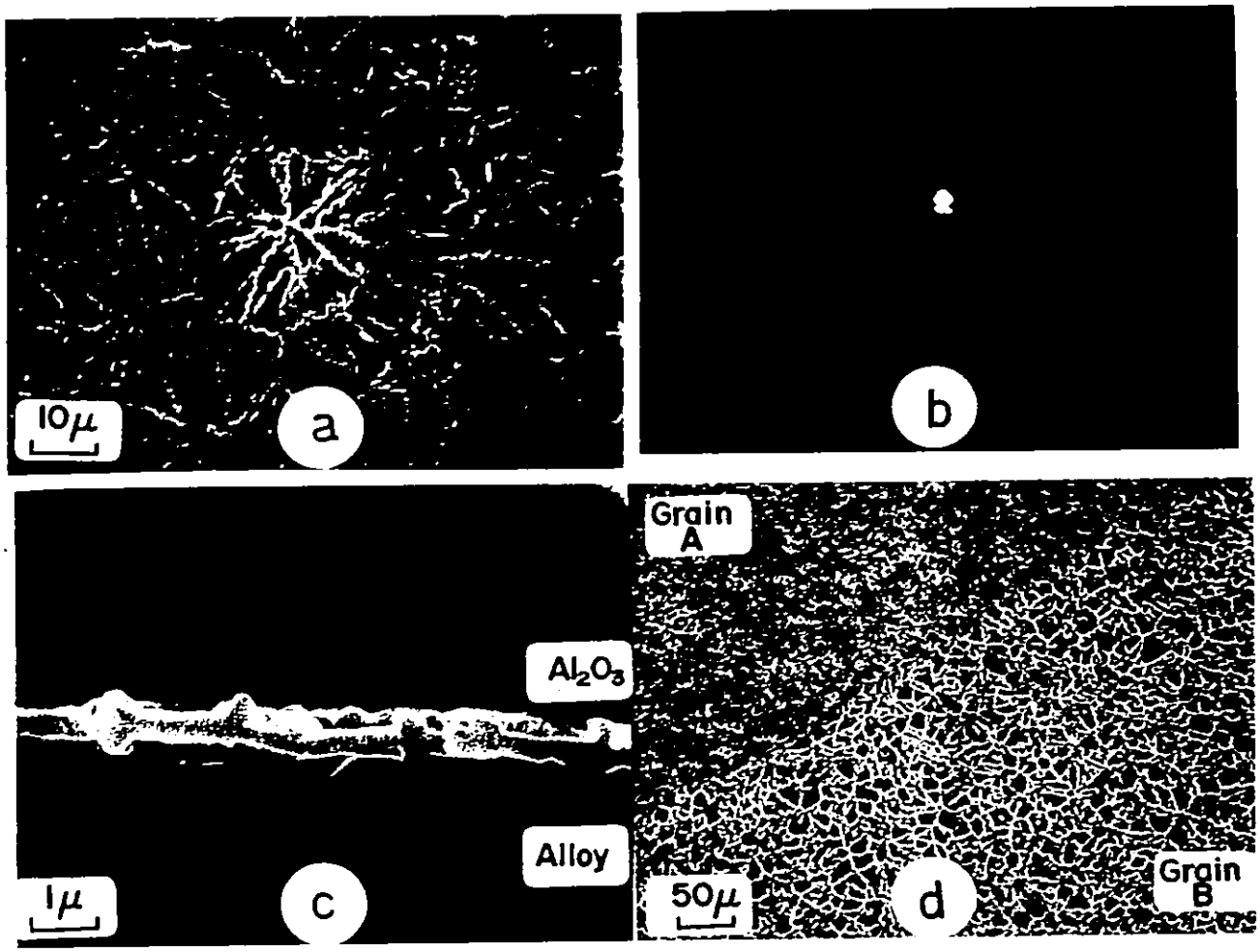

Fig.5-12. Structure of recrystallized α-Al_2O_3 film formed on Ni-32 wt.% Al alloy in 30 min at 1473 K : (a) Top view, (b) RHEED pattern, (c) Fracture cross section, (d) Film morphology in the vicinity of alloy grain boundary.

outer surface. The alloy/scale interface, which was revealed by scale spalling, is shown in Fig.(d) and (e). It has imprints from the scale corresponding to the ridges in its underside of Fig.(c) and oxide-free faceted cavities revealing crystallographic arrangements as if thermal etching has occured, Fig.(d). Spiral steps on the alloy surface are also evident in some cavities, Fig.(e). Though the structure of the cavities varied from one alloy grain to the other, the total cavity volume increased as oxidation was prolonged; compare Fig.5-12 (c) and 5-13 (d).

5.4.2 X-Ray Topography Results

In an attempt to determine if the oxide film morphology depended on the alloy sub-structure, an X-ray topography technique (Berg/Barrett) was used. These observations were made on specimens prepared during this work by Dr.T.Homma[155]. A pair of alloy grains labelled as A and B in Fig.5-14 (a), were selected for substructural examination. Grain A forms an oxide film which has a high density of oxide ridges; whereas grain B has a lower ridge density. The X-ray topographs obtained from these two grains are shown in Fig.(b) and (c). Selected areas of the topographs are also shown at higher magnification. The contrast in these micrographs can be due to either a compositional difference giving rise to a change in lattice parameter or a misorientation between alloy sub-grains[154].

Fig.5-13

Structure of thick α-Al_2O_3 scale on Ni-32 wt.% Al alloy (15 d at 1473 K, SEM images)

(a) Fracture cross section
(b) Scale outer surface
(c) Scale underside
(d) and (e) alloy/scale interface revealed by scale spalling.

Fig.5-14

X-ray Berg/Barrett topographs of Ni-32 wt.% Al alloy. Courtesy of T. Homma(155).

(a) Alloy grain structure and Al_2O_3 film structure in the vicinity of a grain boundary.
(b) and (c) X-ray topographs of grains A and B in Fig.(a)

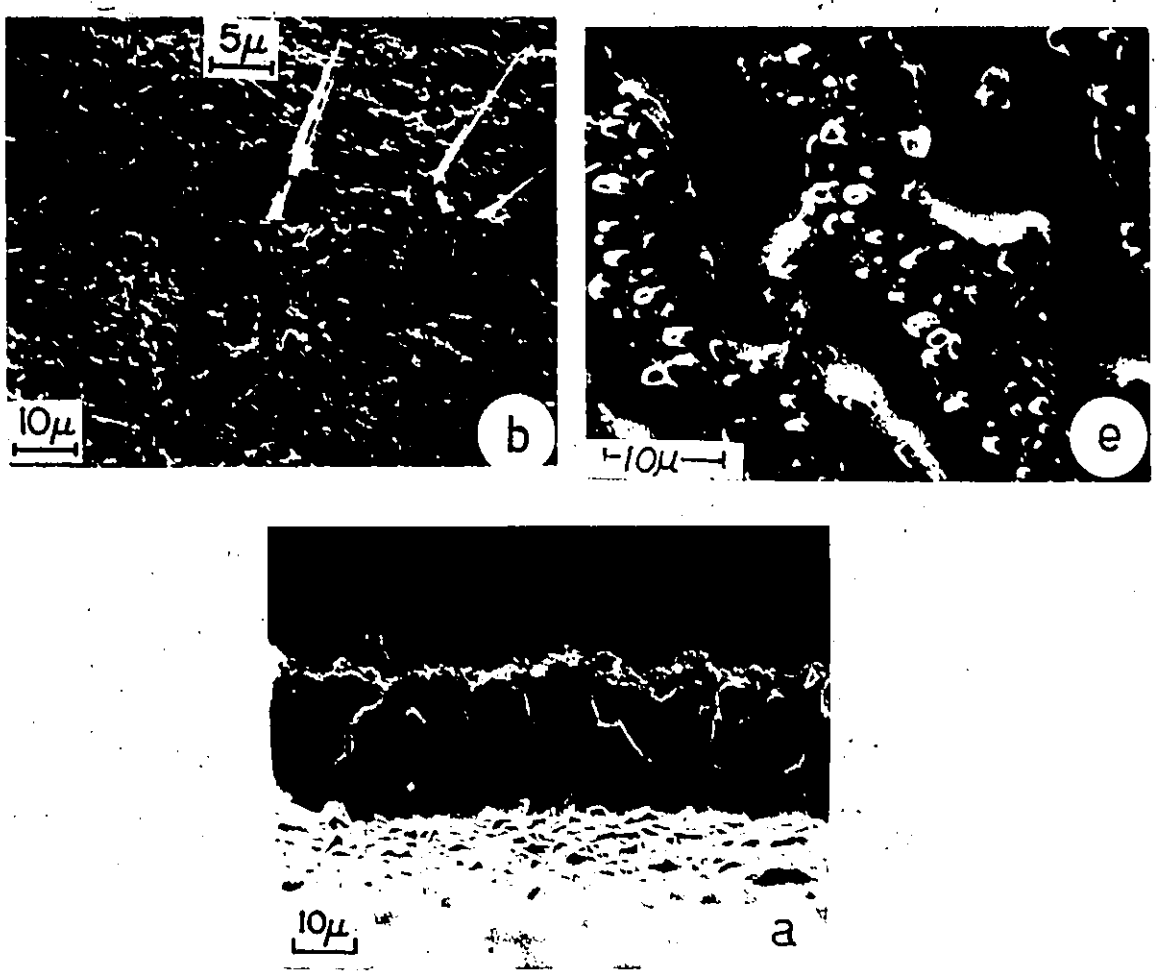

Fig.5-13

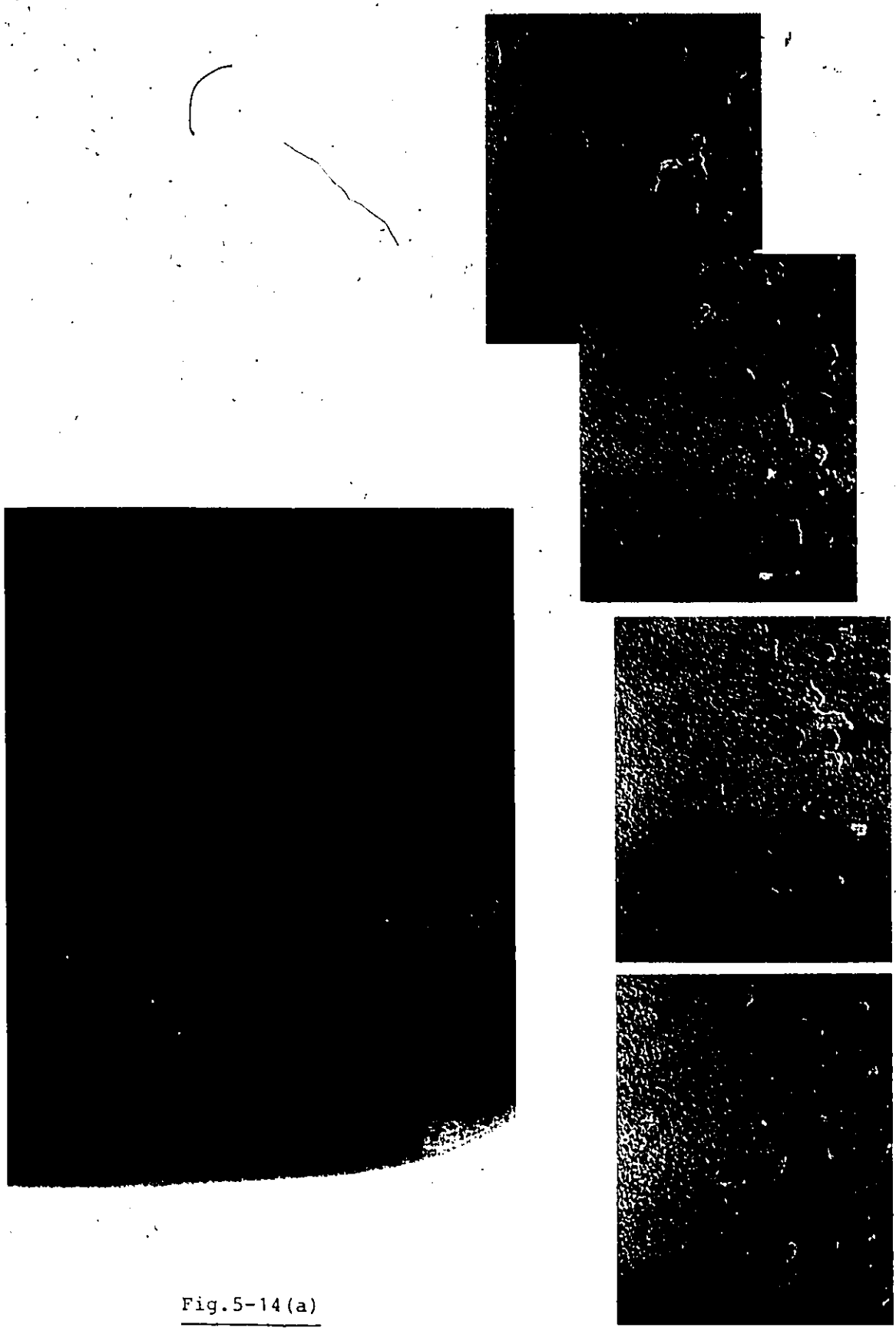

Fig.5-14(a)

Grain A

x52

x200

a'

a''

Fig.5-14(b)

Grain B

x200

x52

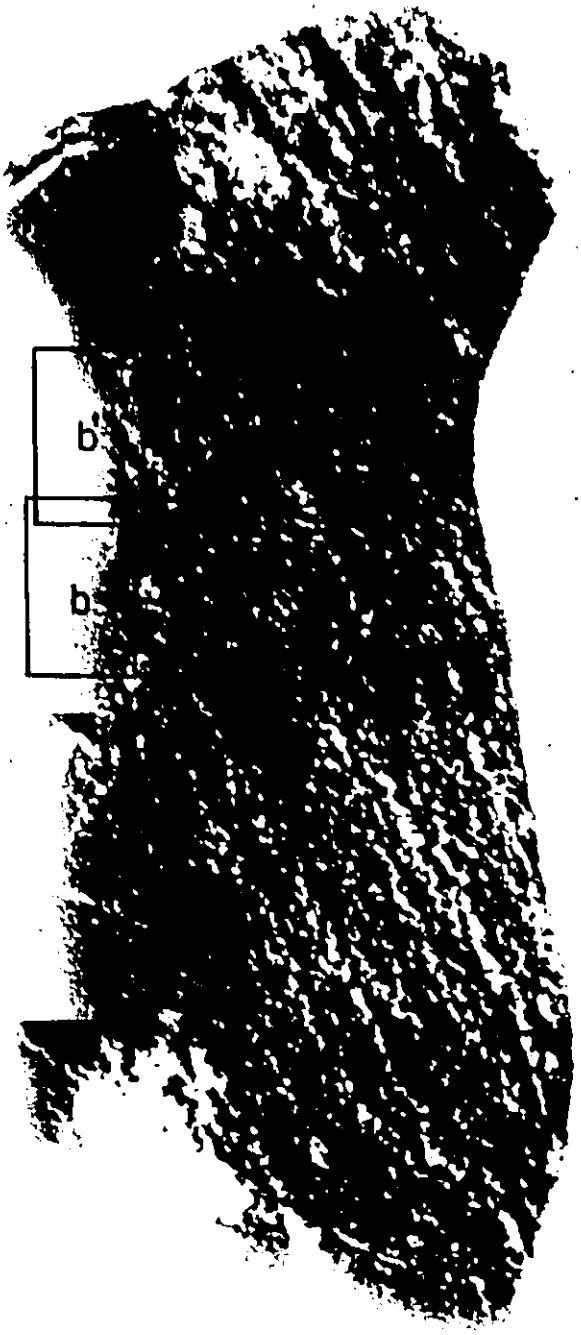

Fig.5.14(c)

5.4.3 Scale and Grain Growth Results

The thicknesses of Al_2O_3 scales were determined from SEM images of polished cross sections enlarged 8000 times. They were measured to an accuracy of 0.5 mm which corresponds to o.1 μm. Each data point represents the average of 15 readings taken from three samples oxidized in a batch. In Fig.5-15 {(a) and (b)}, the reaction kinetics at 1473 and 1573 K are presented as average scale thicknesses and the square of these thicknesses versus time. Parabolic kinetics were not observed in this case; a parabolic plot, Fig.(b) yields a curve which has a slope that declines with time.

Since the specimens did not oxidize parabolically as expected in the case of lattice diffusion controlled reaction and in addition, there is evidence that the transport properties of Al_2O_3 are structurally dependent (Sec.3.4.3), it was decided to assess the contribution of structural imperfections in the scale (grain boundaries) to its growth. The grain size was determined from fracture cross sections of partially spalled Al_2O_3 flakes. The grain diameter was measured parallel to the scale interfaces with the same accuracy of the thickness measurements. In each case, 100 grains, chosen at random from different parts of the scale, were used to determine the grain size distribution. The results of these measurements for a number of oxide scales formed at 1473 and 1573 K are shown plotted as grain fraction versus grain diameter in Fig. 5-16 {(a) and (b)}. The average grain size and its square

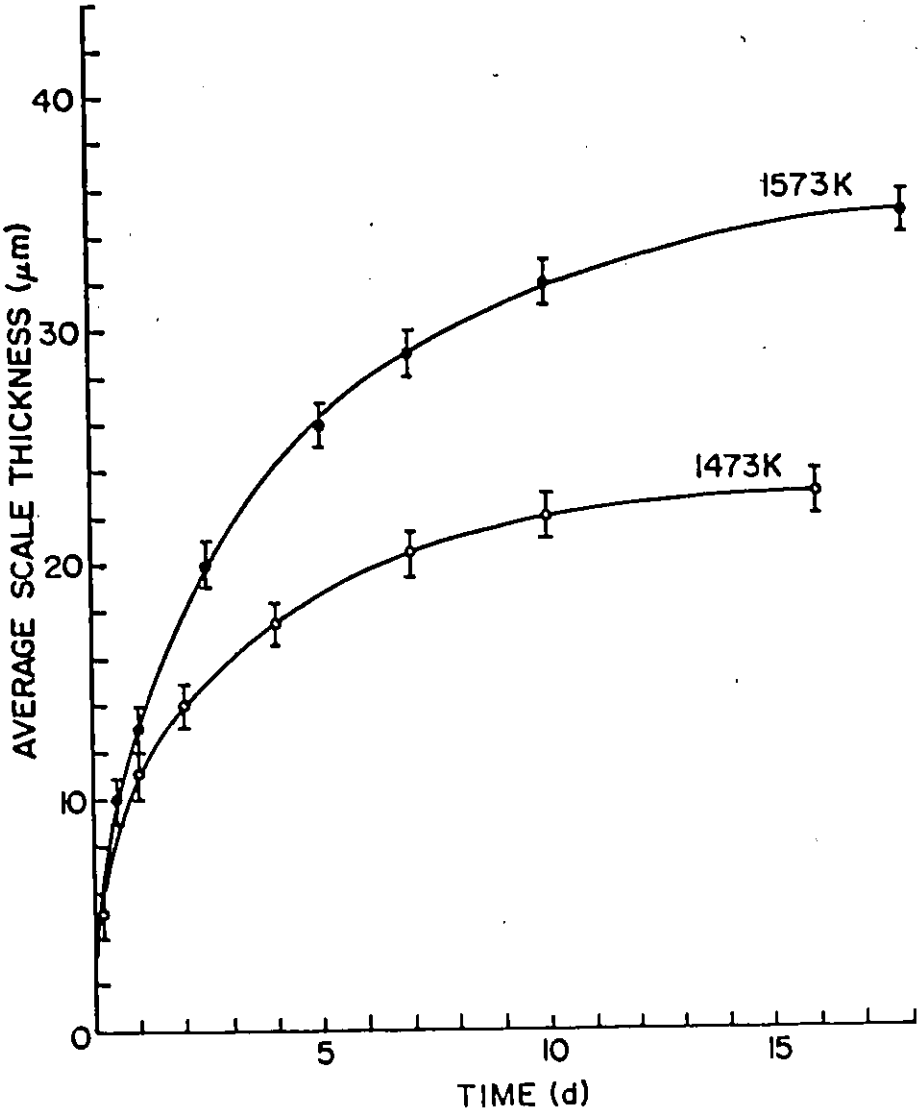

Fig.5-15(a). Al_2O_3 growth kinetics on Ni-32wt.% Al alloy : linear plot.

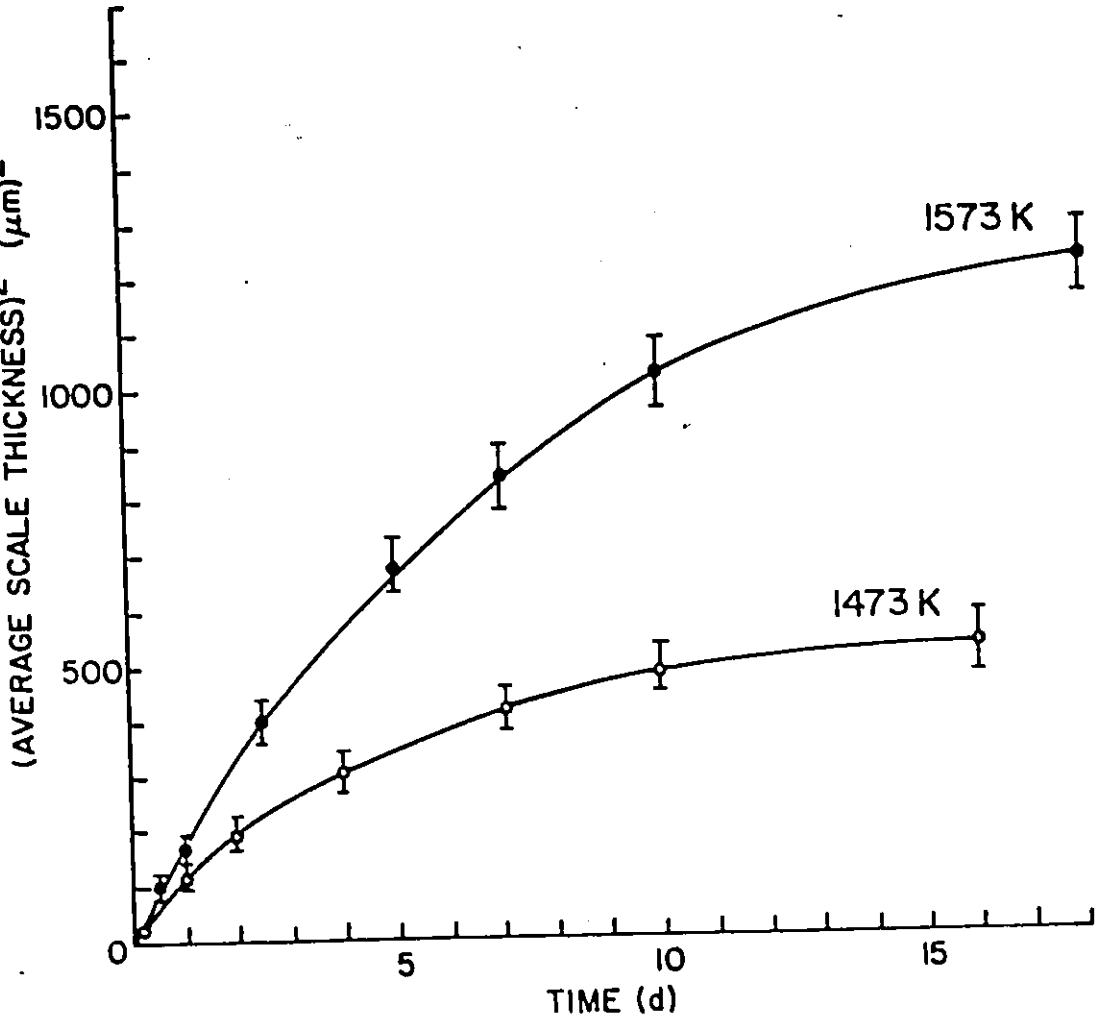

Fig.5-15(b). Al_2O_3 growth kinetics on Ni-32wt.% Al alloy : parabolic plot.

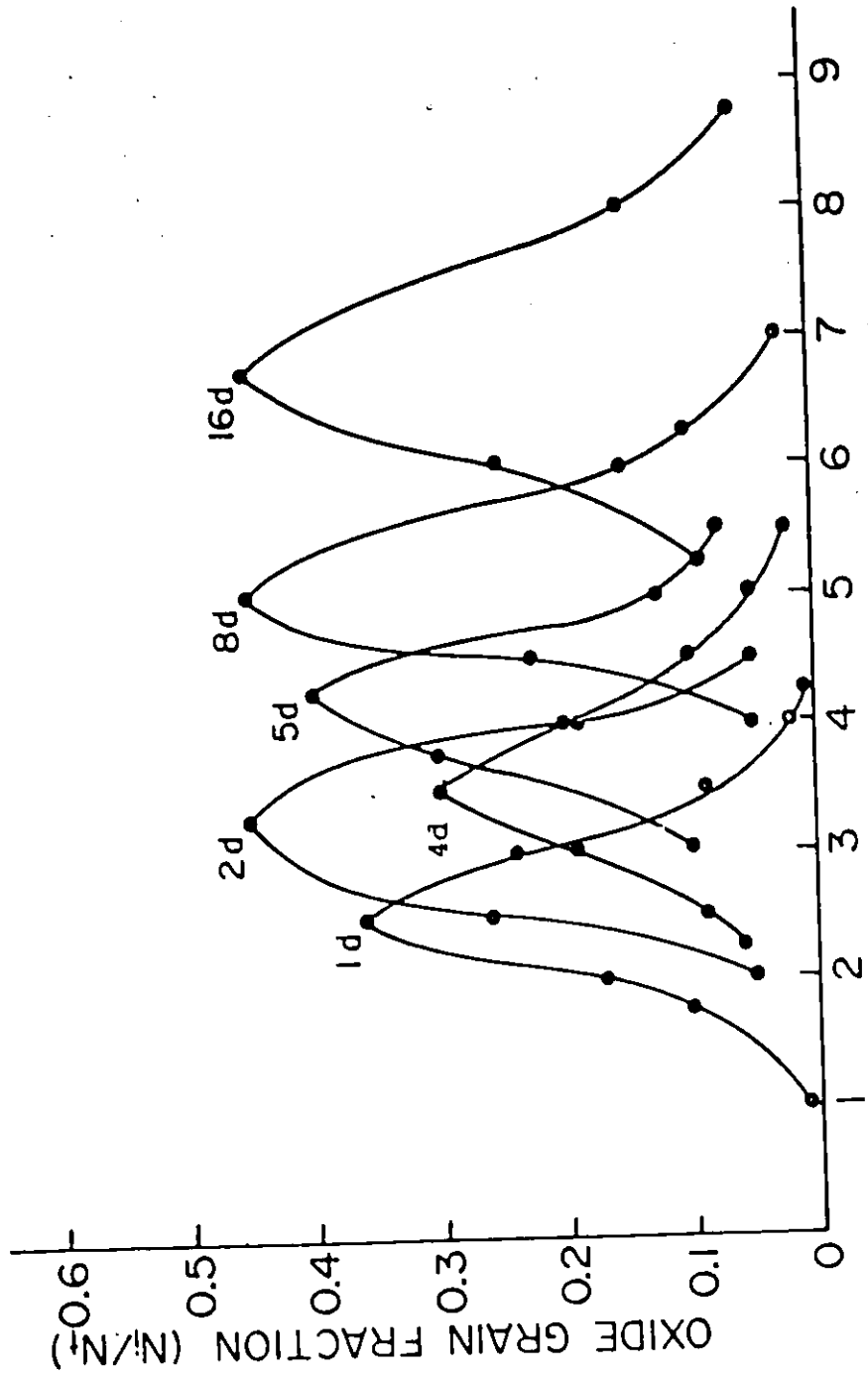

Fig.5-16(a). Al_2O_3 grain size distribution and growth at 1473 K.

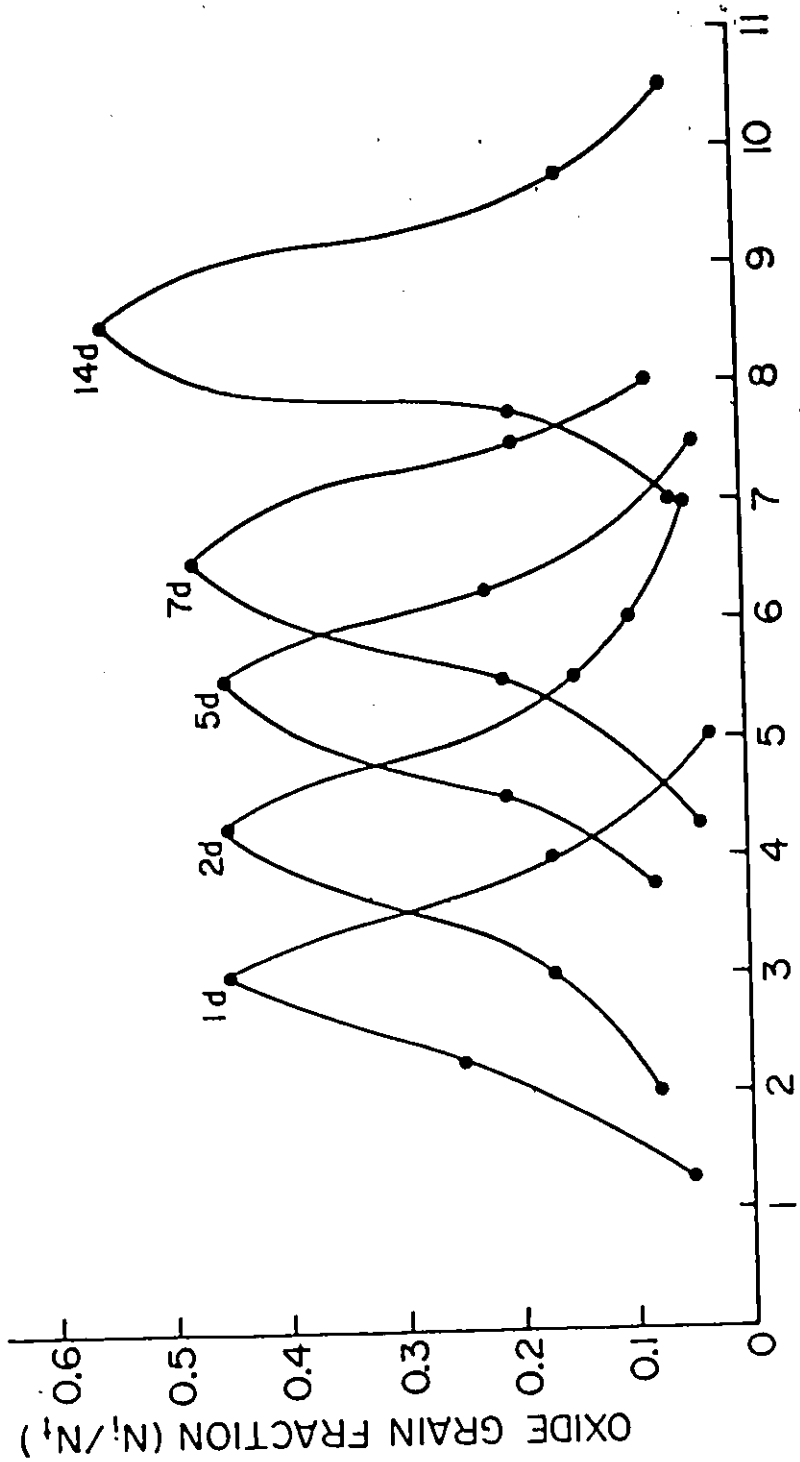

Fig.5-16(b). Al_2O_3 grain size ditribution and growth at 1573 K.

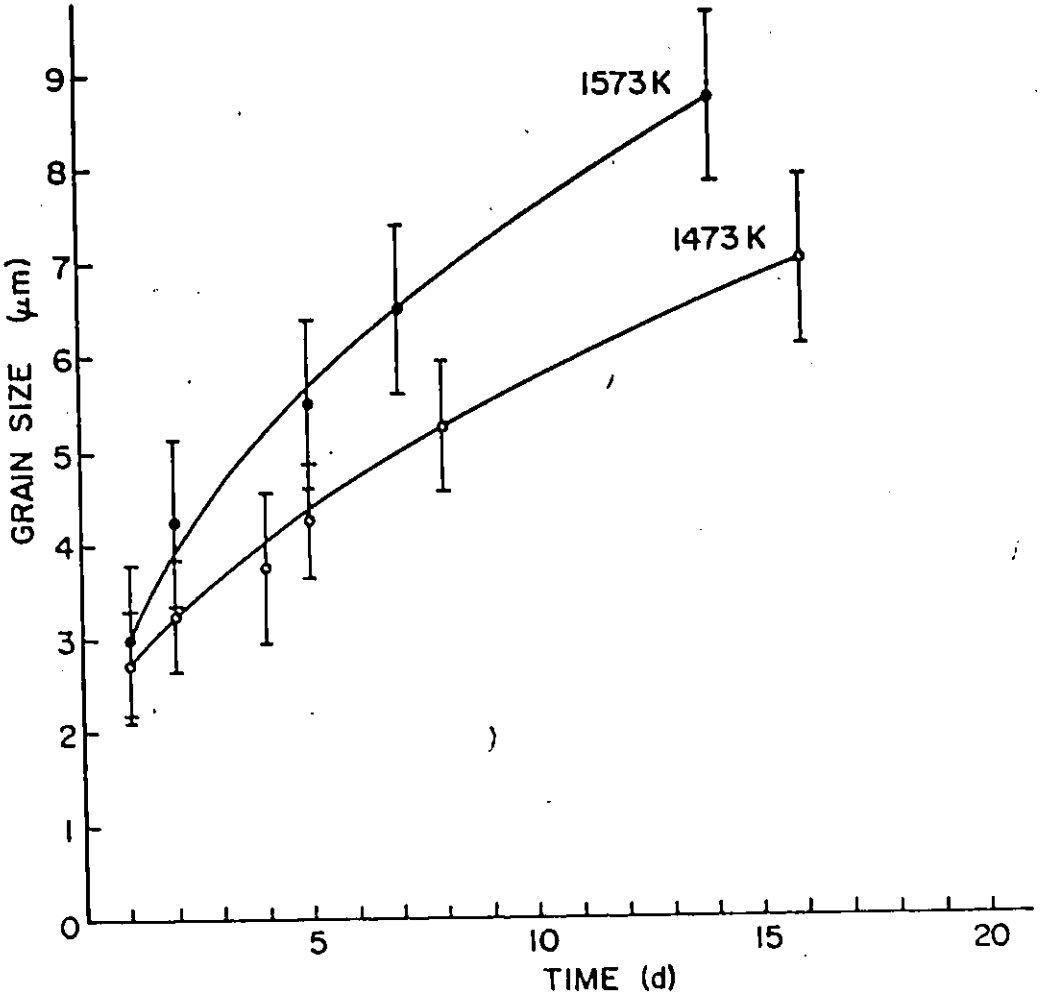

Fig.5-17(a). Al_2O_3 scale grain growth: linear plot.

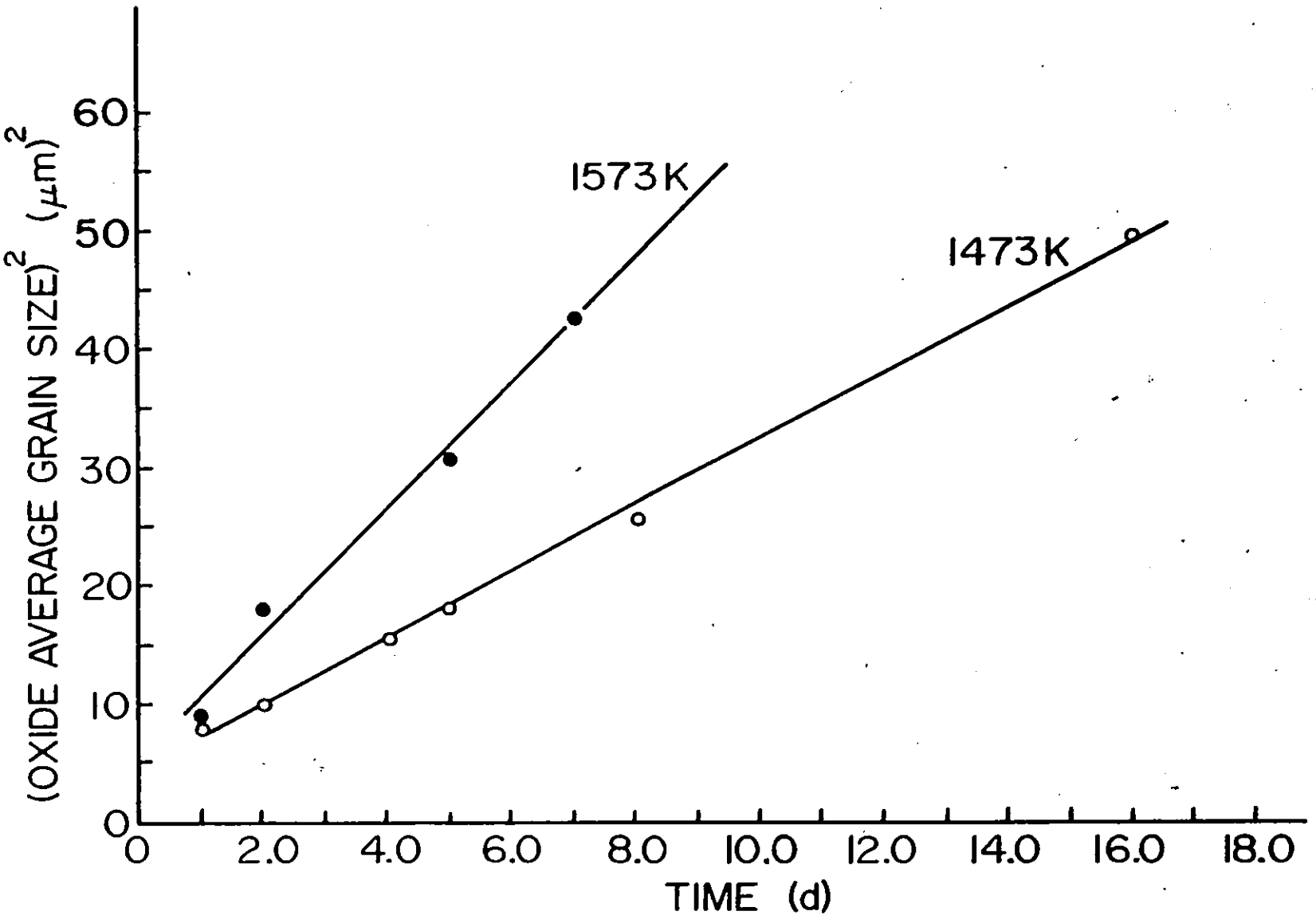

Fig. 5-17 (b). Al_2O_3 scale grain growth : parabolic plot.

are plotted versus time and its root in Fig. 5-17 (a) and (b) respectively. The latter graph yields a straight line which indicates that the average grain size follows the general grain growth relation :

$$D_t^2 - D_o^2 = k't \qquad (2.11)$$

Since grain growth is a thermally activated process, its temperature dependence can be expressed as :

$$D = D^o \exp(-E_G/RT) \qquad (5.1)$$

where E_G is the activation energy for grain growth. Its value , determined from these measurements, is 133 kJ/g mole.

5.4.4 Inert Marker Results

Inert marker techniques allow the identification and estimation of the relative mobilities of the diffusing species in oxide films. In the present study, Auger electron spectroscopy in combination with depth profiling by Ar ion sputtering was employed to determine the location of a thin inert marker during the growth of oxide film on the Ni-32 wt.% Al alloy. The sensitivity of this technique with respect to concentration and depth allows the use of an extremely thin marker (3∿5 nm) in order that its interference with film growth is minimized.

The specimen was oxidized in static oxygen (1 atm) at 1273 K for 5 min. In Sec.5.4.1, it was shown that a sample oxidized in the same condition forms an oxide film 120 nm thick exhibiting few morphological features and a diffraction pattern consisting of halos.

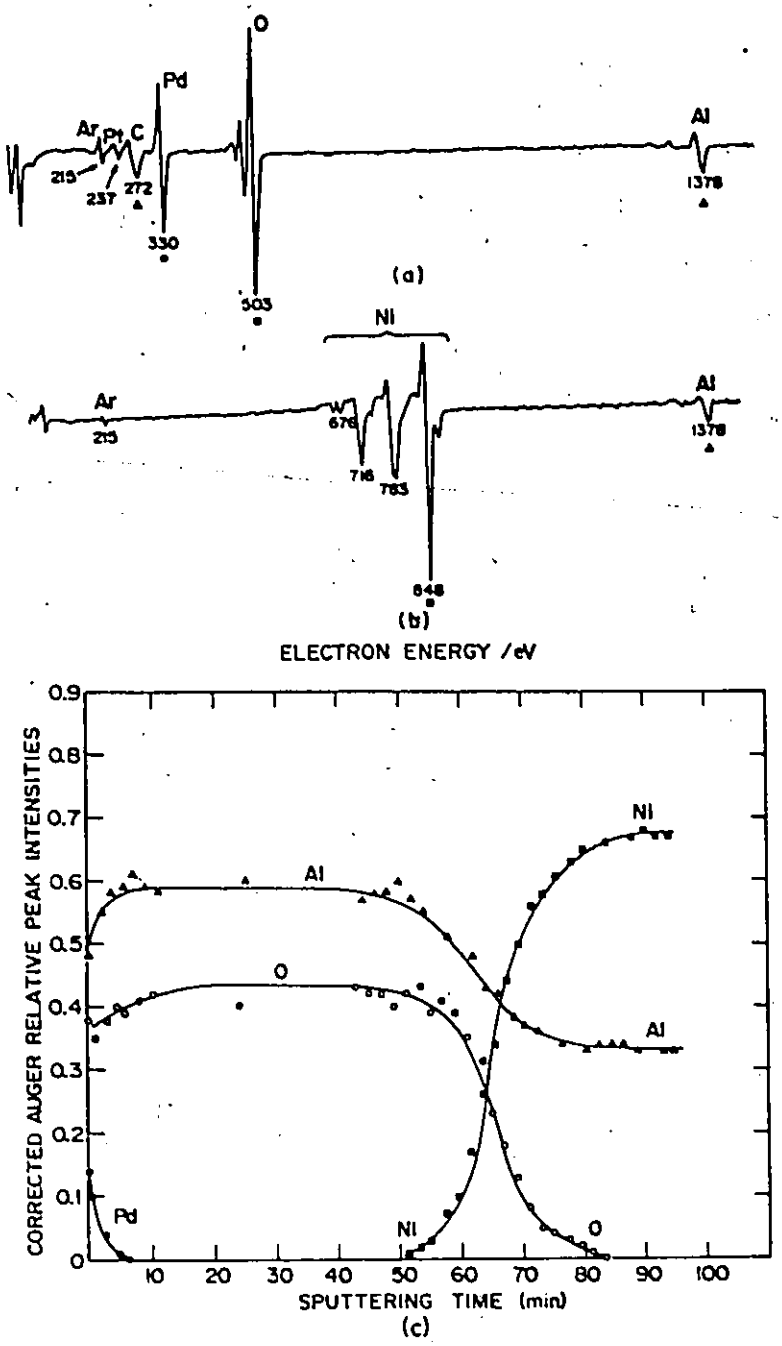

Fig.5-18. AES results for oxidized Ni-32 wt.% Al alloy (5 min at 1273 K) : (a) and (b) spectrums before and after sputtering the oxide film, (c) concentration profile across the film.

Auger electron spectra of the oxidized specimen prior to and after sputtering the oxide film and the concentration profile of its constituents are shown in Fig.5-18 {(a)-(c)}. Disregarding Pd, the film consists of pure Al_2O_3 since Ni could only be detected in the vicinity of the alloy/oxide interface. It is evident that the Pd marker resides at the outer film surface (oxide/gas interface) and is sputtered completely away in less than 10 min.

CHAPTER 6

ANALYSIS AND DISCUSSION OF EXPERIMENTAL RESULTS

6.1 INTRODUCTION

When a Ni-Al alloy is exposed to oxygen at high temperatures, several oxides can form according to the following reactions :

$$Ni_{(alloy)} + 1/2\ O_2 = NiO \quad (6.1)$$

$$2\ Al_{(alloy)} + 3/2\ O_2 = Al_2O_3 \quad (6.2)$$

$$Ni_{(alloy)} + 2\ Al_{(alloy)} + 2\ O_2 = NiAl_2O_4 \quad (6.3)$$

Considering the standard free energy of formation of the pure oxides (Table 3-4) and overlooking for the moment the effect of the activities of alloy components on oxide stability, it can be concluded that NiO would be converted to the more stable oxides Al_2O_3 or $NiAl_2O_4$ via the following reactions :

$$3\ NiO + 2\ Al_{(alloy)} = Al_2O_3 + 3\ Ni_{(alloy)} \quad (6.4)$$

$$NiO + Al_2O_3 = NiAl_2O_4 \quad (6.5)$$

Initially, the oxides are not necessarily in equilibrium with the alloy in view of their rapid formation. The early stage, which is referred to as "transient oxidation", is sensitive to surface preparation and exposure to the oxidizing atmosphere. Since a large difference in thermodynamic and diffusion properties exists between NiO and Al_2O_3, Ni-Al alloys are expected to

undergo a long transient period before steady state scaling is attained, especially alloys with compositions which border between forming either NiO or Al_2O_3 as a stable oxide phase. Eventually, as the oxidation process is diffusion-controlled, the concentrations of the diffusing species at the alloy/scale interface assume fixed values which are determined by alloy bulk composition and the interplay between the diffusion processes in the alloy and oxide phases. Only oxides, which are thermodynamically stable with respect to the steady state alloy interfacial concentration, continue to grow.

The stability of an oxide in contact with its parent alloy is determined by the value of its dissociation pressure with respect to the oxygen pressure in the ambient atmosphere. For example, the dissociation pressure of NiO in equilibrium with a Ni-Al alloy can be calculated providing that the activities in the alloy and oxide phases and the dissociation pressure of NiO in contact with pure Ni ($p_{O_2}^*$) are known, as shown in the following thermodynamic treatment :

$$2\,Ni + O_2 = 2\,NiO \qquad (6.6)$$

$$2\,Ni_{(alloy)} + O_2 = 2\,NiO_{s.s.}\dagger \qquad (6.7)$$

Assuming that aluminum is slightly soluble in NiO, the application of the mass action law to the above equilibria yields :

$$K = \exp(-\Delta F_{f_{NiO}}/RT) = \frac{(a_{NiO})^2}{(p_{O_2}^*)} = \frac{(a_{NiO_{s.s.}})^2}{(a_{Ni\,alloy})^2\,(p_{O_2})} \qquad (6.8)$$

---

† solid solution.

Then,

$$P_{O_2} = \frac{(a_{NiO_{s.s.}})^2 \, (P_{O_2}^*)}{(a_{Ni_{alloy}})^2} \qquad (6.9)$$

If the calculated dissociation pressure is greater than the oxygen pressure in the ambient atmosphere, the oxide is converted to a stable one via a displacement reaction similar to Eq. (6.4).

The main purpose of this work was to study the microstructure, growth rate and mechanism of formation of Al_2O_3 on Ni-Al alloys at high temperatures in pure oxygen at one atmosphere. In the following sections, the experimental results are interpreted in terms of the thermodynamic and diffusion data for the Ni-Al-O system. Scale growth models are proposed to rationalize the experimental observations.

6.2 INTERNAL PRECIPITATION OF Al_2O_3 AND DUPLEX SCALE FORMATION

6.2.1 Introduction

The Ni-2 wt.% Al alloy oxidizes parabolically forming a duplex scale and a precipitation zone in the alloy. Proceding from the scale surface, the three layers, which thicken individually according to a parabolic relation, are Al-doped NiO, NiO + $NiAl_2O_4$ and Al_2O_3 + Al-depleted alloy. Through the temperature range investigated, the oxidation rate constants are one order of magnitude larger than those for pure Ni. These results are in fair agreement with other investigations[16,18].

Since internal oxidation occurs, it appears that the Al alloy concentration is below the critical value necessary to form a continuous Al_2O_3 scale, as discussed in Sec.2.5.2. The

rodlike Al_2O_3 precipitates extend through the precipitation zone parallel to the growth direction. No change in their orientation was observed from one alloy grain to the other. The latter observation indicates that they are formed independent of alloy grain orientation.There is approximately an increase of 7% in volume accompanying the formation of Al_2O_3 precipitates in the alloy. Thence, Al_2O_3 presumably is precipitated incoherently in the alloy. Its growth in the form of continuous rods, rather than isolated precipitates, minimizes its surface area and consequently its total interfacial energy.

In the following, a scale growth model, which is schematically illustrated in Fig.6-1, is proposed.

6.2.2 Growth of the Alloy Layer Containing Al_2O_3 precipitates

The formation of Al_2O_3 as discrete crystallites depletes the alloy aluminum content to the extent that NiO becomes thermodynamically stable. The rapid lateral growth of NiO results in the development of a film which isolates the Al_2O_3 crystallites from the ambient atmosphere. For their continual growth as rods, oxygen must be supplied at the inner reaction front. Several mechanisms are possible :

i) Lattice diffusion of oxygen through the NiO scale. Oxygen diffusion through NiO cannot account for the observed growth rate of the Al_2O_3 precipitates. The measured values of the parabolic rate constants for nickel oxidation, which agree with the results of other researchers compiled in Fig.3-6, were presented in Table 5-1. Since NiO has a small homogeneity

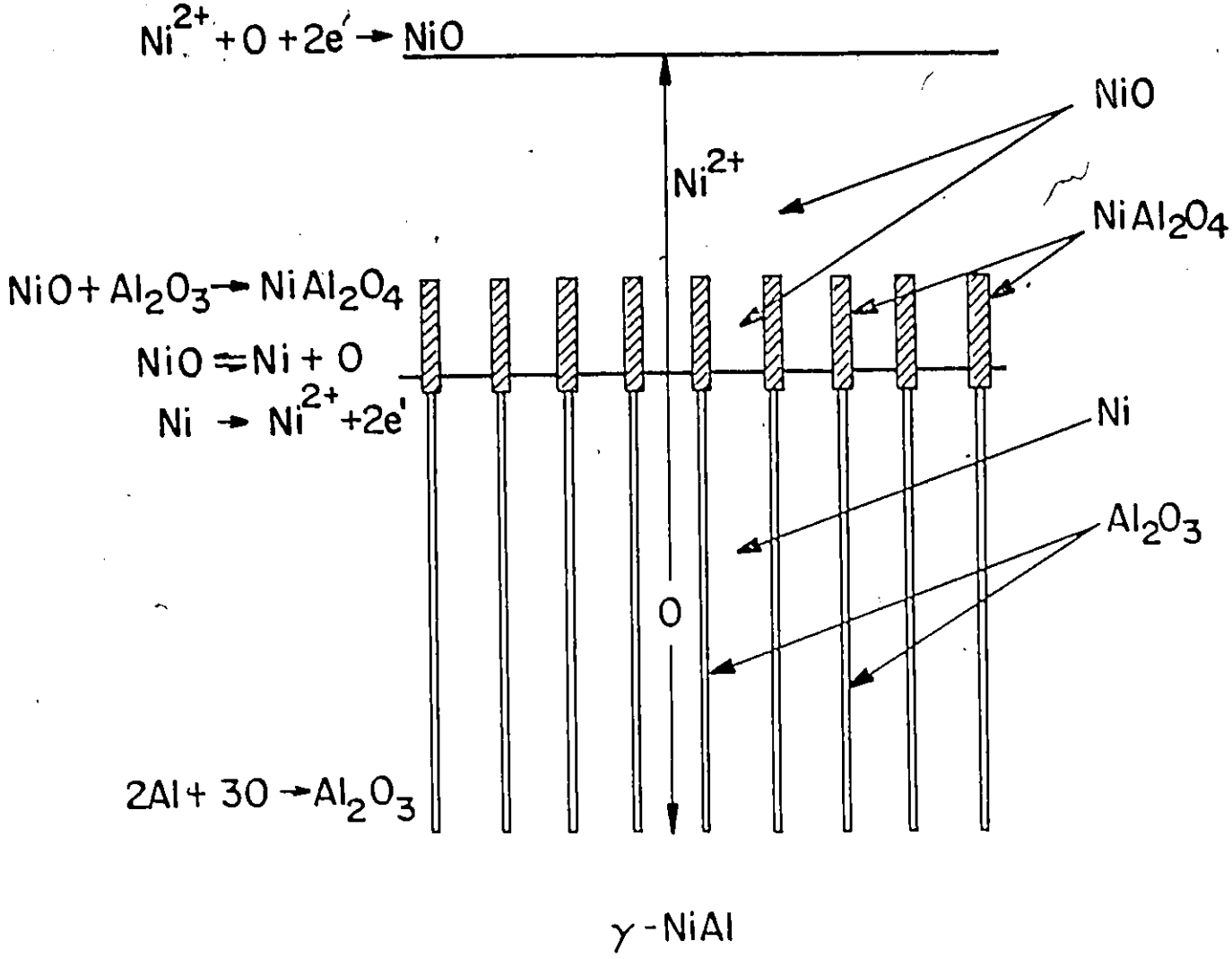

Fig.6-1.

Schematic model for scale growth on Ni-2 wt.% Al alloy.

range, the rational parabolic rate constant can be expressed by Eq.(2.6). It was shown in Sec.3.3.3 that, assuming predominant Ni diffusion, Eq.(2.6) is reduced to

$$k_r(\text{g eq.cm}^{-1}.\text{sec}^{-1}) = 3\,\bar{C}_{eq}.\,D^{o}_{Ni} \qquad (3.5)$$

The rational parabolic rate constant k_r (g eq.cm^{-1}.sec^{-1}) is related to k_p (g^2.cm^{-4}.sec^{-1}) by

$$k_p = k_r \times Eq.W._{NiO} \times \rho_{NiO} \qquad (6.10)$$

Using the values of D^{o}_{Ni} and ρ_{NiO} listed in Table 3-4, Eq.(3.5) and (6.10) can be used to calculate k_p. The result of this calculation at T = 1473 K is $k_p = 1.3\times10^{-9}$ g^2.cm^{-4}.sec^{-1}. The experimental value is $k_p = 1.2\times10^{-9}$ g^2.cm^{-4}sec^{-1}. The agreement between the observed and calculated values within 10%, which is within the accuracy of the determination of D^{o}_{Ni} used in this calculation, demonstrates that the assumption of predominant nickel migration in the thick NiO scales is valid. The foregoing derivation and the results of oxygen tracer diffusion measurements[107], which show that oxygen diffusivity in NiO single crystals is two orders of magnitude less than nickel, lead to the conclusion that lattice diffusion cannot supply oxygen from the gas phase at a rate sufficient to support the observed growth rate of the Al_2O_3 internal precipitates.

ii) Oxygen diffusion along imperfections in the scale. Since the outer NiO layer has a coarse grain structure (average grain size 30 μm), oxygen preferential migration along grain boundaries or cracks would lead to localized growth of the internal precipitation zone rather than the observed uniform

thickening. The fine pores, which were observed at the intermediate region of the scale, did not form a continuous network. Thence, they cannot contribute to the transport of the oxidant from the gas phase to the reaction front. Therefore, both lattice and short circuit oxygen diffusion through NiO are excluded as possible mechanisms to support the growth of the Al_2O_3 precipitates.

iii) Solid state displacement reaction*

It is suggested that the Al_2O_3 precipitates result from a solid state displacement reaction between the NiO scale and Al present in the alloy. At the alloy/scale interface, the following equilibria prevail :

$$NiO = Ni_{(alloy)} + 1/2\ O_2 \qquad (6.1)$$

$$1/2\ O_2 = O_{(alloy)} \qquad (6.11)$$

From Sieverts' law, the concentration of oxygen dissolved in the alloy at the alloy/scale interface is given by :

$$C_O^o = k_S (P_{O_2})^{\frac{1}{2}} \qquad (6.12)$$

Since aluminum has a higher affinity for oxygen than nickel, the oxygen concentration dissolved in the alloy at the Al_2O_3 precipitation front, C_O^i, must be $<< C_O^o$. Thence, the oxygen concentration gradient results in its inward diffusion within the alloy precipitation zone to react with aluminum at the precipitation front :

$$2\ Al_{(alloy)} + 3\ O_{(alloy)} = Al_2O_{3(alloy)} \qquad (6.2)$$

The net result is the growth of the Al_2O_3 precipitates at the

---

* Experimental evidence is given in Appendix A.

expense of the NiO scale.

In the following, a simplified treatment is used to demonstrate that the growth of the precipitation zone is controlled by oxygen diffusion in the alloy. The oxygen flux in the alloy is given by :

$$J_O = (1-f)\left\{-D_{OO}\frac{\delta C_O}{\delta x} - D_{OA}\frac{\delta C_A}{\delta x}\right\}$$

$$= (1-f)\left\{-D_{OO}\left(\frac{\delta C_O}{\delta x} + \varepsilon_O^A C_O \frac{\delta C_A}{\delta x}\right)\right\} \qquad (6.13)$$

where f is is the fractional surface covered by the precipitates and ε_O^A is the interaction coefficient for oxygen with aluminum. Since the alloy in the internal precipitation zone is essentially pure Ni*, $\varepsilon_O^A = 0$ and Eq.(6.13) is reduced to :

$$J_O = (1-f)\left\{-D_{OO}\frac{\delta C_O}{\delta x}\right\} \qquad (6.14)$$

The thickening rate of the precipitation zone is given by :

$$\frac{\delta x}{\delta t} = \frac{J_O}{f}\left\{\frac{M.W.Al_2O_3}{1.5\ M.W.O_2}\right\} V_{Al_2O_3} \qquad (6.1\ )$$

Substituting J_O in the last expression and integrating , assuming D_{OO} independent on alloy concentration,

---

* The amount of aluminum remaining in solution at the alloy/scale interface can be calculated by considering the following equilibrium :

$$2\ Al_{(alloy)} + 3\ O_{(alloy)} = Al_2O_{3(alloy)}$$

$$\exp(\Delta F_{f_{Al_2O_3}}/RT) = (a_{Al_{alloy}})^2\ (p_{O_2})^{3/2}$$

where p_{O_2} corresponds to the coexistence of alloy + Al_2O_3 + $NiAl_2O_4$.

$a_{Al(alloy)} = 10^{-17}$, which corresponds to few ppm of $Al^{(159)}$.

$$x^2 = \frac{2(1-f)}{f}\left(\frac{M.W.Al_2O_3}{1.5\ M.W.O_2}\right) \nu_{Al_2O_3} D_{OO}\ \Delta C_O\ t$$

$$= k\ t \qquad (6.16)$$

Since trace amounts of Al only remain in solution in the Ni-Al alloy upon the precipitation of Al_2O_3, the oxygen concentration at the alloy/scale interface can be assumed equal to its solubility in pure Ni. Due to the high aluminum affinity for oxygen, the oxygen concentration at the Al_2O_3 precipitation front can be considered as nil. At T = 1273 K, C_O in Ni = 0.051 at.%[77], D_O in Ni = 4×10^{-9} $cm^2.sec^{-1}$ [161], f = 0.07 (determined experimentally). Substituting these values in Eq.(6.16), k = 18.7 $\mu m.h^{-\frac{1}{2}}$ which is in close agreement with the experimentally determined value, k = 19.8 $\mu m.h^{-\frac{1}{2}}$.

6.2.3 Growth of the inner NiO-$NiAl_2O_4$ layer in the external scale

Since aluminum solubility in NiO is low[148], the Al_2O_3 precipitates are converted to $NiAl_2O_4$ via reaction (6.5). $NiAl_2O_4$ is formed by counter-current cation diffusion[146] according to the following reactions which occur at the NiO/$NiAl_2O_4$ and Al_2O_3/$NiAl_2O_4$ interfaces, respectively :

$$2\ Al^{3+} + 4\ NiO = NiAl_2O_4 + 3\ Ni^{2+} \qquad (6.17)$$

$$3\ Ni^{2+} + 4\ Al_2O_3 = 3\ NiAl_2O_4 + 2\ Al^{3+} \qquad (6.18)$$

In this NiO and Al_2O_3 diffusion couple study[146], a marker resided within the spinel layer at a relative distance of 1 : 3.2 from the NiO/$NiAl_2O_4$ and Al_2O_3/$NiAl_2O_4$ interfaces, respectively. Accordingly, the counter-current Al and Ni diffusion would result in the advance of the spinel phase in the NiO scale to form a two-pnase layer and in the rodlike Al_2O_3

precipitates present in the alloy at a thickness ratio 1 : 3.2 . Tne limitations imposed by the analytical techniques, however, did not permit measurements to establish if $NiAl_2O_4$ extended into the alloy at the scale/alloy interface.

The observed growth of $NiAl_2O_4$ in NiO/Al_2O_3 diffusion couples at T = 1473 K is k = 0.6 $\mu m.h^{-\frac{1}{2}}$ [146] of whicn one fourth, i.e. 0.15 $\mu m.h^{-\frac{1}{2}}$, is due to aluminum diffusion according to Eq.(6.17). This value is much smaller than the observed advance rate of $NiAl_2O_4$ in NiO, k = 11.4 $\mu m.h^{-\frac{1}{2}}$. thence, the formation of this layer cannot be interpreted by a simple direct solid state reaction between the external NiO scale and Al_2O_3 precipitates.

It is conjectured that the partial consumption of the NiO scale by the displacement reaction, Eq.(6.4), results in its recession to maintain its contact with the alloy surface. The Al_2O_3 particles consequently become embedded in NiO where they are converted to $NiAl_2O_4$ by counter-current lateral diffusion of Al and Ni ions according to Eq.(6.17) and (6.18). Since Al is highly soluble in $NiAl_2O_4$ whereas Ni is not soluble[149], Al ions released by Eq.(6.18) dissolve in $NiAl_2O_4$ and Ni ions released by reaction (6.17) migrate outward to the scale surface.

If this latter mechanism and the postulated displacement reaction were operative, the amount of Al_2O_3 precipitates would be equivalent to the amount of NiO present in the inner layer. The ratio of these two quantities is given by :

$$\frac{k(\text{prec. zone } \mu m.h^{-\frac{1}{2}}) \times f \times \rho Al_2O_3/Eq.W.Al_2O_3}{k(\text{inner layer } \mu m.h^{-\frac{1}{2}}) \times (1-f) \times \rho NiO/Eq.W.NiO}$$

The value of this ratio is 0.5, which within the accuracy of the determination of the rate constants and f and the assumption that the oxides are pore-free, supports the previous conclusion. Since the recession rate of the NiO scale is much faster than the growth rate of $NiAl_2O_4$, the Al_2O_3 particles would not be completely transformed to spinel upon their incorporation into the external scale. This latter conclusion could not be verified experimentally.

The partial dissolution of Al_2O_3 in the inner and outer NiO layers results in the alteration of its defect structure according to the following equation :

$$Al_2O_3 = 2\,Al_{Ni}^{\cdot} + V_{Ni}'' + 3\,O_O^{\times} \qquad (6.19)$$

The increase in the cation vacancy concentration enhances the diffusion of Ni in the precipitate-free region of the scale. According to the Wagner model, the parabolic rate constant is directly proportional to the nickel vacancy concentration, Eq.(3.5); thence,

$$\frac{k}{k^o} = \frac{V_{Ni}}{V_{Ni}^o} \qquad (6.20)$$

where k^o and k are the rate constants for NiO growth on pure Ni and Ni-2 wt.% Al alloy, respectively. At T = 1273 K, $V_{Ni}^o = 10^{-4}$ [39], $k^o = 14.4\ \mu m^2.h^{-1}$ * and $k = 26.6\ \mu m^2.h^{-1}$. Substituting these values in (6.20),

$$\{Al_{Ni}\} = 2\,\{V_{Ni}\} = 0.04 \text{ at.\%} \qquad (6.21)$$

---

* Based on weight gain and assuming 1 mg $O/cm^2 = 6.3 \mu m$ [43].

It is conceivable that the presence of $NiAl_2O_4$ particles in the inner NiO layer offers a resistance to the outward nickel ions flux and therefore masks the effect of dissolved Al on the scale growth rate. Consequently, the above value for aluminum dissolution in NiO cannot be regarded as conclusive.

A definite conclusion cannot be reached concerning the formation of pores in the intermediate region of the scale. The same phenomenon was observed in $NiAl_2O_4$ formed in diffusion couples of NiO and Al_2O_3 close to its interface with NiO[146]. A possible explanation for the presence of these pores within the scale is the decrease in volume, approximately 6% , accompanying the formation of $NiAl_2O_4$ from its parent oxides.

6.2.4 Conclusions

i) The addition of 2 wt.% Al to Ni results in an increase in the oxidation rate by one order of magnitude and the formation of a duplex scale and an internal precipitation zone in the alloy. The duplex scale consists of an outer Al-doped NiO layer and an inner NiO layer containing $NiAl_2O_4$ as a second phase. The internal precipitates are Al_2O_3. The presence of $NiAl_2O_4$ within the alloy in the vicinity of the alloy/scale interface or unreacted Al_2O_3 in the inner layer could not be ascertained experimentally. The internal precipitates grow most rapidly and the inner layer thickens most slowly.

ii) The internal precipitates grow as rods extending through the precipitation zone approximately parallel to the growth direction and independent of alloy orientation.

iii) Tne growth of the Al_2O_3 internal precipitates, which is interpreted by a solid state displacement reaction between the NiO scale and Al in the alloy, is controlled by oxygen diffusion through the Al-depleted alloy in the precipitation zone.

iv) $NiAl_2O_4$ particles in the inner layer are formed by a solid state reaction between NiO and Al_2O_3 precipitates upon the incorporation of the latter, by plastic deformation, into the NiO scale.

v) A rate controlling step cannot be assigned to the reaction since the three layers grow in a cooperative diffusion mode. However, the increase in the oxidation rate of the Ni-2 wt.% Al alloy in comparison to pure Ni is attributed to the doping effect of aluminum in NiO, being partially masked by the presence of $NiAl_2O_4$ particles in the inner layer, and the high aluminum affinity for oxygen resulting in the internal precipitation of Al_2O_3.

6.3 TRANSITION FROM INTERNAL OXIDATION TO CONTINUOUS SCALE FORMATION

6.3.1 Introduction

The oxidation kinetics for the Ni-6 wt.% Al alloy were irreproducible. Scale topographies revealed that the irreproducibility was associated with the formation and coalescence of NiO nodules distributed in an imperfect Al_2O_3 film. These nodules form preferentially at alloy grain boundaries and their density depends on alloy surface preparation procedures.

The development of the scale morphology during a long transient period to a final steady state configuration consisting of a multi-layered $NiO/NiAl_2O_4/Al_2O_3$ scale was described in Sec. 5.3.1.

6.3.2 The phenomenon of Oxide Nodular Growth

It appears that the formation of nodules is a common phenomenon of alloy oxidation when large differences exist in the diffusion and thermodynamic properties of the oxides. In support of this view, nodules of the less stable and usually less protective oxides were observed at localized regions in films of the more stable and usually more protective oxides formed on Ni-Al[19,20], Ni-Cr[162,163], Co-Cr-Al[164], Fe-Cr[165,166] and Fe-Si [167] alloys. Wood et al [19,166] have ascribed this phenomenon to the mechanical breakdown of the initially formed protective scale. Their model was described in Sec.3.5.2.

In the present investigation, no breakaway kinetics were observed under isothermal conditions during long oxidation periods (up to 50 h). The initial oxygen uptake by this alloy, which is much more rapid than its value when only Al_2O_3 is formed on alloys with higher Al contents[16], suggests that Al_2O_3 does not form initially as a perfect continuous film. It appears that imperfectionsat the alloy surface, e.g. grain boundaries, polishing marks, allow NiO to form as a transient phase. Mechanical abrasion of the specimens actually results in the formation of an almost continuous film. A nodule exhibits a circular base due to istropic lateral

diffusion in the cubic NiO phase. As reactant diffusion in NiO is several orders of magnitude faster than in Al_2O_3 (Table 3-4), the former overgrows the Al_2O_3 film and spreads laterally over it.

6.3.3 Transition to Continuous Scale

Giggins and Pettit[168] have observed that on Ni-Cr alloys, Cr_2O_3 is formed as a continuous film over alloy grain boundaries; whereas it is precipitated internally at other areas. Consequently, they suggested that this phenomenon, caused by enhanced chromium diffusion or preferential nucleation of Cr_2O_3 at alloy grain boundaries, coupled with lateral chromium diffusion between these sites led to the transition from internal to external scale formation. A similar mechanism was suggested in the case of Ni-Al alloys[18,19].

Though preferential precipitation of Al_2O_3 at alloy grain boundaries was observed in this investigation, the precipitates did not form a complete continuous film in these regions, Fig.5-3(b). The initiation of continuous Al_2O_3 film formation, which is indicated by (Δ) in Fig.5-7 and 5-8, occured at random sites within the alloy grains. It was observed that in the region where the Al_2O_3 precipitation front ceased to advance at the same rate as the rest, impingement of the rodlike precipitates had occurred, Fig.6-2(a). Based on this observation, it is suggested that impingements of favorably oriented rods lead to the formation of partially continuous Al_2O_3 film sections which hinder oxygen inward

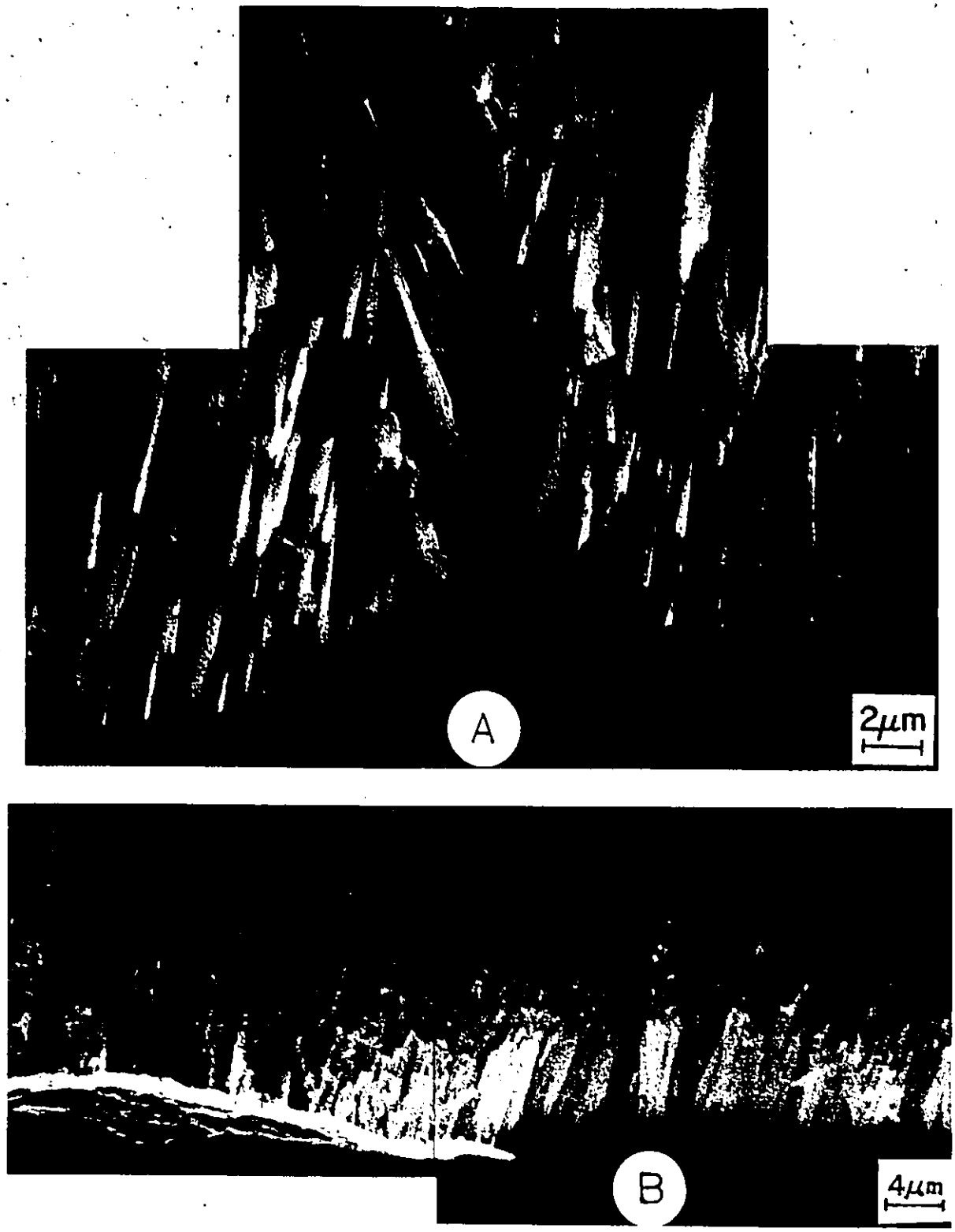

Fig.6-2. Development of Al_2O_3 film at the precipitation front : (a) impingement of rodlike precipitates, (b) lateral growth of discontinuous film.

diffusion in these regions. This process occurs randomly and is favored by the increase in the density of the precipitates accompanying the increase in the alloy aluminum content. The formation of a semi-continuous Al_2O_3 film depletes the aluminum concentration in the vicinity of the alloy/ Al_2O_3 interface. However, oxygen and metal diffusion in Al_2O_3 are several orders of magnitude less than aluminum diffusion in the Ni-Al alloy (Refer to Tables 3-1 and 3-4). This diffusional behavior would be expected to lead to insignificant aluminum depletion from the alloy. In contrast, at the precipitation front, the alloy would be extremely depleted of Al in the vicinity of the precipitates, as discussed in Sec.6.2.2. This latter hypothesis was verified by determining the concentration profile in these two regions using electron probe micro-analysis. The results are presented in Fig.6-3. The Al and Ni X-ray line scans across the reaction zone correspond to regions marked A-A and B-B on the micrograph. It is evident that the alloy is more significantly depleted of Al at the vicinity of the precipitates (line A-A) than in the region where a continuous film was formed (line B-B). This lateral concentration gradient results in Al diffusion in the alloy from beneath the discontinuous film to the neighboring precipitates where it reacts with oxygen moving inward to cause continual lateral growth of the Al_2O_3 film, Fig.6-2(b).

6.3.4 Oxidation Mechanism

Referring to Fig.6-4, the oxidation behavior of the Ni-6 wt.% Al alloy is interpreted as follows :

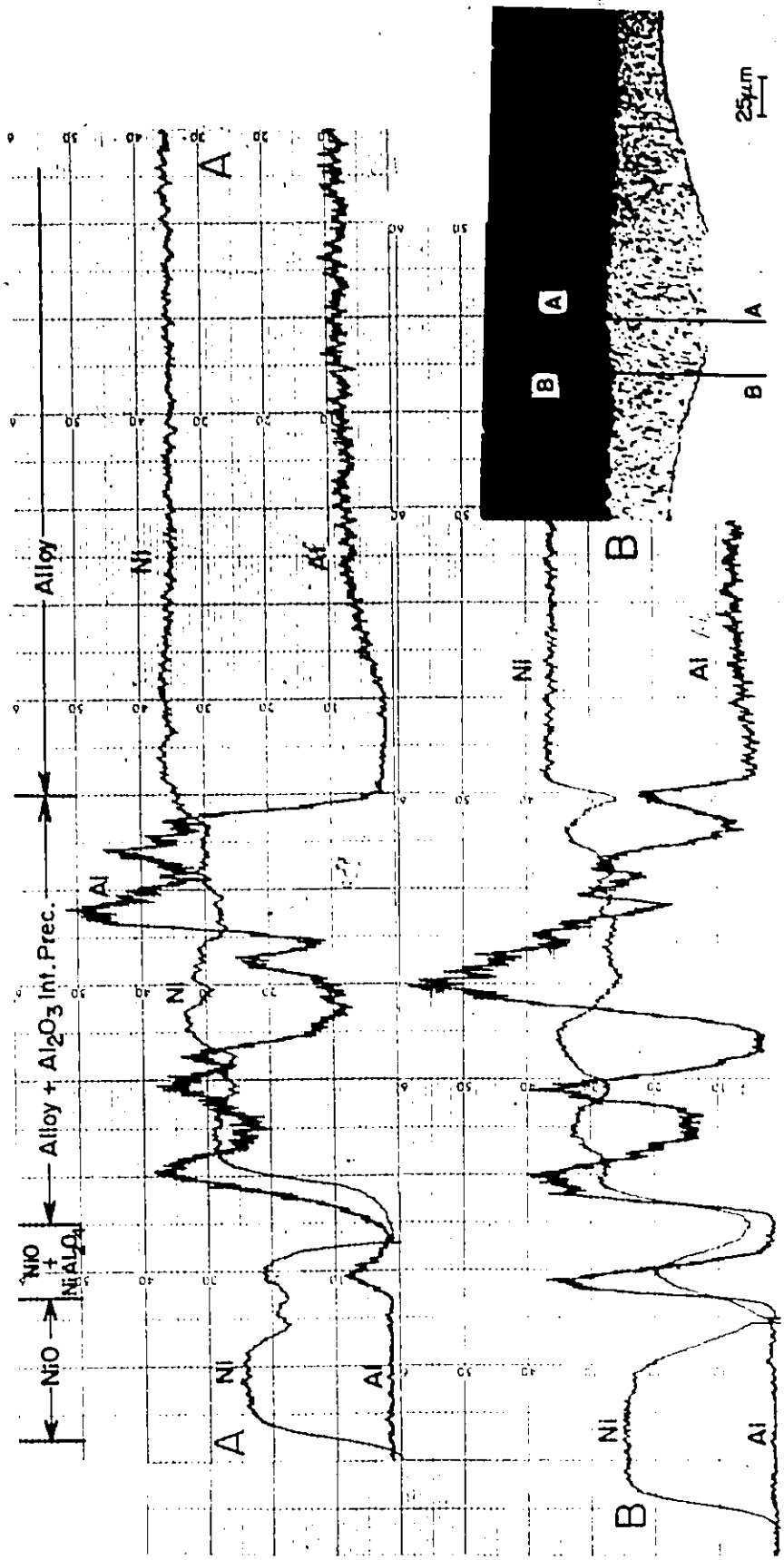

Fig. 6.1. Al and Ni electron microprobe scans across a scale formed on Ni-6 wt.% Al alloy.

i) In the region of nodules or wherever NiO is formed, the scale grows by a mechanism similar to the case of Ni-2 wt.% Al alloy, Fig.(a). At T = 1473 K, the value of the parabolic rate constant during this initial oxidation stage is k_1 = 2.5×10^{-9} $g^2.cm^{-4}.sec^{-1}$. This value, which is the same order of magnitude as that for Ni-2wt.% Al alloy, supports the foregoing conclusion.

ii) At a latter stage , impingement of the rodlike Al_2O_3 precipitates results in the formation of discontinuous more protective film sections at random sites of the precipitation front, Fig.(b). This event leads to the decline in the oxidation kinetics and deviation from parabolic behavior, Fig.5-10.

iii) The complete development of a continuous Al_2O_3 film, which results from Al lateral diffusion from impingement sites to neighboring precipitates, Fig.(c) and (f), coincides with the onset of the second parabolic stage. This highly irregular oxide film isolates the precipitation zone from the alloy substrate. The suppression of the displacement reaction involving the NiO scale and Al in the alloy, which was postulated to account for the growth of the Al_2O_3 precipitates, Sec.6.2.2, results in the decline of the parabolic rate constant by one order of magnitude, k_2 = 0.8×10^{-10} $g^2.cm^{-4}.sec^{-1}$. During this second parabolic stage, the reaction is controlled by outward diffusion of Ni from the Al-depleted alloy in the hindered

precipitation zone through the inner NiO + $NiAl_2O_4$ layer and the outer NiO layer to the scale surface. Plastic deformation of the external scale and the continual incorporation of the Al_2O_3 precipitates in NiO transform these two phases to $NiAl_2O_4$ by counter-current cation diffusion, Fig.(d).

iv) The subsequent decline in the oxidation rate, which is not shown in Fig.5-10, corresponds to the thickening of the innermost Al_2O_3 film and the conversion of the intermediate NiO + $NiAl_2O_4$ layer to a continuous $NiAl_2O_4$ scale by partial dissolution of the Al_2O_3 film, Fig.(e).

6.3.5 Conclusions

i) Addition of 6 wt.% Al to Ni favors the eventual formation of a protective Al_2O_3 film. Structural imperfections at alloy surface allow NiO to form in the early stage of the reaction as nodules beneath which internal precipitation of Al_2O_3 occurs.

ii) The oxidation kinetics are irreproducible and also depend on surface preparation techniques. The irreproducibility is associated with the nodular oxide growth. Tnree distinct reaction stages, nevertheless, can be discerned :

(a) An initial parabolic stage during which NiO and the internal oxidation zone containing Al_2O_3 precipitates grow by a mechanism simflar to the case of the Ni-2 wt•% Al alloy.

(b) A second, but slower, parabolic stage which coincides with the onset of continuous Al_2O_3 film formation at the alloy precipitation front. The decline in the oxidation kinetics is attributed to suppression of the displacement reaction between

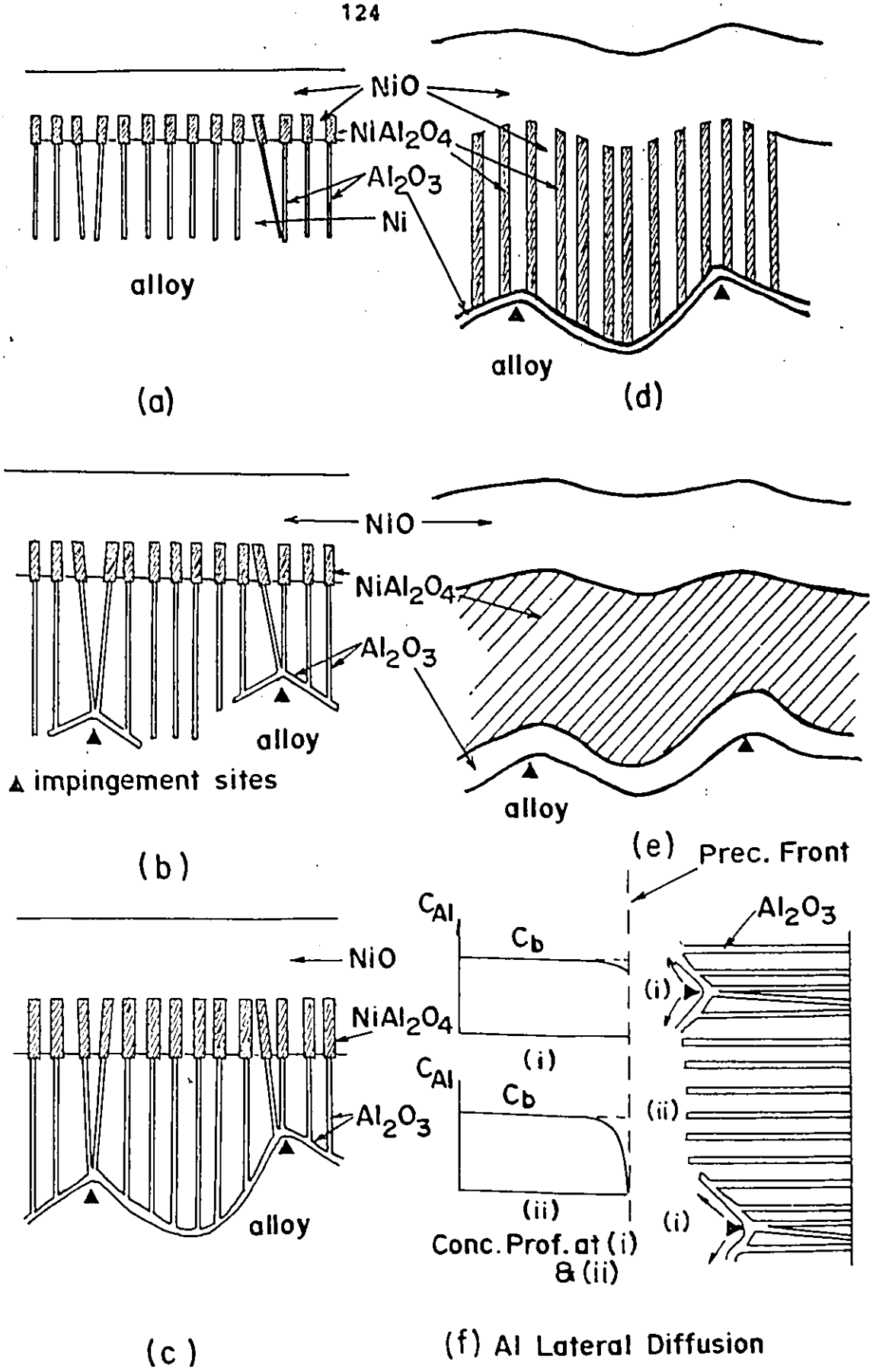

Fig.6-4. Scnematic model for scale growth on Ni-6wt.%Al alloy.

the external NiO scale and Al in the alloy by development of the protective continuous Al_2O_3 film.

(c) A much slower stage controlled by the thickening of the Al_2O_3 film.

iii) It is suggested that the transition from internal precipitation to continuous Al_2O_3 film formation occurs by impingement of favorably oriented rodlike precipitates. These impingements lead to the development of the Al_2O_3 film by lateral diffusion of Al from the impingement sites to react with oxygen at neigboring regions of the precipitation front.

6.4 GROWTH OF THE PROTECTIVE Al_2O_3 SCALE

6.4.1 Introduction

Al_2O_3, which is the sole oxide phase formed on the Ni-32 wt.% Al alloy, grows as a protective film. The following common features are associated with the growth of this Al_2O_3 film on Ni-Al alloys[*,19-22] and alloys containing Al other than Ni-Al[23-29]:

i) The growth kinetics are those of a barrier type film characterized by an initial relatively large weight gain (or high thickening rate) followed by an asymptotic approach towards a very slow scale growth rate[*,19,23-25,26,28]. There is no agreement on the kinetic relationship governing the growth of Al_2O_3, Sec.3.5.3. In the present study, to avoid errors caused by oxidative vaporization of platinum suspension wires, Sec.4.3, the kinetics were determined by layer thickness measurements. These results indicate that the Al_2O_3 scale does not thicken parabolically but rather at a rate which

* This study.

decreases with time, Fig.5-15. Similar results have been obtained in other studies[25,26].

ii) The morphological development of the scale may be summarized as follows :

(a) Formation of an initial sub-microcrystalline oxide film[*,22].

(b) "Recrystallization" of the oxide film[*].

(c) Subsequent growth gives rise to a cellular scale[*,22,29] which has ridges extending inward and outward[*,22,29,158].

(d) Formation of cavities at the alloy/oxide interface[*,19, 21-28].

(e) Growth of oxide filaments (whiskers) at the Al_2O_3 scale/gas interface[*,21,23,28].

iii) Thick scales spall upon cooling. In this respect, it was found that scale adherence is improved by minor additions of reactive elements,e.g. Y, Th, Sc, Hf,[21,23-25,27,28].

The results pertinent to the growth of the Al_2O_3 film and scale, which were obtained in this study, are discussed in the following sub-sections.

6.4.2 Structural Development of the Al_2O_3 Film and Scale

The electron diffraction measurements, which were presented in Sec.5.4.1, demonstrated that an initial sub-microcrystalline film is formed on the Ni-32 wt.% Al alloy even at temperatures as high as 1473 K. Auger electron spectroscopy (AES) revealed that it consists of Al_2O_3 only. Heating the stripped film in the electron microscope caused "recrystallization" to γ-Al_2O_3 rather than α-Al_2O_3. This transformation

was observable at 1073 K under the conditions of rapid heating. It is therefore conceivable that the sub-microcrystalline oxide films formed under isothermal conditions at temperatures exceeding 1273 K , which transform to α-Al_2O_3 during their growth, involve the transient formation of γ-Al_2O_3 phase. If this transformation does occur, it could possibly lead to the occurence of faulty regions in the recrystallized film since the conversion of γ-Al_2O_3 to α-Al_2O_3 is accompanied by a reduction of 14.3% in volume[133].

The recrystallized α-Al_2O_3 film is non uniform and exhibits ridges extending inward and outward which implies that these ridges contain a large density of boundaries which act as easy diffusion paths for the reactants. The presence of these active boundaries within the polycrystalline oxide ridges between the well oriented thinner oxide film regions, Fig.5-12, could be induced by faulty regions, as discussed above or the influence of the alloy substructure.

Attempts were made to determine if a correlation exists between the alloy substructure and structure of the α-Al_2O_3 film. The results obtained using X-ray Berg/Barrett topography technique[155], were presented in Sec.5.4.2. The contrast present in the X-ray topographs, Fig.5-14, can arise from either a variation in lattice parameter due to compositional difference or misorientation between alloy sub-grains. Electron probe micro-analysis (EPMA) indicated no compositional difference in an oxidized specimen in the region of the alloy/oxide interface. Furthermore, AES analysis, using a 200 nm electron

beam, of an ion sputter-cleaned region of the alloy surface from which the Al_2O_3 scale has spalled, assured the above finding[155]. In view that diffusion in β-NiAl is several orders of magnitude greater than in Al_2O_3 (Table 3-1 and 3-4), selective oxidation of Al does not lead to a significant compositional gradient in the alloy. Accordingly, the contrast in the X-ray topographs is due to misorientation of alloy sub-grains. Therefore, the white areas in these images correspond to sub-grains which are exactly oriented for Bragg diffraction whereas dark areas portray improperly oriented sub-grains. Thence, the transition from a dark to white region indicates the presence of a sub-boundary. A comparison of the oxide film SEM image, Fig.(a), to the X-ray topographs, Fig.(b) and (c), indicates that there is not a one-to-one correspondence between the alloy sub-boundary density and oxide ridge density. The size of the alloy sub-grains is much larger than the size of the oxide grains between ridges. There is,notwithstanding, a qualitative relation between these two parameters : a large sub-boundary density in alloy grain A corresponds to a large oxide ridge density. The same observation applies for grain B which has fewer sub-boundaries.

It is plausible that the sub-structure of the alloy surface is different from the bulk and that the former determines the structure of the recrystallized film. Since the sensitivity of the X-ray topography technique with respect to depth is in the order of 100μm, the surface sub-structure would not be revealed. Furthermore, it is anticipated that

the original alloy sub-grains, which determine the structure of the oxide film, recrystallize and grow and even become consumed as thick Al_2O_3 films are formed. Accordingly, based on the X-ray topography measurements, one cannot draw a definite conclusion with respect to the existence of a correlation between alloy substructure and film structure.

The origin of the cavities at the alloy/Al_2O_3 scale interface, which were also observed by other investigators [19,21-28,89] in Al_2O_3 forming alloys, cannot be unequivocally defined. Similar pores or cavities were observed in oxidized Ni[169] and Fe-Cr alloys[170,171]. It is established that NiO and $(Fe,Cr)_2O_3$, which form on these alloys, respectively, grow by outward cation diffusion. Consequently, it was speculated[169-172] that in the presence of few vacancy sinks, as in the case of coarse-grained alloys or foils with large surface/volume ratio, the concentration of the vacancies injected to the metal exceeds the supersaturation limit leading to void formation by vacancy coalescence. Another possible source of vacancies is the Kirkendall effect resulting from a faster backward diffusion of the noble metal to the alloy bulk than the forward diffusion of the metal being selectively oxidized to the reaction front[21,24].

Transport of the reactive elements across the voids can occur by evaporation from the alloy substrate[25,170]. In the following derivation, this latter hypothesis is verified. The aluminum evaporation rate from the Ni-Al substrate is given by :

$$\frac{dW}{dt} = \{ P_{Al} \left(\frac{M}{2\pi RT}\right)^{\frac{1}{2}} \} \qquad (6.22)$$

In this calculation, the effect of void curvature in not taken

into consideration. At T = 1473 K, $P^{o}_{Al} = 10^{-5}$ atm [173], $a_{Al} = 10^{-3}$ [90]. Substituting these values in Eq.(6.22), the aluminum evaporation rate $\simeq 0.2\times10^{-8}$ g.cm^{-2}.sec^{-1} which is equivalent to 1.7×10^{-7} g O.cm^{-2}.sec^{-1}. The latter value is much greater than the maximum observed oxygen uptake rate by the specimen equal to 0.1×10^{-8} g O.cm^{-2}.sec^{-1}. This aluminum evaporative mechanism leads to the conclusion that void formation does not interfere with scale growth and explains the growth of relatively uniform thick scales in the presence of cavities, Fig.5-13(a). Aluminum evaporation from the substrate leads to the observed spiral steps, faceting and enlargement of voids, Fig.5-13 {(d) and (e)}. Void formation, however, has a detrimental effect on the mechanical properties of the alloy/scale system since they concentrate stresses arising from differential thermal contraction during cooling which leads to scale spalling [21].

6.4.3 Aluminum and Oxygen Mobility in Al_2O_3 Films and Scales

The results of the inert marker measurements, which were performed on the initial sub-microcrystalline Al_2O_3 film formed on Ni-32 wt.% Al, were presented in Sec.5.4.4. Since the palladium marker resided at the film gas interface, this film grew by inward oxygen diffusion. This method was also used to study the growth of γ-Al_2O_3 and NiO on Al and Ni, respectively. The results are included in Appendix B to demonstrate the validity of this technique.

Since the thicker recrystallized α-Al_2O_3 films were

not uniform and inevitably spalled upon cooling, it was not possible to use this technique to establish their growth mechanism. Nevertheless, based on metallographic observations, previous investigators have drawn some conclusions concerning the growth of α-Al_2O_3 scales on aluminum-containing alloys other than NiAl. The persistent appearance of polishing scratches at the scale surface was taken as an indication that oxygen is the most mobile species in the lattice; whereas, the growth of oxide ridges was taken as evidence that grain boundaries are short-circuit paths for both species[29]. However, most investigators believe that α-Al_2O_3 growth is controlled by oxygen diffusion along grain boundaries present in the scale[21-28]. The last conclusion is supported by the following observations :

- Inert platinum markers reside at the scale outer surface[23]. The diameter of the wires used (10-20 μm) should be compared with scale thickness (approximately 5 μm). This experiment was carried out on FeCrAlY alloy since scales formed on Y-free alloys spall readily upon cooling.

- Reactive metals, which are slightly soluble in Fe, Ni and Co base alloys (e.g. Y, Hf, Sc, Th, etc) segregate at alloy grain boundaries and form thick oxide stringers 10 to 20 μm long which extend through the scale and become incorporated in it after very long time[25,27,28]. Y and Th form large particles (10∿25 μm) which protrude from spalled areas at the alloy surface[21,24].

- Alloy grain boundaries extend into the scale in the

case of Y-doped alloys[23].

- Preferential inward scale thickening in the vicinity of grain boundaries[26].

- Variation of grain size across the scale[28], as discussed in Sec.3.5.3.

These observations, however, are not definitive for establishing the diffusion mechanism for oxide layer growth. Thick inert wire markers may interfere with scale growth[174]. Results obtained using reactive markers are difficult to interpret since the large size and irregular shape of these precipitates do not allow accurate determination of their location in the reaction zone*. In addition to modifying the defect and grain structures of the Al_2O_3 scale, the presence of theses elements may affect its stability by depleting the aluminum alloy content in localized regions to the extent that other less stable oxides are formed[21] or that Al_2O_3 is initially precipitated internally. The encapsulation of thick oxide stringers of the reactive elements by a thin Al_2O_3 film giving rise to a highly irregular morphology[25,28], which is similar to that observed in this study during the transition from internal oxidation to continuous scale formation, would support the latter assumption.

In the present investigation, the viewpoint is adopted that both aluminum and oxygen migration in the α-Al_2O_3 scales play a role in the oxidation mechanism. The formation of oxide ridges extending inward in the vicinity of grain boundaries,

---

* See Ref.(21),(24),(25),(27) and (28).

Fig.5-12(c) and 5-13(c), is taken as taken as evidence that oxygen inward migration is mainly limited to grain boundaries in the scale. Moreover, the following metallographic observations suggest outward aluminum diffusion in the Al_2O_3 grains and along grain boundaries :

i) Formation of ridges extending outward in the region of grain boundaries[*,22,29], Fig.5-12(a) and(c) and Fig.5-13 (b) A similar morphology was observed in NiO scales[121] which grow by predominant nickel diffusion.

ii) The ridge spacing at the scale/gas interface is usually less than at the scale/alloy interface, Fig.5-13(b) and (c). This observation is consistent with scale growth at the scale/gas interface if nucleation of new grains and their subsequent growth are taken into consideration.

iii) Growth of whiskers at the Al_2O_3 scale/gas interface[*,21,23,28], Fig.5-13(b). Plastic deformation was suggested to cause needle or whisker growth on oxidized metals wherein oxygen is expected to be the mobile specie in the oxide[175]. It is evident that the oxide must be extremely ductile to undergo such deformation. Rather than adopting this point of view, the mechanism advanced by previous investigators[59-61], which is based upon metal transport through the oxide by a type of line or surface defect, is believed to apply.

iv) In the previous section, it was demonstrated that the equivalent aluminum evaporation rate from the alloy substrate

---

* This study.

is one order of magnitude larger than the maximum oxygen uptake rate. Under these circumstances, bulk oxygen diffusion would result in the formation of oxide crystallites which would fill the cavities. This condition was not observed; instead, the cavity volume increased with time, Fig.5-12(c) and 5-13(d).

The relative contribution of oxygen diffusion to scale growth is determined by the density of grain boundaries present in it. Oxygen boundary diffusion was shown to play the major role in the growth of the sub-microcrystalline film. Hence, thickening of the recrystallized α-Al_2O_3 film would be controlled by oxygen inward migration along the fewer grain boundaries in the scale in conjunction with outward aluminum migration through grain boundaries and grain bulk. The transport properties of α-Al_2O_3 were discussed in Sec.3.4.3. The measurements of tracer diffusivities[55,56] demonstrated that aluminum diffuses approximately at a rate one order of magnitude higher than oxygen in polycrystalline Al_2O_3. Oxygen diffusion in single crystal Al_2O_3 compared to the above aluminum diffusion rate is about two orders of magnitude less. One is therefore led to the conclusion that the highly oriented Al_2O_3 grains between the oxide ridges grow mainly by aluminum lattice diffusion outward to react with oxygen at the external scale surface. Moreover, this rate of aluminum diffusion would be enhanced by the doping effect of Ni on Al_2O_3 since thick scales contained 0.5 wt.% Ni. The most recent electrical conductivity measurements on nigh purity Al_2O_3 single crystal by Kröger et al[142] are consistent with the point defect model with

Al interstitial ions and electrons as the major mobile species. Accordingly, the defect equation can be written as :

$$Al_2O_3 = 2\,Al_i^{3\cdot} + 3/2\,O_2 + 6\,e' \qquad (6.23)$$

The doping of Al_2O_3 by Ni results in the increase of interstitial aluminum ions concentration according to the following reaction :

$$NiO = Ni'_{Al} + Al_i^{3\cdot} + 1/2\,O_2 + 2\,e' \qquad (6.24)$$

Consequently, the scale between the oxide ridges would grow by this enhanced aluminum outward lattice and lateral boundary diffusion to lead to the development of the observed relatively uniform thick scales, Fig.5-13(a).

6.4.4 Al_2O_3 Scale Growth Model

In this section, a model, which is illustrated in Fig.6.5, is advanced for the growth of Al_2O_3 scale on Ni-32wt.% Al alloy. Initially,a sub-microcrystalline Al_2O_3 film is formed. This film contains a large density of boundaries along which oxygen diffuses inward resulting in even and relatively rapid thickening, Fig.(a). Film "recrystallization",by nucleation of epitaxed crystallites and their lateral growth, leads to the development of a well oriented α-Al_2O_3 film containing regions of disarrayed oxide, Fig.(b). The latter could be induced by faulty regions within the recrystallized film or the influence of alloy sub-structure. The presence of reactive diffusion boundaries in this disarrayed oxide results in the development of ridges extending inward and outward by countercurrent diffusion of oxygen and aluminum, respectively, Fig.(c). Based on the recent electrical conductivity measurements[142],

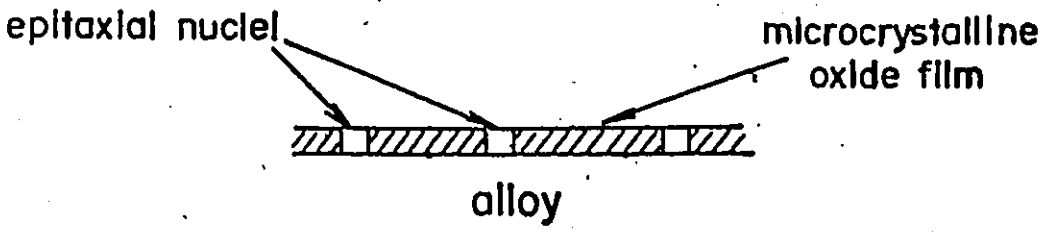

(a)

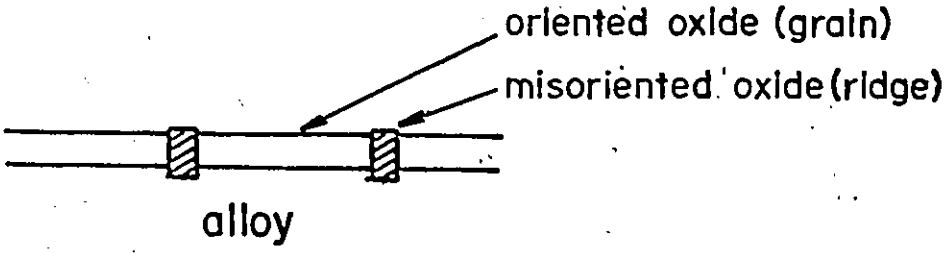

(b)

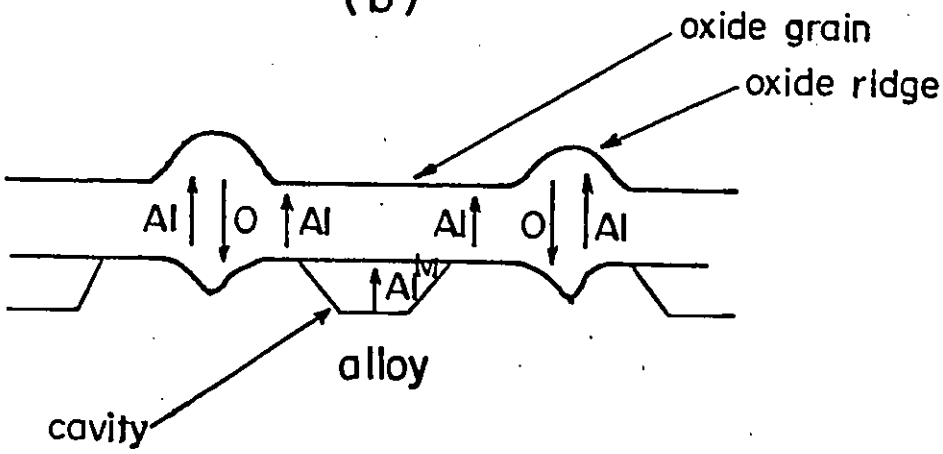

(c)

Fig.6-5. Schematic model for Al_2O_3 scale growth on Ni-32 wt.% Al alloy.

it is assumed that the film bulk grows by outward migration of aluminum ions via an interstitial mechanism. Voids are formed at the alloy/Al_2O_3 interface by coalescence of vacancies generated by film growth. Aluminum evaporation from the substrate leads to the development of faceted cavities. Eventually, aluminum lateral diffusion through the boundaries present in oxide ridges coupled with its enhanced outward diffusion through the film,due to nickel doping, results in uniform thickening of the scale.

In the following, the oxidation kinetics for the growth of the recrystallized α-Al_2O_3 scale are interpreted by a short-circuit diffusion model. This latter type of model was advanced by Perrow and co-workers[43-45] to interpret the growth of NiO films on Ni. The effective diffusion coefficient for oxygen and aluminum migration along grain boundaries and aluminum along lattice sites can be expressed by :

$$D_{eff} = (1-f)\, D_L + f\, \bar{D}_B \approx D_L + f\, \bar{D}_B \qquad (2.7)$$

where D_L is the aluminum lattice diffusion coefficient,

$\bar{D}_B$ is an average diffusion coefficient for counter-current migration of aluminum and oxygen along grain boundaries,

f is the fraction of grain boundary sites.

Based on this formula and the derivation outlined in Sec.2.4, it can be shown that :

$$x^2 = 2\, \tilde{V}\, \Delta C\, D_L \int dt + 2\, \tilde{V}\, \Delta_C\, \bar{D}_B \int f\, dt \qquad (6.25)$$

$$x^2 = K_L\, t + K_B \int f\, dt \qquad (6.26)$$

Upon substituting f from Eq.(2.12) and the observed grain growth relationship, Eq.(2.11), and integrating, one obtains :

$$x^2 = K_L t + K_B \frac{4d}{k'} (D - D_o) \qquad (6.27)$$

Redifferentiating,

$$\frac{dx^2}{dt} = K_L + 2 K_B d (D)^{-1} \qquad (6.28)$$

The plot of $\frac{dx^2}{dt}$ versus $(D)^{-1}$, Fig.6-6, which yields a straight line, demonstrates that the above relation is valid. The slope of this line is $2 K_B d$. Assuming an Arrhenius relation $K_B = K_B^o \exp(-E_B/RT)$ and the independence of boundary width on temperature, the calculated value of the activation energy for aluminum and oxygen boundary diffusion is 128 kJ/g mole. The agreement between the value obtained from this model and the activation energy for grain growth, E_G = 133 kJ/ g mole,(Sec. 5.4.3) supports the conclusion that grain boundary diffusion is involved in scale growth.

An additional test for the model was made by calculating the scale grain size after incremental oxidation periods. Since $K_B >> K_L$, Eq.(6.28) is reduced to :

$$\frac{dx^2}{dt} \alpha (D)^{-1} \qquad (6.29)$$

Using the kinetic data and knowing the average grain size at a given time, the scale grain growth rate can be predicted. The calculated and measured grain size are given in Table6-1. This reasonable agreement between the observed and calculated values, within the limitation of the experimental accuracy of the kinetic and grain growth data, provides an additional

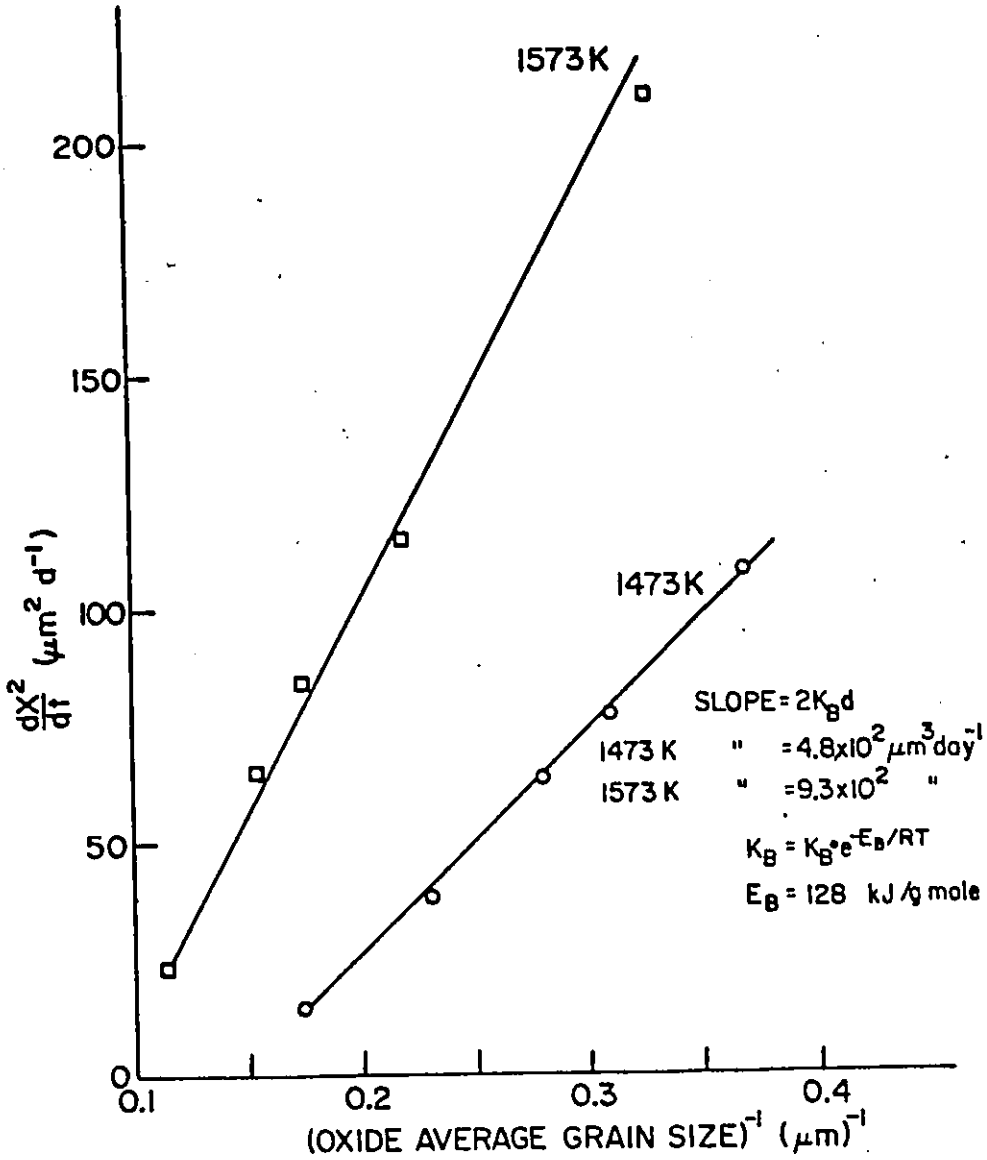

Fig.6-6. Verification of short-circuit model : Plot of $\frac{dX^2}{dt}$ versus D^{-1}.

support for the applicability of the short-circuit diffusion model.

Table 6-1

Comparison of Observed and Calculated Oxide Grain Size

Oxidation Time (d)	Average Oxide Grain Size (μm) Observed	Calculated
2	3.2 ±0.6	3.8
3	3.6 ±0.8	4.7
5	4.5 ±0.6	6.8

6.4.5 Conclusions

i) Only Al_2O_3 is formed on the Ni-32 wt.% Al alloy and it grows as a protective film. The initial Ni-free sub-microcrystalline film thickens evenly. The recrystallized α-Al_2O_3 film is non uniform and exhibits ridges extending inward and outward. Thick scales have a cellular structure and contain 0.5 wt.% Ni in solution.

ii) It was not possible to establish if the structure of the recrystallized Al_2O_3 film was related to the alloy substructure, using the X-ray Berg/Barrett technique, or to the presence of faulty regions in the film induced by recrystallization. The disarrayed oxide (ridge) in the recrystallized film contains a large density of boundaries which are responsible for the relatively rapid growth of the film in these regions.

iii) The marker measurements demonstrated that the submicrocrystalline Al_2O_3 films grow by inward oxygen diffusion. The large density of boundaries in these films results in relatively rapid growth and uniform thickening. The metallographic observations on the growth of the recrystallized α-Al_2O_3 scale are consistent with counter-current aluminum and oxygen boundary diffusion in the disarrayed polycrystalline oxide (ridge) and outward aluminum lattice diffusion in the well oriented thinner film.

iv) The origin of the cavities observed at the alloy/Al_2O_3 scale interface cannot be unequivocally defined. Nevertheless, it was demonstrated that they do not interfere with scale growth since the aluminum evaporation rate from the substrate is much larger than the maximum observed oxygen uptake rate.

v) The average oxide grain size of the scale follows the relation $D^2 = D_0^2 + k' t$, with an activation energy equal to 133 kJ/g mole.

vi) The growth kinetics of the recrystallized α-Al_2O_3 do not follow a parabolic relation. These kinetics can be interpreted using a short-circuit diffusion model which involves both lattice and grain boundary diffusion, as described above. According to this model, the activation energy for aluminum and oxygen boundary diffusion is 128 kJ/g mole.

6.5 APPLICATION OF THE DIFFUSION PATH CONCEPT

In this section, the concept of the diffusion path is used to interpret the observed steady state morphologies of scales formed on the different alloys (Sec.5-2 to 5-4). To date, the Ni-Al-O phase diagram has not been published. However, a study is in progress in this laboratory [159] to determine the compositions of oxide and alloy phases coexisting in equilibrium. The phase diagram shown in Fig.6-7 is based on the results of this study. The proposed virtual diffusion paths corresponding to the scale morphologies observed in the present investigation are shown on the diagram. Paths $A_1B_1C_1D_1E_1F_1G_1H_1I_1$, $A_2B_2C_2D_2E_2F_2G_2H_2$ and $A_3B_3C_3D_3$ correspond to the scale morphologies observed on Ni-2, Ni-6 and Ni-32 wt.% Al alloys, respectively.

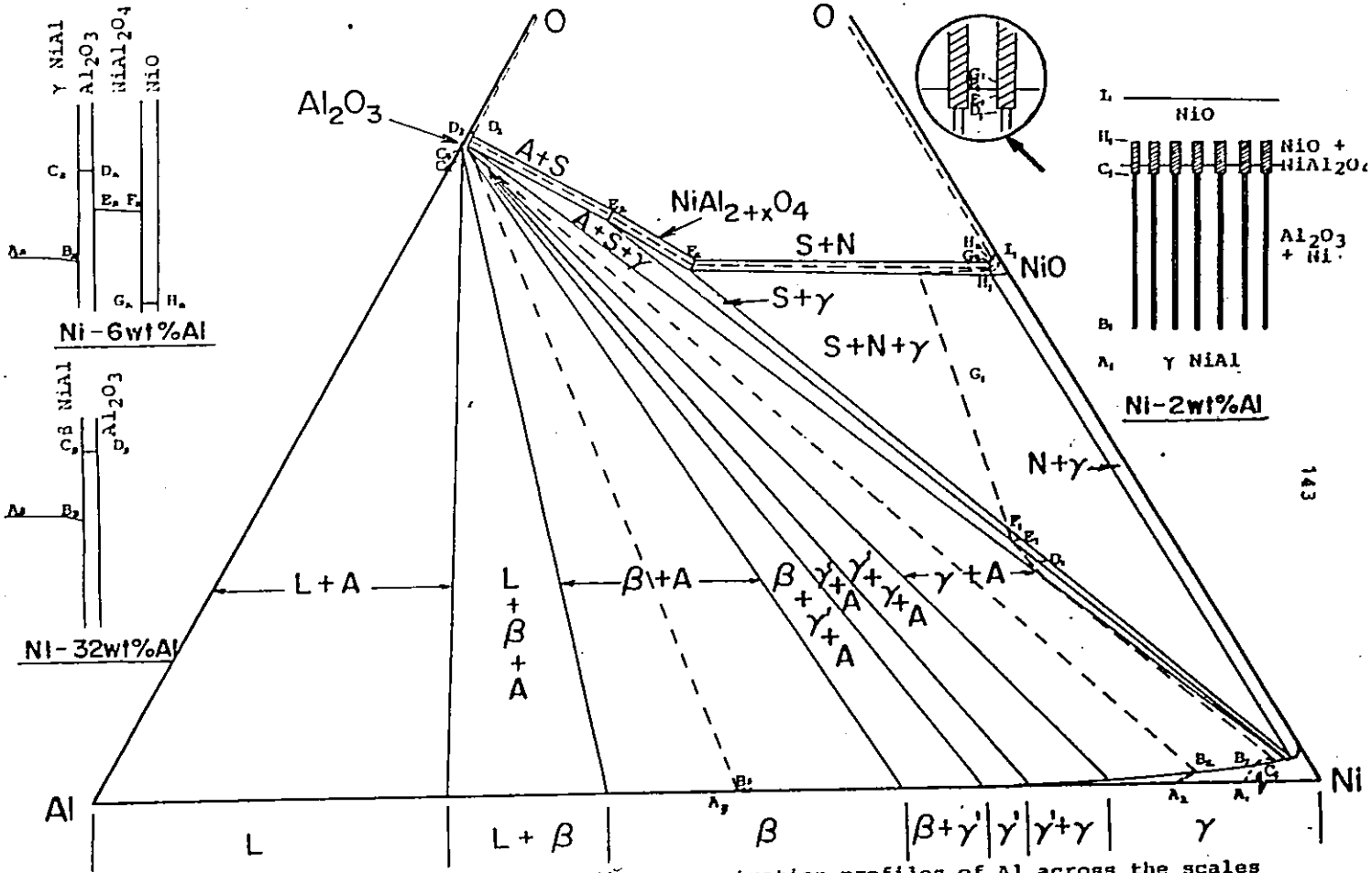

Fig.6-7. Diffusion paths and corresponding concentration profiles of Al across the scales formed on the different alloy compositions. Paths are denoted by 1, 2 and 3 for Ni-2, Ni-6 and Ni-32 wt.% Al alloys, respectively. A=Al_2O_3, N=NiO, S=$NiAl_2O_4$.

CHAPTER 7

SUMMARY

The oxidation properties of Ni-Al alloys, with special interest in the microstructures and growth kinetics of Al_2O_3 formed on them, were investigated in one atmosphere oxygen and at the temperature range 1273-1573 K.

At low aluminum concentration (<4 wt.%), Al_2O_3 is precipitated internally in the alloy and grows as rods extending through the precipitation zone parallel to the growth direction and independent of alloy grain orientation. It was demonstrated that the growth of these precipitates occurs by a solid state displacement reaction between an external NiO scale and Al in the alloy and is controlled by oxygen diffusion through the precipitation Al-depleted alloy zone to the inner reaction front. Solid state reaction between NiO and Al_2O_3 precipitates results in the partial conversion of the inner part of the external scale to $NiAl_2O_4$.

The increase in the oxidation kinetics of dilute Al-Ni alloys relative to pure Ni, which is approximately one order of magnitude, was ascribed to the doping effect of dissolved Al in NiO and the formation of the internal Al_2O_3 precipitates.

At intermediate aluminum alloy concentration (6 wt.%), the initially formed Al_2O_3 precipitates are subsequently transformed to a continuous Al_2O_3 film underlying $NiAl_2O_4$

and NiO layers. It was demonstrated that the transition from internal precipitation to continuous Al_2O_3 film formation is initiated by impingement of favorably oriented rodlike precipitates. Lateral aluminum diffusion from the impingement sites to react with oxygen at neighboring regions of the precipitation front leads to the development of a continuous Al_2O_3 film.

The irreproducibility of oxidation kinetics of this alloy composition during the transient stage and its sensitivity to surface preparation techniques are associated with NiO nodular growth at imperfect sites on the alloy surface, e.g. grain boundaries. However, the steady state oxidation stage is controlled by the thickening of the Al_2O_3 film.

Only Al_2O_3 is formed on Ni-32 wt.% Al alloy (β-NiAl) and grows as a continuous film from the onset of the reaction. However, the initial sub-microcrystalline film subsequently "recrystallizes" to α-Al_2O_3 giving rise to a well oriented film containing regions of disarrayed polycrystalline oxide. It was not possible to establish that the structure of this recrystallized film depended on alloy sub-structure or the presence of faulty regions in the film induced by recrystallization.

Inert marker measurements, using Auger electron spectroscopy in combination with ion sputtering to determine the location of 3-5 nm thick vapor-deposited palladium in the reaction zone, indicate that the initial sub-microcrystalline film grows by inward oxygen diffusion. The metallographic observations on the growth of the recrystallized α-Al_2O_3 scale are consistent with counter-current aluminum and oxygen boundary diffusion in the

disarrayed polycrystalline oxide and outward aluminum lattice diffusion in the well oriented thinner film .

It was proved that the cavities at the alloy/scale interface, which presumably result from coalescence of vacancies generated by film growth, do not interfere with the growth mechanism since aluminum can be transported by evaporation from the alloy substrate across the cavities at a sufficient sustaining rate. The α-Al_2O_3 growth kinetics can be interpreted by a short-circuit diffusion model involving simultaneous reactant lattice and boundary diffusion as described above.

CHAPTER 8

RECOMMENDATIONS FOR FUTURE WORK

1) The study of the Al_2O_3 internal precipitates growth and their transition to a continuous scale was complicated by the presence of other phases (NiO and $NiAl_2O_4$). The use of a controlled atmosphere (CO/CO_2), in which only Al_2O_3 would be thermodynamically stable, would render this task easier.

2) Scale adherence was improved by the "pinning" effect of the rodlike structure of the Al_2O_3 precipitates. This finding suggests that the improved scale adherence of Al_2O_3 scales on the intermetallic nickel aluminide coatings, upon the addition of small amounts of reactive metals such as Y, Th, Hf, etc, occurs by a similar mechanism. However, this phenomenon is not yet fully understood and requires further study.

3) Application of the short-circuit diffusion model to Al_2O_3 films formed on the different faces of β-NiAl single crystal.

4) In this work, a new method, which is based on AES and an inert metal marker was developed to determine metal and oxygen transport in oxide films on metals. However, uneven sputtering of the oxide and metal phases imposed limitations on the precise location of the marker in the reaction zone in the case of oxide films growing by predominant cation diffusion.

In order to avoid this problem, Rutherford ion back-scattering (RBS), which is a non destructive technique, would be more useful in establishing the exact location of the marker. The use of secondary ion mass spectroscopy (SIMS) to determine the distribution of O^{18} in a film grown in O^{16} would permit a quantitative assesment of oxygen diffusivity.

APPENDIX A

RESULTS OF NiO/Ni-2wt.%Al Alloy REACTION COUPLE

In Sec.6.2.2, it was postulated that the growth of the Al_2O_3 rodlike precipitates in Ni-2wt.% Al alloy occurs by a solid state displacement reaction between the external NiO scale and Al in the alloy. In order to support this mechanism, the following experiment was carried out.

A diffusion couple, which was prepared by embedding a Ni-2wt.% Al alloy specimen in compacted NiO powder, was heated to 1373 K in an oxygen-gettered argon atmosphere for 30 h. The reacted couple is shown in Fig.1. It is evident that the internal Al_2O_3 precipitates do form under such conditions. The growth rate of the precipitation zone is also comparable to that observed in a direct oxidation experiment (Sec.5.2).

Solid state displacement reactions occuring in several metal/oxide diffusion couples have been studied by Rapp and co-workers[176]. A Cu_2O/Fe couple resulted in the growth of a Cu+FeO precipitation zone having a morphology similar to that observed in this investigation.

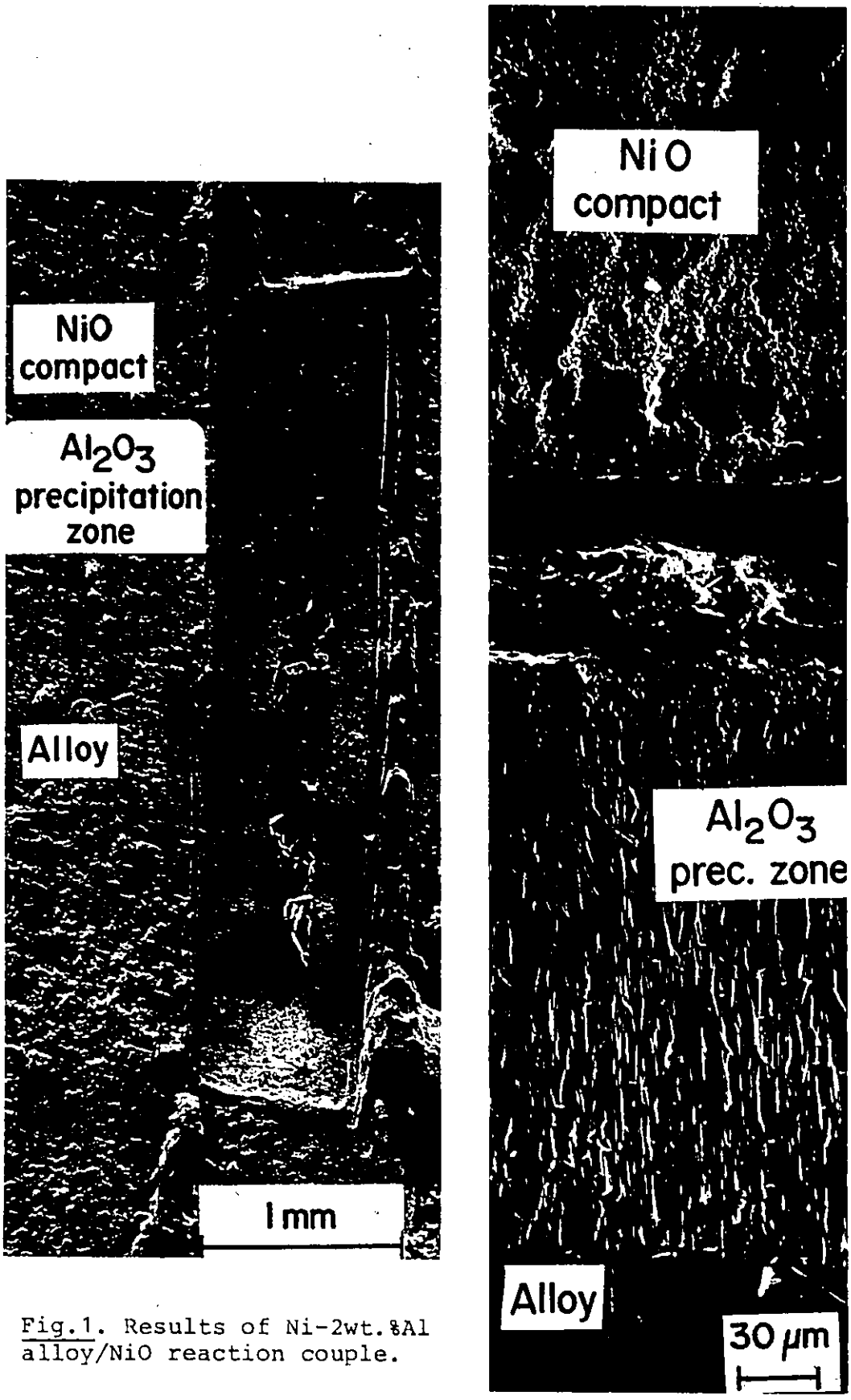

Fig.1. Results of Ni-2wt.%Al alloy/NiO reaction couple.

APPENDIX B

APPLICATION OF AUGER ELECTRON SPECTROSCOPY AND INERT METAL MARKER TECHNIQUES TO DETERMINE METAL AND OXYGEN TRANSPORT IN OXIDE FILMS ON METALS

AES in combination with depth profiling by Ar ion sputtering was employed as a surface analytical technique to determine the location of thin inert palladium markers during growth of oxide films on Al and Ni. The experimental procedure was described in Sec.4.2.4.

Al_2O_3 Film on Aluminum

A transmission electron image and diffraction pattern of the 35 nm thick oxide film formed on Al in 15 h at 853 K are shown in Fig.1. The film is composed of the γ-allotropic phase of Al_2O_3 having the spinel structure. The average oxide grain size is ∿ 150 nm. Auger electron spectra of the oxidized specimens prior to and after sputtering and the film constituents obtained upon depth profiling by sputtering are shown in Fig.2. Steady state compositional profiles were obtained after sputtering for a few minutes. It is evident that the palladium marker resides at the external film surface (oxide/gas interface) and that it is sputtered completely away within 10 min. This observation supports the conclusion that the γ-Al_2O_3 grows by inward oxygen diffusion in accord with conclusions previously drawn from an electron metallographic study by Doherty and Davis[130] who concluded that at T = 873 K, γ-Al_2O_3 crystallites nucleate and grow inward beneath an

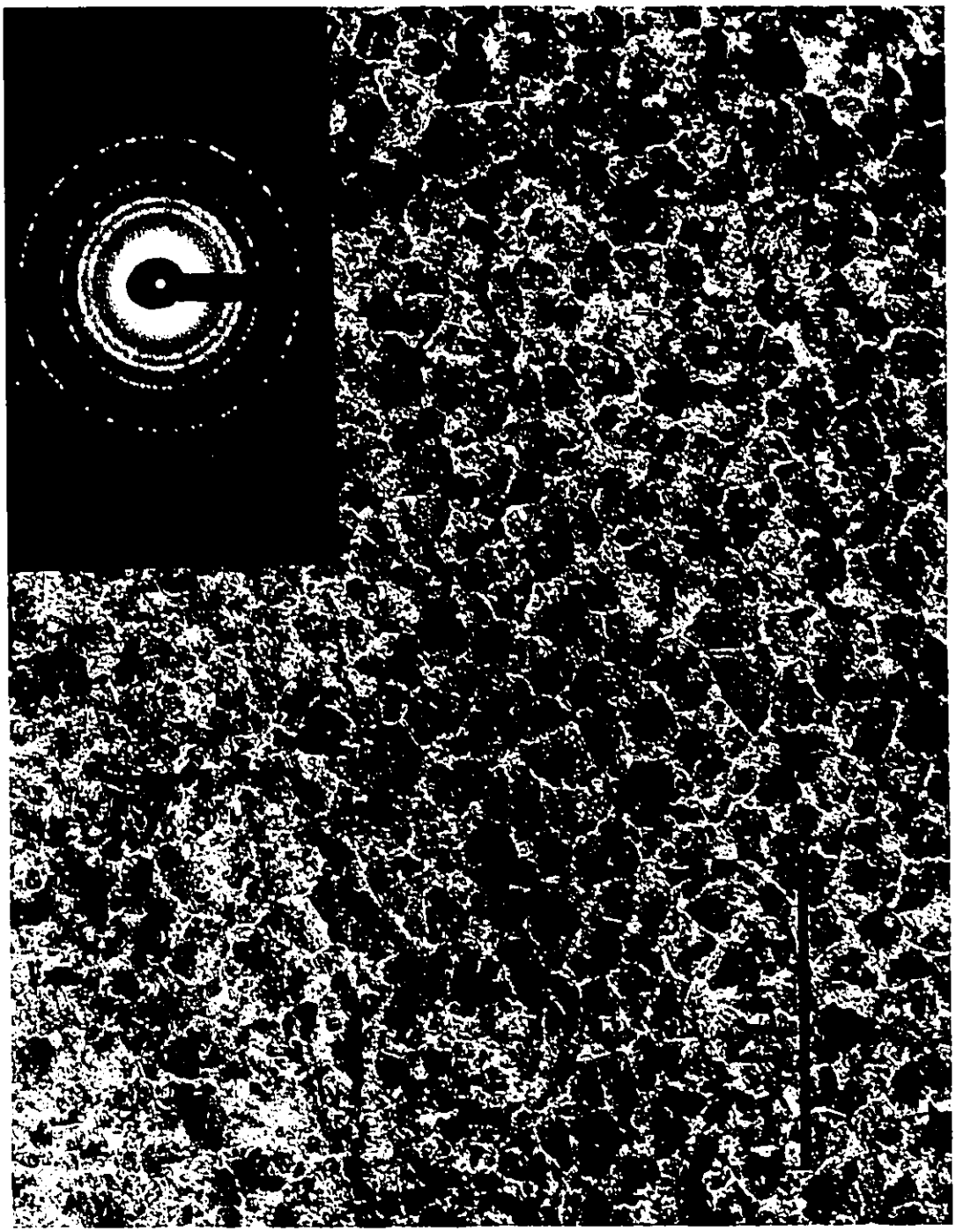

Fig. 1. Transmission electron image and selected area diffraction pattern of an Al_2O_3 film formed on Al in 15h at 853 K.

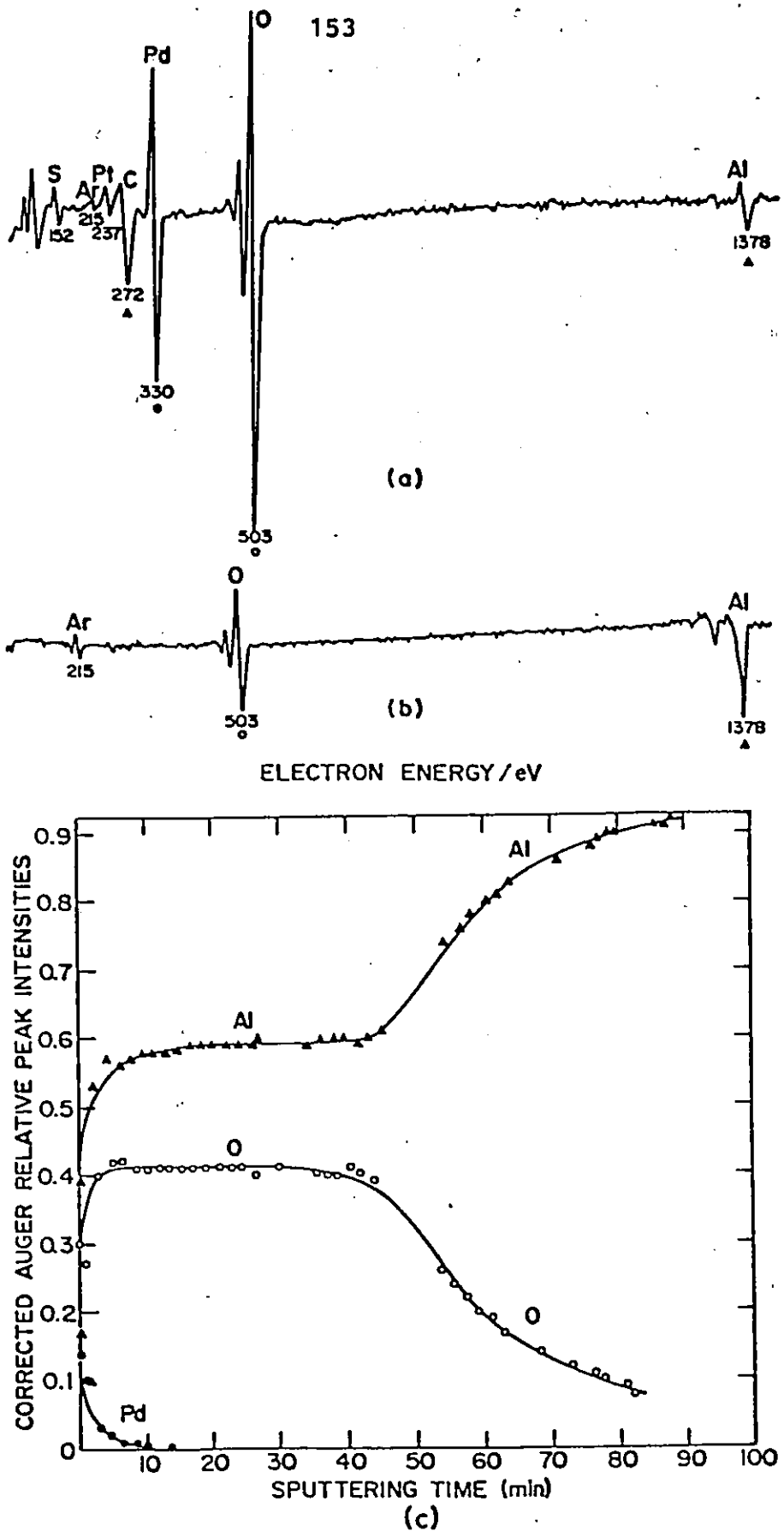

Fig.2. AES results for oxidized Al : (a) and (b) spectrums before and after sputtering the oxide film, (c) concentration profile across the film.

amorphous Al_2O_3 film.

NiO film on (111) Ni

The electron transmission image and the selected area diffraction pattern of the 150 nm thick NiO film formed on (111) Ni in 20 min at 923 K are shown in Fig.3. This relatively uniform film is composed of small crystallites which are sufficiently oriented with respect to the metal to give rise to a spot diffraction pattern. The Auger electron spectra prior to, at intermediate stage and after complete sputtering the oxide film are shown in Fig.4 together with the concentration profiles.

The palladium marker in this case is only detected after sputtering in the vicinity of the metal/oxide interface wnere the oxygen and nickel contents deviate from the steady state values for the NiO film; it was found to lay within a 26 nm region of the metal interface. Unfortunately, the transition in the concentration profile between the oxide film and metal is continuous rather than a step function to be expected at a sharp NiO/Ni interface. This smearing effect was also found at the oxide/metal interface in the previously investigated case of Al_2O_3 growth on Al, Fig.2. Possible causes for this phenomenon can be ascribed to the development of uneven metal/oxide interface during film growth, non-uniform sputtering of the oxide film and different sputtering coefficients of the film constituents and the palladium marker. SEM micrographs shown in Fig.5 of the NiO film before and after partial sputtering demonstrate that the original oxide surface

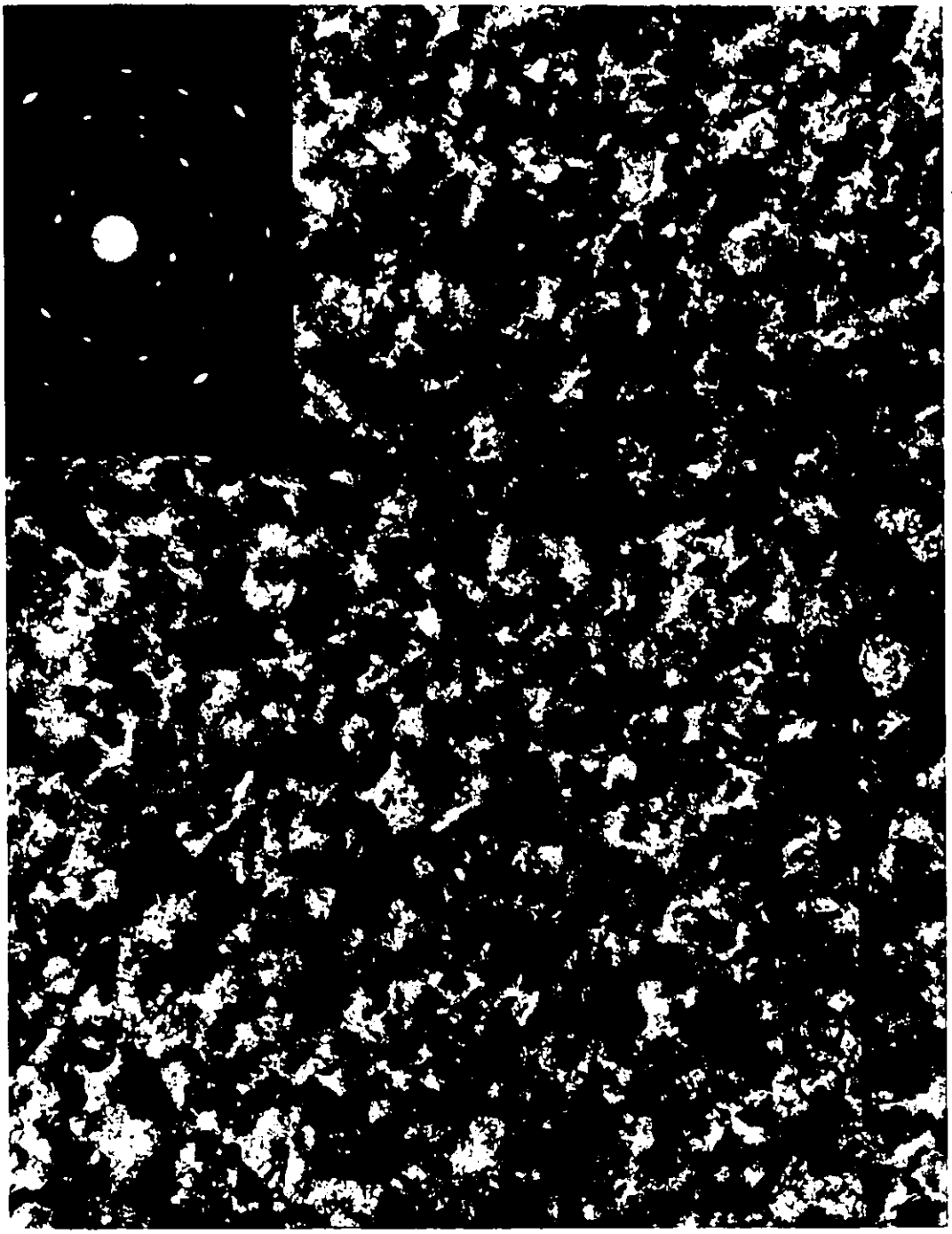

Fig. 3. Transmission electron image and selected area diffraction pattern of a NiO film formed in 20 min. on (111) Ni at 923 K.

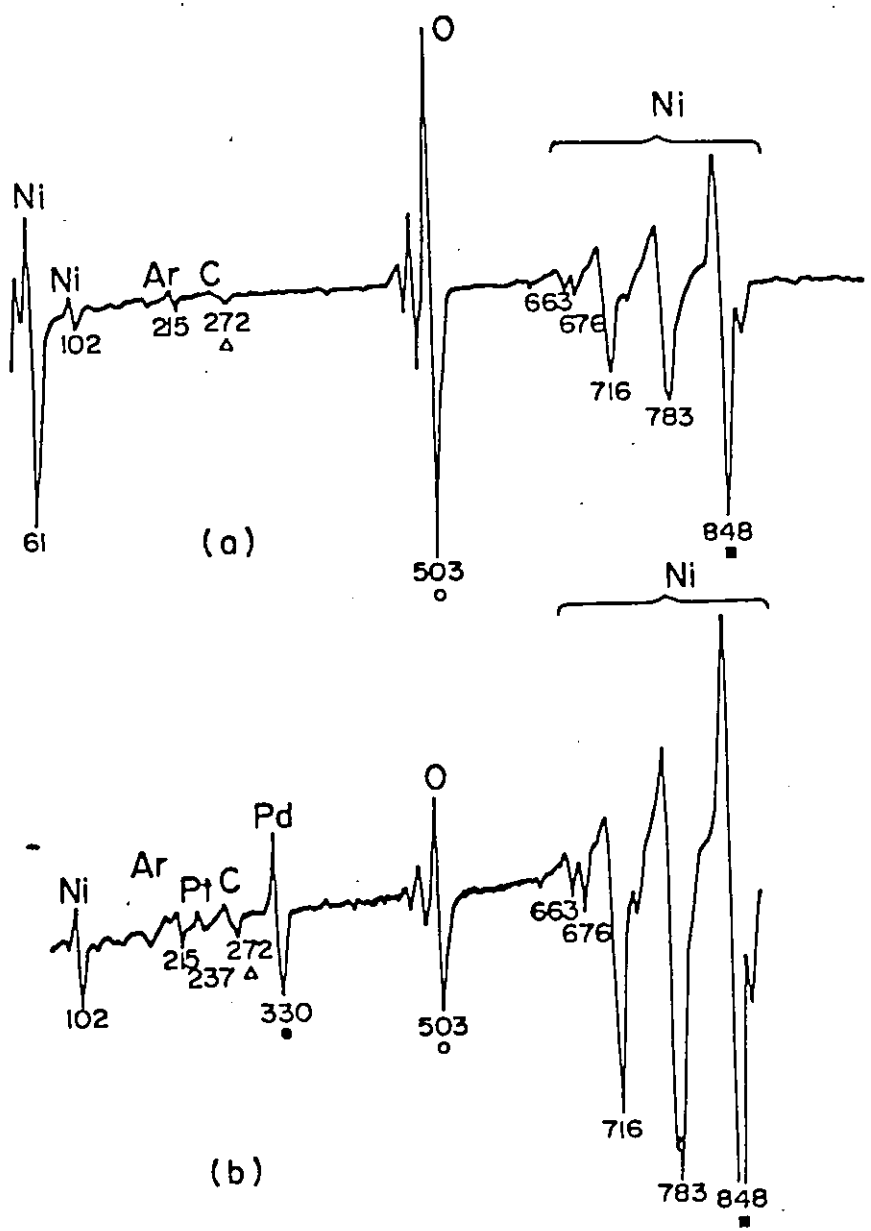

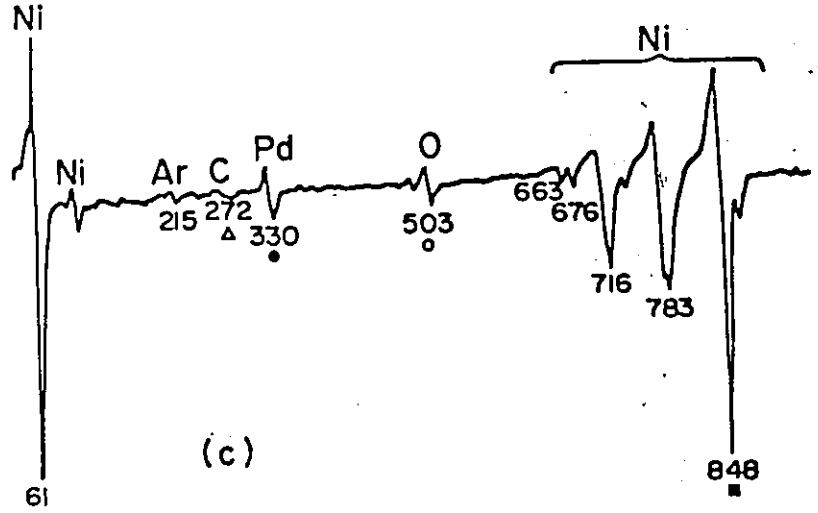

ELECTRON ENERGY /eV

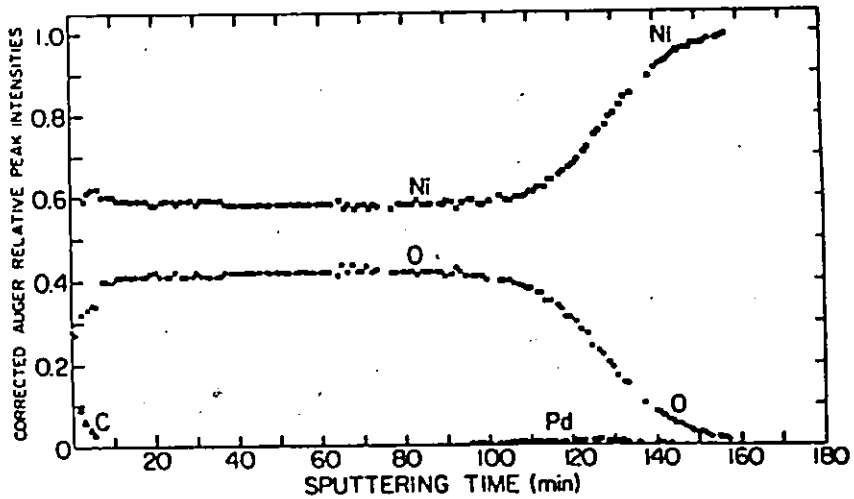

(d)

Fig.4. AES results for oxidized Ni : (a),(b) and (c) spectrums prior to, at intermediate stage and after sputtering the oxide film, (d) concentration profile across the film.

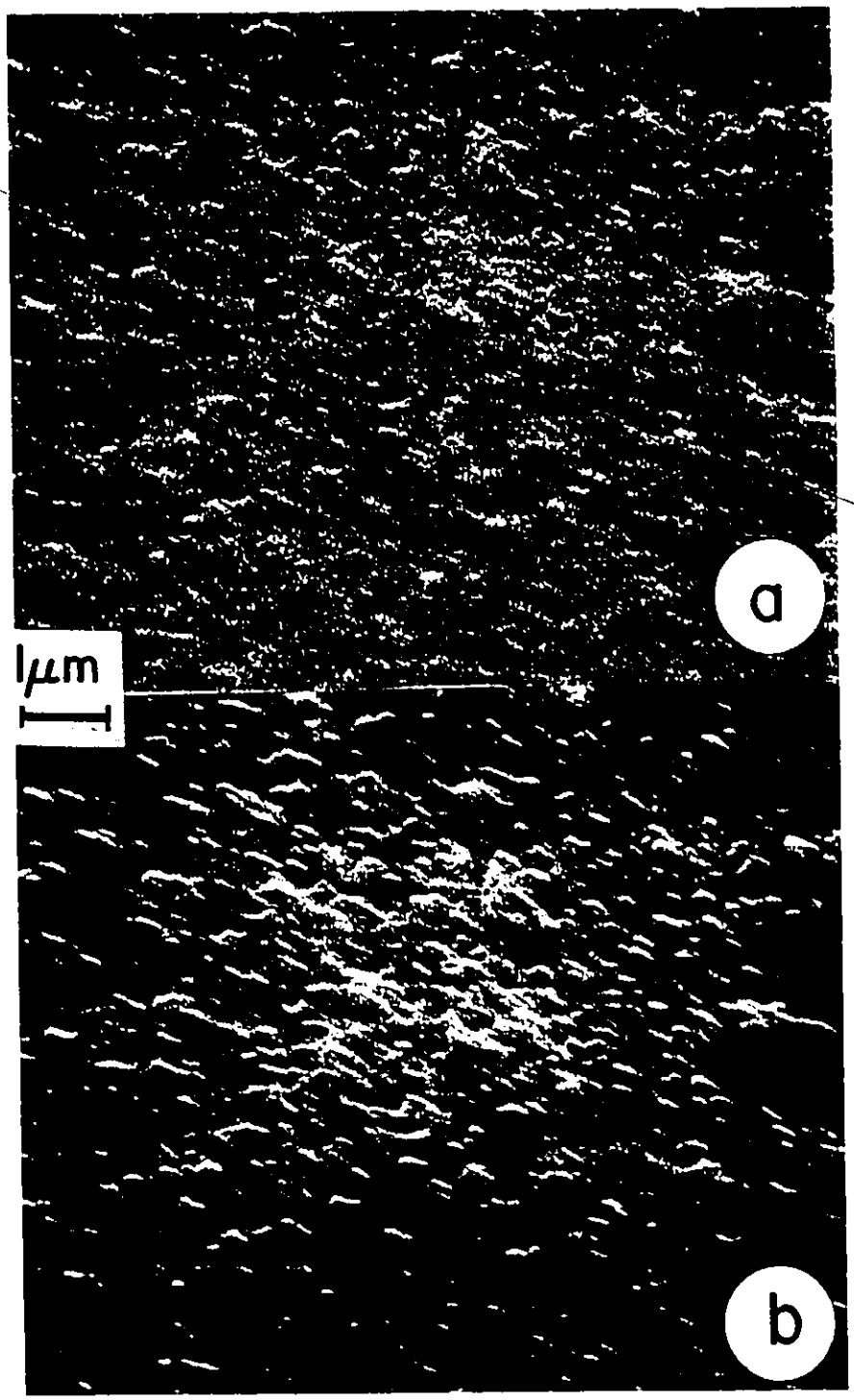

Fig.5. NiO film structure prior to (a) and after partial sputtering (b).

was relatively smooth and that surface roughness and faceting developed as a consequence of sputtering.

These results for predominant diffusion of nickel in the film, despite the limitation imposed by uneven sputtering, are consistent with the findings of Atkinson et al[177] who have demonstrated that oxygen is immobile in NiO films less than 300 nm thick by examining the distribution of an ^{18}O tracer upon its activation by the $^{18}O(p,\alpha)^{15}N$ reaction.

REFERENCES

1. C.T. Sims, J. Metals, 18, 1119 (1966).

2. A.U. Seybolt, Trans. ASM, 59, 861 (1966).

3. P. Grenier and M. Marchal, Mém. Sci. Rev. Mét., 65, 5 (1968); ibid, 66, 929 and 933 (1969).

4. C.A. Stearns, F.J. Kohl and G.C. Fryburg, J. Electochem. Soc., 121, 945 (1974) ;
Y.W. Kim and G.R. Belton, Met. Trans., 5, 1811 and 2151 (1974).

5. E.A. Gulbransen and K.F. Andrew, Metal-Slag-Gas Reactions and Processes, Z.A. Foroulis and W.W. Smeltzer, Editors, The Electrochem. Soc., N.J., 343-354 (1975).

6. J. Askill, Tracer Diffusion Data for Metals, Alloys and Simple Oxides, Plenum Press (1970).

7. P. Kofstad, Nonstoichiometry, Diffusion and Electrical Conductivity in Binary Metal Oxides, Wiley, N.Y. (1972).

8. G.W. Goward, D.H. Boone and G.S. Giggins, Trans. ASM, 60, 228 (1967).

9. T.K. Redden, Met. Trans. (AIME), 242, 1695 (1968).

10. N.R. Lindblad, Oxid. Met., 1, 143 (1969).

11. G.W. Goward, J. Metals, 22, 31 (1970).

12. G.W. Goward and D.H. Boone, Oxid. Met., 3, 475 (1971).

13. G. Lehnert and H. Meinhardt, Elec. Dep. Surf. Treat., 1, 71 and 189 (1972/73).

14. J.L. Smialek and C.E. Lowell, J. Electrochem. Soc., 121, 800 (1974).

15. A.J. Hickl and R.W. Heckel, Met. Trans., 6A, 431 (1975).

16. F.S. Pettit, Trans. Met. Soc. (AIME), 239, 1296 (1967).

17. J.S. Wolf and E.B. Evans, Corros.-NACE, 18, 129t (1962).

18. F.H. Stott and G.C. Wood, Corros. Sci., 17, 647 (1977).

19. G.C. Wood and F.H. Stott, Brit. Corros. J., 6, 247 (1971).

20. W.C. Hagel, Corros.-NACE, 21, 316 (1965).

21. J.D. Kuenzly and D.L. Douglass, Oxid. Met., 8, 139 (1974).

22. J.L. Smialek, Met. Trans., 9A, 309 (1978).

23. J.K. Tien and F.S. Pettit, Met. Trans., 3, 1587 (1972).

24. A. Kumar, M. Nasrallah and D.L. Douglass, Oxid. Met., 8, 227 (1974).

25. C.S. Giggins and F.S. Pettit, Rep. N° ARL 75-0234, Pratt and Whitney Aircraft, Connecticut (1975).

26. E.J. Felten and F.S. Pettit, Oxid. Met., 10, 189 (1976).

27. F.A. Golightly, F.H. Stott and G.C. Wood, Oxid. Met., 10, 163 (1976).

28. I.M. Allam, D.P. Whittle and J. Stringer, Oxid. Met., 12, 35 (1978).

29. J.S. Sheasby and D.B. Jory, Oxid. Met., 12, 527 (1978).

30. U.R. Evans, The Corrosion and Oxidation of Metals, Edwin Arnold, London (1960); Supplement (1968).

31. O. Kubaschewski and B.E. Hopkins, Oxidation of Metals and Alloys, Butterworths, London (1962).

32. J. Bénard, L'Oxydation des Métaux, 1 and 2, Gauthier-Villiards, Paris (1962-64).

33. K. Hauffe, Oxidation of Metals, Plenum Press, N.Y. (1965).

34. P. Kofstad, High Temperature Oxidation of Metals, Wiley, N.Y. (1966).

35. ASM Seminar, Oxidation of Metals and Alloys, American Society for Metals, Ohio (1971).

36. M.S. Seltzer and R. Jaffee, Editors, Defect and Transport in Oxides, Plenum Press, N.Y. (1974).

37. S. Mrowec and T. Werber, Gas Corrosion of Metals, Nat. Center for Scientific Information, Warsaw (1978).

38. R.C. Logani and W.W. Smeltzer, Can. Met. Quart., 10, 149 (1971).

39. W.W. Smeltzer and D.J. Young, Prog. Sol.-St. Chem., 10, Part (1), 17 (1975).

40. F.P. Fenlner and N.F. Mott, Oxid. Met., 2, 59 (1970); M.J. Dignam, D.J. Young and G.W. Goad, J. Phys. Chem. Solids, 34, 1227 and 1235 (1973).

41. C. Wagner, Corros. Sci., 13, 23 (1973).

42. C. Wagner, Z. Phys. Chem., B21, 25 (1933) ; ibid, Atom Movements, ASM, Ohio, 153 (1951).

43. J.M. Perrow, The Role of Structural Defects in the Growth of Thin Nickel Oxide Films, Ph.D. Thesis, McMaster University (1967).

44. J.M. Perrow, W.W. Smeltzer and R.K. Ham, Acta Met., 15, 577 (1967).

45. J.M. Perrow, W.W. Smeltzer and J.D. Embury, Acta Met., 16, 1209 (1968).

46. N.N. Khoi, The Growth and Structure of Nickel Oxide Formed on the (100), (110) and (111) Crystal Faces of Nickel, Ph.D. Thesis, McMaster University (1972).

47. T. Homma, N.N. Khoi, W.W. Smeltzer and J.D. Embury, Oxid. Met., 3, 463 (1971).

48. R. Herchl, N.N. Khoi, T. Homma and W.W. Smeltzer, Oxid. Met., 4, 35 (1972).

49. N.N. Khoi, W.W. Smeltzer and J.D. Embury, J. Electrochem. Soc., 122, 1495 (1975).

50. A. Madeyski, D.J. Poulton and W.W. Smeltzer, Acta Met., 17, 579 (1969).

51. W.W. Smeltzer, R.R. Haering and J.S. Kirkaldy, Acta Met., 9, 880 (1961).

52. D. McLean, Grain Boundaries in Metals, Claredon Press, 224 (1957).

53. J.V. Cathcart, G.F. Petersen and C.J. Sparks, J. Electrochem. Soc., 116, 664 (1969).

54. M.J. Graham, R.J. Hussey and M. Cohen, J. Electrochem. Soc., 120, 1523 (1973).

55. Y. Oishi and W.D. Kingery, J. Chem. Phys., 33, 480 (1960).

56. A.E. Paladino and W.D. Kingery, J. Chem. Phys., 37, 957 (1962).

57. H. Fischmeister, Mém. Sci. Rev. Métal., LXII, 211 (1965).

58. S. Talbot and J. Bigot, ibid, LXII, 261 (1965).

59. E.A. Gulbransen, ibid, LXII, 253 (1965).

60. D.J. Barber, Phil. Mag., 10, 75 (1964).

61. R.L. Tallman and E.A. Gulbransen, J. Electrochem. Soc., 114, 1227 (1967).

62. A. Manolescu, Growth and Structure of NiO scales on polycrystalline Nickel, Ph. D. Thesis, McMaster University, (1977).

63. E.W. Hart, Acta Met., 5, 597 (1957).

64. J.S. Kirkaldy and L.C. Brown, Can. Met. Quart., 2, 89 (1963).

65. J.S. Kirkaldy, Can. Met. Quart., 8, 35 (1969).

66. A.D. Dalvi and D.E. Coates, Oxid. Met., 5, 113 (1972).

67. C. Wagner, Corros. Sci., 8, 889 (1968).

68. W.W. Smeltzer and D.P. Whittle, J. Electrochem. Soc., 125, 1116 (1978).

69. R.A. Rapp, Corros., 21, 382 (1965).

70. R.A. Rapp and H.D. Colson, Met. Trans. (AIME), 236, 1616 (1966).

71. H.F. Merrick, Met. Trans., 4, 885 (1973).

72. L.R. Cornwell and G.R. Purdy, Met. Trans., 5, 780 (1974).

73. J.M. Oblak, J.E. Doherty, A.F. Giamei and B.H. Kear, Met. Trans., 5, 1252 (1974).

74. H. Davies and W.W. Smeltzer, J. Electrochem. Soc., 121, 543 (1974).

75. C.S. Giggins and F.S. Pettit, J. Electrochem. Soc., 118, 1783 (1971).

76. G.R. Wallwork and A.Z. Hed, Oxid. Met., 3, 171 (1971).

77. M. Hansen and K. Anderko, Constitution of Binary Alloys, McGraw-Hill, New York (1958).

78. L.H. Van Vlack, Materials Science for Engineers, Addison-Wesley, New York, 64 and 506 (1970).

79. L.R. Cornwell, The Mechanical Properties of Precipitation Hardened Nickel-Aluminum Alloys, Ph.D. Thesis, McMaster University (1969).

80. T. Hughes, E.P. Lautenschlager, J.B. Cohen and J.O. Brittain, J. Appl. Phys., 42, 3705 (1971).

81. A. Taylor and N.J. Doyle, J. Appl. Cryst., 5, 201 (1972).

82. A. Ball and R.E. Smallman, Acta Met., 16, 233 (1968).

83. W. Yang, R.A. Dodd and P.R. Strutt, Met. Trans., 3, 2049 (1972).

84. H.L. Fraser, M.H. Loretto, R.E. Smallman and R.J. Wasilewski, Philos. Mag., 28, 639 (1973).

85. J.E. Eibner, H.J. Engell, H. Schultz, H. Jacobi and G. Schlatte, Philos. Mag., 31, 739 (1975).

86. L.S. Darken and R.W. Gurry, Physical Chemistry of Metals, Metallurgical Series, McGraw-Hill, New York, 349 (1951).

87. S. Rosen and J.A. Goebel, TMS (AIME) 242, 722 (1968).

88. J.L. Smialek and R.F. Hehemann, Met. Trans., 4, 1571 (1973).

89. J.L. Smialek, Met. Trans., 2, 913 (1971).

90. A. Steiner and K.L. Komarek, TMS (AIME), 230, 786 (1964).

91. R.E. Haneman and A.U. Seybolt, TMS (AIME), 245, 437 (1969).

92. S.C. Schaefer, Rep. N° 7993, USA Bureau of Mines (1975).

93. O. Kubashewski, Trans. Far. Soc., 54, 814 (1958).

94. R. Hultgren, R.L. Orr, P.D. Anderson and K.K. Kelley, Editors, Selected Values of Thermodynamic Properties of Metals and Alloys, John Wiley, new York (1963).

95. J.F. Elliot and M. Gleiser, Editors, Thermochemistry for Steel Making, Addison-Wesley (1960).

96. M.M.P. Janssen and G.D. Reick, TMS (AIME), 239, 1372 (1967).

97. M.M.P. Janssen, Met. Trans., 4, 1623 (1973).

98. J.D. Whittenberger, Met. Trans., 3, 2010 (1972).

99. G.F. Hancock, Phys. Stat. Sol. (a), 7, 535 (1971).

100. P. Delavignette, H, Richel and S. Amelinkx,Phys. Stat. Sol. (a), 13, 545 (1973).

101. G.C. Wood, I.G. Wright and J.M. Ferguson, Corros. Sci., 5, 645 (1965).

102. M.L. Volpe and J. Reddy, J. Chem. Phys., 53, 1117 (1970).

103. W.C. Tripp and N.M. Tallan, J. Amer. Ceram. Soc., 53, 531 (1970).

104. Y.D. Tretyakov and R.A. Rapp, TMS (AIME) , 245, 1235 (1969).

105. M.T. Shim and W.J. Moore, J. Chem. Phys., 26,802 (1957).

106. M. O'Keeffe and W.J. Moore, J. Phys. Chem., 65,1438 (1961).

107. J.S. Choi and W.J. Moore, J. Phys. Chem., 66, 1308 (1962).

108. A. Atkinson and R.I. Taylor, J. Mat. Sci., 13, 427 (1978).

109. J.M. Jarzebski and S. Mrowec, Oxid. Met., 1, 267 (1969).

110. J.D. Christian and W.P. Gilbreath, Oxid. Met., 9, 1 (1975).

111. D.F. Mitchell, P.B. Sewell and M. Cohen, Surf. Sci., 61, 355 (1976).

112. L. Berry and J. Paidassi, C.R. Acad. Sci. Paris, 258, 2810 (1964);
ibid, Mém. Sci. Rev. Métal., LXV, 651 (1968).

113. K. Fueki and J.B. Wagner, J. Electrochem. Soc.,112, 384 (1965).

114. H. Uhlig, J. Pickett and J. McNairn, Acta Met., 7, 111 (1959).

115. K. Hauffe, L. Pethe and R. Schmidt, J. Electrochem. Soc., 115, 456 (1968).

116. C. Wagner, Corros. Sci., 10, 641 (1970).

117. M.J. Graham and M. Cohen, J. Electrochem. Soc., 119, 879 (1972).

118. M.J. Graham, D. Caplan and M. Cohen, J. Electrochem. Soc., 119, 1265 (1972).

119. S. Matsunaga and T. Homma, Oxid. Met., 10, 361 (1976).

120. M.J. Graham, G.I. Sproule, D. Caplan and M. Cohen, J. Electrochem. Soc., 119, 883 (1972).

121. D. Caplan, M.J. Graham and M. Cohen, J. Electrochem. Soc., 119, 1205 (1972).

122. J.A. Startell and C.H. Li, J. Inst. Metals, 90, 92 (1961).

123. N. Birks and H. Richert, J. Inst. Metals, 91, 308 (1962).

124. A.G. Evans, D. Rajdev and D.L. Douglass, Oxid. Met., 4, 151 (1972).

125. F.N. Rhines and J.S. Wolf, Met. Trans., 1, 1701 (1970).

126. H. Yanagida and F.A. Kröger, J. Amer. Ceram. Soc.,51, 700 (1968).

127. J. Beretka and M.J. Ridge, J. Chem. Soc. (A), London, 2106 (1967).

128. B.A. Scott and W.H. Horsman, Trans. Brit. Ceram. Soc., 69, 37 (1970).

129. J. Drowart, G. DeMaria, R.P. Burns and M.G. Inghram, J. Chem Phys., 32,1336 (1960).

130. P. E. Doherty and R.S. Davis, J. Appl. Phys., 34, 619 (1963).

131. M.J. Pryor, Oxid. Met., 3, 523 (1971).

132. H.C. Stumpf, A,S. Russel, J.W. Newsome and C.M. Tucker, Ind. Eng. Chem., 42, 1398 (1950).

133. P.P. Budnikov and A.M. Ginstling, Principles Of Solid State Chemistry, translated from Russian and edited by K. Shaw, Gordon and Breach Sci. Pub., New York, 299 (1968).

134. D. Ghosh and D.A.R. Kay, Ref.(5), p. 267.

135. O. Kubaschewski and E. Evans, Metallurgical Thermochemistry, Pergamon Press, Oxford (1967).

136. W.W. Smeltzer, Corros.-NACE, 11, 18 (1955); ibid, J. Electrochem. Soc., 103, 209 (1956).

137. M.J. Dignam, W.R. Fawcett and H. Böhni, J. Electrochem. Soc., 113, 656 and 663 (1966).

138. A.F. Beck, M.A. Heine, E.J. Caule and M.J. Pryor, Corros. Sci., 7, 1 (1966); A.J. Brock and M.J. Pryor, Corros. Sci., 13, 199 (1973).

139. M.J. Dignam, J. Electrochem. Soc., 109, 184 and 192 (1962).

140. J. Pappis and W.D. Kingery, J. Amer. Ceram. Soc., 44, 459 (1961).

141. P.J. Harrop and R.H. Creamer, Brit. J. Appl. Phys., 14, 335 (1963).

142. R.J. Brook, J. Yee and F.A. Kröger, J. Amer. Ceram. Soc., 54, 444 (1971); J. Yee and F.A. Kröger, J. Amer. Ceram. Soc., 56, 189 (1973).

143. H. Schmalzried, Z. Physik. Chem., 38, 87 (1963).

144. W.H. Gitzen, Editor, Alumina as a Ceramic Material, Amer. Ceram. Soc. Special Pub. N° 4.

145. J.D. Tretjakow and H. Schmalzried, Ber Busenges, 69, 396 (1965).

146. F.S. Pettit, E.H. Randklev and E.J. Felten, J. Amer. Ceram. Soc., 49, 199 (1966).

147. R.C. Weast, Editor, Handbook of Chemistry and Physics, 52nd ed., Chem. Rub. Co (1971/72).

148. W.J. Minford and V.S. Stubican, J. Amer. Ceram. Soc., 57, 363 (1974).

149. B. Phillips, J.J. Hutta and I. Warshaw, J. Amer. Ceram. Soc., 49, 579 (1963).

150. J.S. Armijo, Oxid. Met., 1, 171 (1969).

151. P. Sullivan, J. Jensen, D.S. Duvall and T.T. Field, Trans. ASM, 61, 582 (1968).

152. R.S. Crouse, Metallography Appendix, ASM Spec. Pub.

153. W.J. Alford and D.L. Stephens, J. Amer. Ceram. Soc., 46, 193 (1963).

154. C.S. Barrett and T.B. Massalski, Structure of Metals, McGraw-Hill, New York (1966).

155. T. Homma, Inst. Ind. Sci., Un. of Tokyo, Private Communication (1976-78).

156. A.S. Darling, Int. Met. Rev., 18, 91 (1973); J.C. Chaston, Plat. Met. Rev., 19, 135 (1975).

157. L.E. Davis, N.C. McDonald, P.W. Palmberg, G.E. Riach and R.E. Weber, Editors, Handbook of Auger Electron Spectroscopy, Editors, Phys. Elect. Ind., Minnesota, 2nd ed. (1976).

158. F.S. Pettit, Pratt and Whitney Aircraft Group, United Technologies, East Hartford, Connecticut, Private Communication.

159. F. Elrefaie, McMaster University, Private Communication.

160. A. Dalvi, Senior Editor, The Electron Probe Micro-Analyzer, a McMaster Publication (1969).

161. C.B. Alcock and P.B. Brown, Met. Sci. J., 3, 116 (1969).

162. J. Stringer, B.A. Wilcox and R.I. Jaffee, Oxid. Met., 5, 11 (1972).

163. D.R. Tenney, C.T. Young and H.W. Herring, Met. Trans., 5, 1001 (1974).

164. G.R. Wallwork and Z. Hed, Oxid. Met., 3, 213 (1971).

165. J.M. Perrow and W.W. Smeltzer, J. Electrochem. Soc., 109, 1023 (1962).

166. G.C. Wood and D.P. Whittle, Corros. Sci., 7, 763 (1967).

167. R.C. Logani and W.W. Smeltzer, Oxid. Met., 3, 15 (1971).

168. C.S. Giggins and F.S. Pettit, TMS (AIME), 245, 2495 and 2509 (1969).

169. R. Hales and A.C. Hill, Corros. Sci., 12, 843 (1972).

170. V.R. Howes, Corros. Sci., 8, 221 (1968).

171. V.R. Howes, Corros. Sci., 10, 99 (1970).

172. G.B. Gibbs and R. Hales, Corros. Sci., 17, 487 (1977).

173. L. Brewer and A.W. Searcy, J. Amer. Chem. Soc., 73, 5308 (1951).

174. G. Romeo, W.W. Smeltzer and J.S. Kirkaldy, J. Electrochem. Soc., 118, 1336 (1971).

175. J. Markali, Mechanical Properties of Engineering Ceramics, W.W. Kriegel and H.Palmour, Editors, Interscience, N.Y. (1961).

176. R.A. Rapp, A. Ezis and J. Yurek, Met. Trans. 4, 1283 (1973).

177. A. Atkinson, R.I. Taylor and P.D. Goode, Report AERE-R8985, UK Atomic Energy Authority, Harwell, Oxfordshire, England, January (1978).